Control and measurement of a single-ion quantum harmonic oscillator

by

Katherine Casey McCormick

B.S., Astrophysics, University of California, Santa Cruz, 2012

B.A., Mathematics, University of California, Santa Cruz, 2012

A thesis submitted to the

Faculty of the Graduate School of the

University of Colorado in partial fulfillment

of the requirements for the degree of

Doctor of Philosophy

Department of Physics

2019

This thesis entitled:
Control and measurement of a single-ion quantum harmonic oscillator
written by Katherine Casey McCormick
has been approved for the Department of Physics

Dietrich Leibfried

David J. Wineland

Date

The final copy of this thesis has been examined by the signatories, and we find that both the content and the form meet acceptable presentation standards of scholarly work in the above mentioned discipline.

McCormick, Katherine Casey (Ph.D., Physics)

Control and measurement of a single-ion quantum harmonic oscillator

Thesis directed by Dr. Dietrich Leibfried and Prof. David J. Wineland

A trapped-ion harmonic oscillator represents a rich and well-controlled platform for tests of quantum physics, with applications to quantum simulations, quantum sensing, and quantum information processing. Owing to its net charge, the ion's motion is affected by changes in the electric potential. Consequently, electric field and potential curvature noise will limit the coherence of the ion's harmonic oscillation. While in some respects, this serves as a limitation in the performance of the trapped ion system (for example, in the fidelity of two-qubit gates or quantum simulations with motional quanta), it also opens an opportunity to use the ion as a precise field sensor and to use engineered quantum states of motion to enhance the sensitivity to these fields beyond the standard quantum limit (SQL). This thesis describes the implementation of such applications on a single beryllium ion confined in a Paul trap.

In the thesis, I present the theory of an ideal harmonic oscillator and the implementation of this system using the motion of a single trapped ion, including producing special quantum states of motion; these states include the energy eigenstates of the harmonic oscillator, called number states, up to $n = 100$, superpositions of number states of the form $\frac{1}{\sqrt{2}}(|0\rangle + |n\rangle)$, with n up to 18, and coherently displaced number states with an average occupation $\bar{n}$ up to approximately 300. I describe how we use these quantum states of motion for precise sensing of fluctuations of the harmonic oscillator frequency. The sensitivity of the $\frac{1}{\sqrt{2}}(|0\rangle + |n\rangle)$ state ideally follows the $1/n$ Heisenberg scaling for frequency sensitivity. Additionally, I describe investigations of the spectrum of motional frequency noise using a series of coherent displacements of the motion of the ion, with features similar to Ramsey and dynamical decoupling sequences for two-level systems. While these displaced states don't

improve sensitivity over the SQL, they can be simply and rapidly implemented with trapped ions. I discuss extensions to all of these experiments, including to multiple ions in a new trap designed to confine 3 or 4 ions in individually tunable potential wells.

Dedication

For Mom and Dad.

Acknowledgements

These 7 years have been a time of great personal growth. I owe a lot of this to my experiment, where my tenacity and gumption was tested many times. Whenever the cryostat broke in a new and interesting way, I was grateful to have fellow graduate students Susanna, Raghu, and Shaun in the lab to offer suggestions and sympathy, postdocs David A. (now a professor at University of Oregon) and Daniel (now a staff scientist) as well as my co-advisor, Dave W. to give sage advice and encouragement, and Andrew, who, despite being my de facto advisor, got his hands dirty and helped with a lot of the tedious tasks and never gave up on me. Later additions to the lab whom I am grateful to are Hannah, who has taken on an ambitious project, but always greets her problems with humor, and Jonas, who saved me from the lab, taking over many of my half-finished projects, so that I could turn to my computer to write 2 papers, a proposal, and this thesis, all in succession. I know that I leave this experiment in very thoughtful and capable hands and I'm excited to see what comes out of it with Jonas at the helm. Finally, I would like to express endless gratitude to my advisor, Didi. He gave me support, encouragement, and pressure when I needed it to persevere and never settle for less than excellence. An additional thanks goes especially to Dave and Didi, who have had to read a *lot* of my writing in the past year or so. Their comments on my work have greatly improved my writing, and I am grateful to them for the many hours spent on this.

Outside of the lab, I found camaraderie in a few different circles. The dinner club nights and "chool" bus bouldering trips with Mike, Matt, Molly, Steve, Tom, Dan, and company

provided well deserved diversion through the early years of grad school. Later, being a member of the CU women's ultimate team, Colorado Kali, was one of the most rewarding things I have participated in. I am inspired by the dedication, grit, and weirdness of that group of women. Finally, I thoroughly enjoyed living in our little bus commune-turned conventional house with Dani, Britt, Erica, Nicole, and Buck over the last few years.

Thank you, Mom and Dad, for the lifetime of unwavering love and support, and Ryan and Matthew for the jokes, games, and conversations about science, politics, climbing, and everything in between. Dad and Matthew, I will cherish the memories made during our annual 14er hikes and hope that this tradition continues in the PNW and wherever else life takes us.

And finally, Dan. These last 2 years with you have been wonderful. Thank you for the snacks, back-rubs, encouragement, and tolerance of the stressball I've been during the final stretch of graduate school.

Contents

Chapter

Tables

Table

Figures

Figure

Chapter 1

Introduction

In this thesis, I will describe a series of experiments that use quantum states of a single trapped ion to characterize its center-of-mass motion and fields that affect it. From my perspective, there are several motivations for this work: 1) it allows us to test quantum mechanics (QM) in new regimes and develop techniques that can be applied to other systems, for example, macroscopic systems, which will provide additional tests of QM. 2) It enables us to utilize QM to our benefit, using quantum coherence to obtain better measurement precision than we would otherwise be able to achieve. 3) It provides a way forward for higher-fidelity quantum computations with trapped ions that rely on the motional coherence of the ions.

1.1 The harmonic oscillator as a test bed for quantum physics

Because of its strange and counterintuitive predictions, quantum mechanics has a long history of inspiring spirited arguments among prominent physicists. Albert Einstein famously proclaimed, "God does not play dice," as he had deep discomfort with the probabilistic nature of quantum mechanics, introducing the EPR paradox to argue that quantum mechanics is not a complete description [Einstein et al., 1935; Einstein, 1936]. Erwin Schrödinger, too, did not like the implications of quantum mechanics, and through correspondence with Ein-

stein, he developed the "cat paradox" which has since come to be known as "Schrödinger's cat" [Schrödinger, 1935]. The premise of the paradox is this: a cat is in an isolated box with a radioactive particle. When the particle decays, it triggers a mechanism that kills the cat. At a time equal to the half-life of the particle, an observer opens the box to find the cat either dead if the particle decayed or alive if the particle did not. Quantum mechanics says that before the observer opens the box, the cat is in a superposition of both dead and alive, entangled with the particle's state.

Schrödinger's cat paradox represents a description of events which is at odds with human intuition; this has unsettled many scientists, opening opportunity to resolve this apparent paradox by refining our intuition of quantum mechanics and exploring the boundary between the quantum and classical descriptions of nature. This has inspired interest in observing quantum mechanics on mesoscopic and macroscopic scales, and continues to be an intriguing area of study from a philosophical and foundational perspective. Researchers continue to design experiments to push the boundaries of quantum mechanics by producing larger and larger quantum states. For example, researchers have prepared macroscopic superpositions of states in a superconducting circuit [Wilhelm et al., 2001], entangled the vibrational modes of two particles consisting of 10^{16} atoms, separated by 15 cm [Lee et al., 2011], and observed wave-particle duality in compounds with masses of approximately 10^4 times the mass of a proton [Eibenberger et al., 2013].

The harmonic oscillator, a thoroughly studied, well understood, and ubiquitous physical system, could provide the ideal platform for such tests of quantum mechanics. The textbook example of a harmonic oscillator is a mass on a spring which oscillates due to the restoring force provided by the spring. Other examples include: a pendulum swinging back and forth under gravity, an LC electrical circuit, light in an optical cavity, microfabricated cantilevers and membranes, and a single ion in a harmonic trap. In principle, every harmonic oscillator

is a quantum harmonic oscillator, but the quantum mechanics that governs the dynamics of the system is not typically apparent until we go to the very small and very cold. Recent experiments have studied quantum mechanical behavior of higher energy states [McCormick et al., 2019a; Joshi et al., 2019] or of larger, more massive oscillators [Lee et al., 2011; Chu et al., 2018], at scales where the behavior is usually well described by classical mechanics. Such experiments serve to explore this boundary between quantum and classical physics and demonstrate a growing level of quantum control over relatively large harmonic oscillators.

1.2 Quantum-enhanced measurements

With improved control over harmonic oscillator systems, researcher have been able to push the limits of systems exhibiting hallmarks of quantum mechanics farther than ever before. But as the states become more non-classical, they also become more susceptible to perturbations from the environment. This increased coupling to the environment is often stated as one of the reasons that macroscopic quantum superpositions are typically not observed [Zurek, 1991]. While this poses limitations on the level of quantum control that we can achieve, it also opens an opportunity to use non-classical states as more sensitive probes of certain external perturbations. Therefore, efforts toward improved quantum control are not only of philosophical interest—more non-classical states could be used towards precision measurements, potentially contributing to technological advances and to answering fundamental questions about the nature of the universe. While the idea of using non-classical states to improve the performance of sensors is not new [Helstrom, 1976; Caves et al., 1980; Wineland et al., 1992; Bollinger et al., 1996], we have now achieved the level of measurement sensitivity where we benefit from using quantum techniques to enhance the sensitivity. LIGO, for example, has recently added the use of squeezed light in one arm of the interferometer for a factor of ~ 3 dB enhancement in their sensitivity to gravitational waves, which

promises about an 8-fold increase in detected events [Aasi, 2013]. The use of entangled many-atom states for enhanced performance in atomic clocks and atom interferometers is also on the horizon [Wineland et al., 1998; Polzik and Ye, 2016; Engelsen et al., 2016].

Likewise, the non-classical states of motion of a single trapped ion can be used for enhanced measurement sensitivity. Since ions have a net charge, they are particularly susceptible to electric fields. While this susceptibility affects the coherence of the quantum motion of the ion and limits the quantum states that we can produce, it also means that the more susceptible states are better probes of this electric field noise. Developing quantum-enhanced techniques for precise electric field and curvature measurement with a trapped-ion mechanical oscillator could contribute to discoveries in fundamental physics, surface science, and, as I will detail next, improved fidelity in quantum computations.

1.3 Application to trapped-ion quantum computing

In most trapped-ion quantum computing proposals, gates are achieved by coupling the ions' motion to their internal electronic and hyperfine states via lasers or microwave interactions. To generate a two-qubit gate, most proposals also rely on the fact that ions interact with one another via the Coulomb force, so oscillation of one ion is felt by the other [Cirac and Zoller, 1995]. Two-qubit gate fidelities achieved are among the highest for current implementations of qubit gates, but one of the main limitations is dephasing and heating of the harmonic oscillator motion providing the coupling between the qubits [Gaebler et al., 2016; Ballance et al., 2016].

Some of these errors can be attributed to electric field noise. The dominating mechanism that produces electric field noise on trap electrodes is not known and an active area of investi-

gation. Of particular interest is the electric field noise near the harmonic oscillator frequency which heats the harmonic oscillator—this is known as anomolous heating because the source is unclear and cannot be attributed to Johnson or technical noise [Brownnutt et al., 2015].

The experiments I will discuss in this thesis contribute to further study of the motional coherence of ions, helping to answer questions about anomolous heating and electric field noise. Unlike other studies on anomalous heating, these methods also provide a way to measure noise components at frequencies away from the harmonic oscillator frequency. This allows us to follow the oscillator frequency as it changes over time, minimizing errors associated with undetected deviations between the oscillation frequency and, for example, frequencies of a laser driving a two-qubit gate operation. This could help identify and alleviate the added susceptibility to fluctuating stray fields when using traps with very small ion-to-electrode distances, which offer significant advantages in terms of scalability and speed of operation in high-fidelity quantum computing.

1.4 Thesis structure

This thesis is structured as follows. I will first briefly cover quantum harmonic oscillators, including introducing different representations of quantum harmonic oscillator states of particular interest. Then I will discuss the implementation of a trapped-ion harmonic oscillator, including parts of the system that go beyond the simple one-dimensional harmonic oscillator model and how we are able to isolate a single mode of oscillation in the system to perform experiments which can be described by a simple 1-d model. Following a chapter describing the experimental apparatus, I will discuss experiments involving three different classes of states of a quantum harmonic oscillator: number (or Fock) states, superpositions of number states of the form $|0\rangle + |n\rangle$ (for simplicity, normalization is dropped), and coher-

ently displaced number states. Finally, I will discuss how these experiments performed with one ion can be extended to multiple ions, and in particular our plans with three ions in a triangular configuration.

Chapter 2

Quantum harmonic oscillators

"Everything is a **harmonic oscillator** or a two-level system."

- Professor Thomas Degrand, University of Colorado, 2012.

Harmonic oscillators are among the most ubiquitous physical systems. Harmonic motion is one of the first topics a first-year physics student encounters, and it is revisited time and time again in different contexts. An ion trapped in a confining potential is one of the simplest examples of a harmonic oscillator system. An object follows harmonic motion in a restoring potential, governed by spring constant k, of the form $V(x) = \frac{1}{2}kx^2$ so that the Hamiltonian that describes the system is

$$H = \frac{1}{2m}\hat{p}^2 + \frac{1}{2}m\omega^2\hat{x}^2, \tag{2.1}$$

where m is the mass of the object, $\omega = \sqrt{\frac{k}{m}}$ is the frequency of oscillation, and $\hat{x}$ and $\hat{p}$ are the position and momentum operators. Replacing $\hat{x}$ and $\hat{p}$ with the raising and lowering operators, $\hat{a}$ and $\hat{a}^\dagger$, where $\hat{x} = \sqrt{\frac{\hbar}{2m\omega}}(\hat{a}^\dagger + \hat{a})$ and $\hat{p} = i\sqrt{\frac{\hbar m\omega}{2}}(\hat{a}^\dagger - \hat{a})$, we have

$$H = \hbar\omega(\frac{1}{2} + \hat{n}) \tag{2.2}$$

where $\hat{n} = \hat{a}^\dagger\hat{a}$. Eigenenergies $E_n = \hbar\omega(1/2+n)$, with $n \geq 0$ an integer, are equidistant from one another, like rungs in a ladder (hence why $\hat{a}$ and $\hat{a}^\dagger$ are sometimes referred to as "ladder operators"). The eigenstates are called number states because of this linear dependence of the energy on the number n.

2.1 Wave mechanics representation

The eigenstates projected into position space, $\psi(x) = \langle x|\psi\rangle$ can be determined by finding the solutions to the Schrödinger equation in position space, $\hat{H}|\psi(x)\rangle = E|\psi(x)\rangle$, which becomes a second-order differential equation. The solutions are [Sakurai, 1993]:

$$\psi_n(x) = \frac{1}{\sqrt{2^n n!}}\left(\frac{m\omega}{\pi\hbar}\right)^{\frac{1}{4}} e^{-\frac{m\omega x^2}{2\hbar}} H_n\left(\sqrt{\frac{m\omega}{\hbar}}x\right) \tag{2.3}$$

where $H_n(z)$ is a Hermite polynomial:

$$H_n(z) = (-1)^n e^{z^2}\frac{d^n}{dz^n}\left(e^{-z^2}\right). \tag{2.4}$$

The wavefunctions for the first few eigenstates are shown in Fig. 2.1. As we can see from this figure, as n increases, the wavefunction becomes more dispersed and has n nodes in the amplitude, behaving more and more nonclassically. These are eigenstates, so the observables are stationary. There is no time evolution of the state, other than an overall phase factor $e^{in\omega t}$, which cannot be observed directly. However, the frequency difference between such phase factors can be observed in interferometric experiments, as described in detail in Sec. 2.4 below and later in Ch. 6.

2.2 Phase-space representation and Wigner functions

It is sometimes convenient to express the behavior of a mechanical system in phase space—where the position is plotted on the x-axis and the momentum is plotted on the y-axis. This representation is particularly convenient for harmonic potentials, where, in

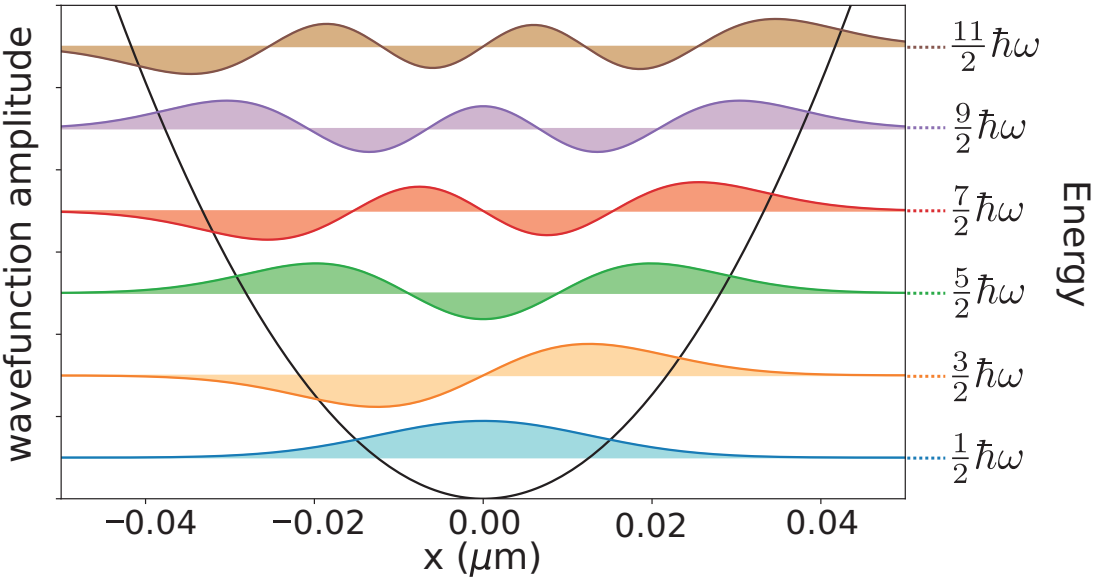

Figure 2.1: Wavefunctions and energies of the first few harmonic oscillator eigenstates of a $^9Be^+$ ion, where $\omega = 2\pi \times 7$ MHz. The wavefunction amplitudes (not normalized) versus position for $n = 0 - 5$ are plotted, with offsets equal to the energy of the state. The black parabola represents the harmonic confining potential.

classical mechanics, the evolution of a particle undergoes simple harmonic motion:

$$x(t) = A\sin(\omega t + \phi) \tag{2.5}$$

$$p(t) = m\frac{dx(t)}{dt} = mA\omega\cos(\omega t + \phi). \tag{2.6}$$

If we define dimensionless variables $\tilde{x}$ and $\tilde{p}$ to be

$$\tilde{x} = \frac{1}{2}\sqrt{\frac{2m\omega}{\hbar}}x \tag{2.7}$$

$$\tilde{p} = \frac{1}{2}\sqrt{\frac{2}{m\hbar\omega}}p, \tag{2.8}$$

then when plotted in phase space, the harmonic motion traces circles, with the radius $\alpha = \sqrt{m\omega/(2\hbar)}A$ proportional to the amplitude of the motion.[1]

In quantum mechanics, we can visualize a representation of the quantum state in phase space by defining a quasiprobability distribution, or Wigner function [Wigner, 1932]:

$$W(x,p) = \frac{1}{\pi\hbar}\int_{-\infty}^{+\infty}\psi^*(x+y)\psi(x-y)e^{2ipy/\hbar}dy. \tag{2.9}$$

If ψ is a pure state, then integrating the Wigner function over momentum p gives $\int_{-\infty}^{+\infty} dpW(x,p) = |\psi(x)|^2$, which is the probability distribution of the state in position space and is positive for all x. Likewise, $\int_{-\infty}^{+\infty} dxW(x,p) = |\Phi(p)|^2$. Note that the Wigner function can be negative in parts, hence why it is called a *quasi*probability distribution.

We can visualize certain features and dynamics of quantum states of a harmonic oscillator in phase space using this Wigner function representation, replacing x and p with their respective unitless counterparts, $\tilde{x}$ and $\tilde{p}$, defined above. There exist other phase-space representations of quantum states (e.g. Glauber-Sudarshan P, Husimi Q, etc.), but the Wigner

[1] Although we are discussing a classical harmonic oscillator and of course, $\hbar$ is a quantum unit, we use this scaling factor in anticipation of the transition to our discussion of quantum harmonic oscillators. In classical mechanics, the unitless phase-space representation can be accomplished using *any* constant with units of action in place of $\hbar$.

function is most prevalent and is sufficient in establishing the desired physical intuition for the quantum states of the harmonic oscillator systems.

2.2.1 Time evolution of Wigner functions and the rotating frame

The interaction picture [Sakurai, 1993] is commonly used in atomic physics when the Schrödinger picture Hamiltonian can be written as

$$\hat{H}(t) = \hat{H}_0 + \hat{V}_I(t) \tag{2.10}$$

where $\hat{H}_0$ is a time-independent, unperturbed Hamiltonian, and $\hat{V}_I(t)$ is a time-dependent interaction term. In the interaction picture, we define an interaction Hamiltonian:

$$\hat{H}_{int} = e^{i\hat{H}_0 t/\hbar}\hat{V}_I(t)e^{-i\hat{H}_0 t/\hbar} \tag{2.11}$$

and transform the original, Schrödinger-picture wavefunction $|\Psi_S(t)\rangle$ to $|\tilde{\Psi}(t)\rangle = e^{iH_0 t/\hbar}|\Psi_S(t)\rangle$ so that the transformed states evolve according to

$$\frac{d\,|\tilde{\Psi}(t)\rangle}{dt} = \hat{H}_{int}\,|\tilde{\Psi}(t)\rangle\,. \tag{2.12}$$

So, the state $|\tilde{\Psi}(t)\rangle$ evolves *only* according to the interaction term. (We can drop the tilde notation when it is clear which frame is used.) If there is no interaction, then the state in the interaction picture coincides with the state in the Heisenberg picture and is constant. An observable $\hat{O}_S$ that is time-independent in the Schödinger picture becomes time-dependent, and evolves according to $\hat{O}_I = e^{iH_0 t/\hbar}\hat{O}_S e^{-iH_0 t/\hbar}$.

In our case, where we have a harmonic oscillator and we visualize the time evolution via the rotation of Wigner functions in phase space, moving to the interaction picture amounts to moving to a frame that is rotating with frequency $\omega_0 = H_0/\hbar$ in phase space, so the ladder

operators in the interaction picture become:

$$\hat{a}^\dagger \rightarrow \hat{a}^\dagger e^{i\omega_0 t} \tag{2.13}$$

$$\hat{a} \rightarrow \hat{a} e^{-i\omega_0 t}. \tag{2.14}$$

An unperturbed harmonic oscillator with no interactions with its environment or externally applied driving field ($\hat{V}_I(t) = 0$) will not move in this frame. However, any deviations of the actual oscillator frequency ω from the value ω_0 that defines the rotating frame will cause the Wigner function of the state to rotate about the origin at a rate $\delta\omega = \omega - \omega_0$. Throughout the remainder of this thesis we will use this interaction picture to describe the evolution of the quantum states.

In the next few sections, we will discuss a few special types of quantum states of motion, noting important features in their energy and phase-space representations.

2.3 Number states

As introduced above, number states are eigenstates of the harmonic oscillator Hamiltonian, and hence are rather boring in the energy basis. When we examine the Wigner functions (see Fig. 2.2) of this class of states, however, two important features of number states become apparent. First, the radial dependence of the Wigner function becomes more finely structured as we use increasingly high values of n. (This becomes intuitively clear when considering that integration of the Wigner functions along the momentum axis will yield the square modulus of the position wavefunctions (see Fig. 2.1 for the wavefunctions themselves).) Second, the Wigner functions have continuous azimuthal symmetry in phase space. These two features will become especially important when we discuss the proposed use of these states for quantum-enhanced force sensing later. The first feature gives us the

quantum enhancement, and the second allows us to use this quantum enhancement regardless of the phase of the displacement.

2.4 Number-state superpositions

Because of the quantum coherent interference between the different constituents of the superposition, the Wigner functions of states of the form $|0\rangle + |n\rangle$ (omitting normalization) exhibit features that are not present in a single number state alone. Chiefly, the continuous rotational symmetry in the single number state case instead becomes a discrete, n-fold symmetry (see Fig 2.3). We will discuss later how this can be used for quantum-enhanced measurements of the harmonic oscillator frequency.

2.5 Coherent states

The study of coherent states is a fascinating and rich area from both a physical and a mathematical perspective. We can derive many of their interesting qualities starting from the formal, mathematical definition of a coherent state: it is defined to be an eigenstate of the lowering operator $\hat{a}$:

$$\hat{a}|\alpha\rangle = \alpha|\alpha\rangle. \tag{2.15}$$

The form of $|\alpha\rangle$ that satisfies this relationship is

$$|\alpha\rangle = e^{-\frac{|\alpha|^2}{2}} \sum_{n=0}^{\infty} \frac{\alpha^n}{\sqrt{n!}}|n\rangle. \tag{2.16}$$

This is a Poissonian distribution over number states $|n\rangle$, with an average value $\langle\alpha|\hat{n}|\alpha\rangle = \bar{n} = |\alpha|^2$. This can be expressed in terms of the ground state wavefunction. Since $(\hat{a}^\dagger)^n|0\rangle =$

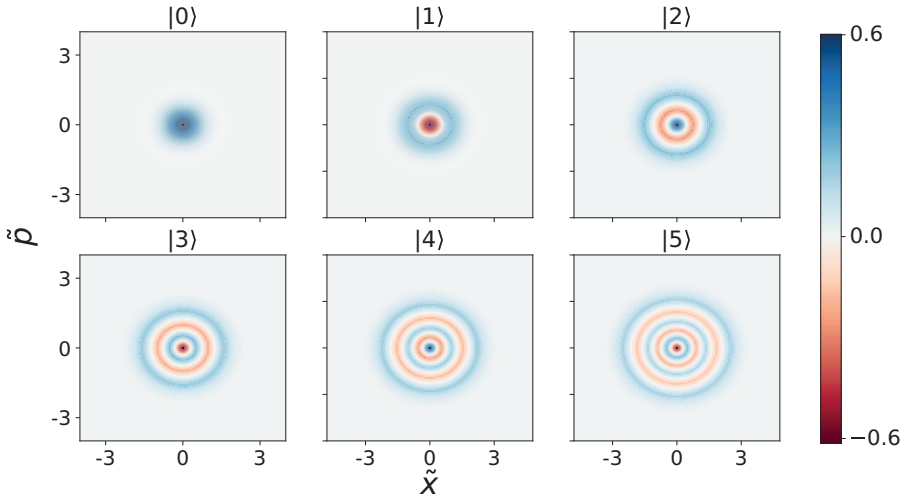

Figure 2.2: Wigner functions of first few harmonic oscillator number states, from $n = 0 - 5$. Salient features of number states are: azimuthal symmetry in phase space, and fine structure in the radial dependence of the Wigner function that increases in complexity with n. Both of these features are key to the metrological usefulness of these states and will be discussed in later chapters.

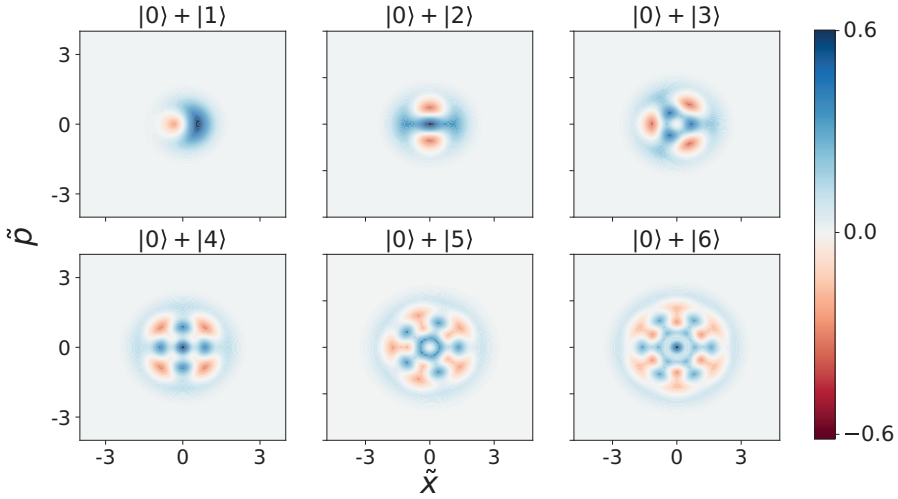

Figure 2.3: Wigner functions of superpositions of number states of the form $|0\rangle + |n\rangle$, with $n = 1 - 6$. While the single number states are azimuthally symmetric, the interference between the two components of these superpositions causes n-fold azimuthal symmetry, making the superposition states sensitive to rotations about the origin with a sensitivity that increases linearly with n. This will be discussed in more detail in later chapters.

$\sqrt{n!}|n\rangle$, from Eq. 2.16 we obtain:

$$|\alpha\rangle = e^{-\frac{|\alpha|^2}{2}} \sum_{n=0}^{\infty} \frac{(\alpha\hat{a}^\dagger)^n}{n!}|0\rangle = e^{-\frac{|\alpha|^2}{2}} e^{\alpha\hat{a}^\dagger}|0\rangle = e^{\alpha\hat{a}^\dagger - \alpha^*\hat{a}}|0\rangle \tag{2.17}$$

where the last step is completed by applying the Baker-Haussdorf Lemma [Sakurai, 1993]. The operator applied to the ground state is called the displacement operator $\hat{D}(\alpha) = e^{\alpha\hat{a}^\dagger - \alpha^*\hat{a}}$ because it displaces the ground state from the origin by an amount α in phase space (see Figure 2.4). For real α, the displacement is proportional to the momentum operator, enacting a translation along x, while purely imaginary α is proportional to the position operator and produces a momentum kick.

Let us now look at the dynamics of a displaced ground state, or coherent state. We find the expectation values $\langle\hat{x}\rangle$ and $\langle\hat{p}\rangle$ (calculated in the interaction picture):

$$\langle\alpha|\hat{x}|\alpha\rangle = \sqrt{\frac{\hbar}{2m\omega_0}}\langle\alpha|(\hat{a}e^{-i\omega_0 t} + \hat{a}^\dagger e^{i\omega_0 t})|\alpha\rangle = \sqrt{\frac{2\hbar}{m\omega_0}}|\alpha|\cos(\omega_0 t + \phi) \tag{2.18}$$

$$\langle\alpha|\hat{p}|\alpha\rangle = -i\sqrt{\frac{m\hbar\omega_0}{2}}\langle\alpha|(\hat{a}e^{i\omega_0 t} - \hat{a}^\dagger e^{-i\omega_0 t})|\alpha\rangle = \sqrt{\frac{m\hbar\omega_0}{2}}|\alpha|\sin(\omega_0 t + \phi), \tag{2.19}$$

with $\phi = Arg[\alpha]$. In scaled units the relation between α and the expectation values of position and momentum is particularly simple:

$$\langle\alpha|\tilde{x}|\alpha\rangle = Re[\alpha], \langle\alpha|\tilde{p}|\alpha\rangle = Im[\alpha]. \tag{2.20}$$

The position and momentum expectation values obey the classical equations of motion of an object undergoing simple harmonic motion, as in Eqs. 2.5 and 2.6, where $A = \sqrt{\frac{2\hbar}{m\omega_0}}|\alpha|$. The uncertainties in both quadratures, Δx and Δp, are:

$$\Delta x = \sqrt{|\langle\hat{x}\rangle^2 - \langle\hat{x}^2\rangle|} = \sqrt{\frac{\hbar}{2m\omega_0}} \tag{2.21}$$

$$\Delta p = \sqrt{|\langle\hat{p}\rangle^2 - \langle\hat{p}^2\rangle|} = \sqrt{\frac{\hbar m\omega_0}{2}}. \tag{2.22}$$

Notably, the time- and α-dependence drops out, leaving a state that, regardless of its amplitude of motion, satisfies the minimum uncertainty allowed by Heisenberg:

$$\Delta x \Delta p \geq \frac{\hbar}{2}, \Delta\tilde{x}\Delta\tilde{p} \geq \frac{1}{4}. \tag{2.23}$$

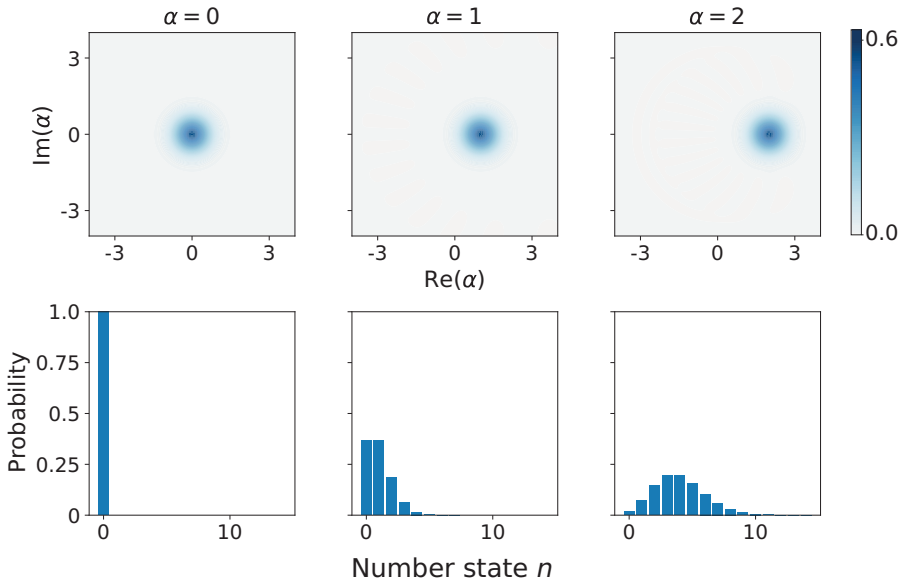

Figure 2.4: Wigner functions and corresponding number state populations of coherent states with $\alpha = 0$, 1, and 2. From the Wigner functions, one can see that the coherent states correspond to a ground state Wigner function that is displaced by amount α in phase space. The population follows a Poissonian distribution with the average $\bar{n} = |\alpha|^2$.

So, the dynamics of a coherent state can be described in phase space by a circular, minimum-uncertainty, Gaussian Wigner function travelling in circles in phase-space. In pictorial representations, the Wigner function is often replaced by a disk with a diameter corresponding to the width of the Gaussian.

To summarize, the key features of a coherent state are:

- it is an eigenstate of the lowering operator: satisfies $\hat{a}\,|\alpha\rangle = \alpha\,|\alpha\rangle$
- it is composed of a Poissonian distribution over number states with average value $\bar{n} = |\alpha|^2$
- it obeys classical equations of motion
- it has time-independent position and momentum uncertainties, with the minimum uncertainty allowed by the Heisenberg uncertainty principle, with time independent position and momentum uncertainties which are shared equally.

Because they are classically behaving states, they serve as a baseline when defining quantum advantages. A harmonic oscillator state is said to provide a quantum advantage if no coherent state exists that performs equally well for the task at hand. By definition, one cannot derive a quantum advantage from using these states for metrology, but as we will see in later chapters, the ease and speed with which these states can be produced can give a practical advantage in the lab over more exotic quantum states.

2.6 Displaced number states

In the previous section, we saw that a coherent state is generated by applying the displacement operator $\hat{D}(\alpha_d)$ to the ground state. What if instead we applied the displacement operator to a higher number state $|\Psi(0)\rangle = |n\rangle$? This would result in a more involved probability distribution over number states m [Carruthers and Nieto, 1965]:

$$P_m^{(n)} = \bar{n}^{|n-m|} e^{-\bar{n}} \frac{n_<!}{n_>!} (L_{n_<}^{|n-m|}(\bar{n}))^2, \tag{2.24}$$

where $\bar{n} = |\alpha_d|^2$, $n_<$ ($n_>$) is the lesser (greater) of the integers n and m and $L_n^a(x)$ is a generalized Laguerre polynomial.

The application of operators to quantum states of motion helps us expand our toolbox of quantum motional control and can be useful for future applications to other quantum-enhanced motional state metrology protocols.

2.7 Decoherence in quantum oscillators

There are two main types of motional decoherence in harmonic oscillators: one type either adds or subtracts energy to the oscillator, driving transitions between oscillator levels, while the other does not drive transitions between levels, but causes the phase evolution of the various energy levels to decohere. The former is driven by noise components at the oscillator frequency [Carruthers and Nieto, 1965] and is sometimes called dissipation, damping, or heating, and the latter is produced by noise at frequencies that differ from the oscillator frequency and is usually referred to as dephasing. When we think about how the different types of decoherence affect the Wigner functions of states in phase space, we note that, since the energy is proportional to the square of the magnitude of the displacement from the origin, $|\alpha|^2$, then the first type of decoherence, the dissipation, would act radially in phase space. By the same reasoning, dephasing must not have any radial component, since the

average energy of the state does not change, so dephasing causes only rotations around the origin in phase space.

2.8 Quantum vs. classical measurements

With the phase-space and Wigner functions introduced, we can now look at the difference between classical and quantum measurements more rigorously. As we have shown above, a coherent state of a quantum harmonic oscillator exhibits time-dependent expectation values consistent with classical mechanics, so if we compare the phase-space representation of these states with those of the other quantum states introduced in this chapter, we can determine situations in which other quantum states would be more metrologically useful than a classically behaving state.

A fundamental limit to how precisely we can measure an observable is given by the Heisenberg uncertainty principle. For a coherent, or classically behaving, state, the uncertainty disk is shared equally in both quadratures of phase space. If we have quantum control of the harmonic oscillator, then we can make a quantum state to "bend" the rules a bit. A classic example of this is squeezing, where the uncertainty in one of the quadratures of α is "squeezed" to less than $\sqrt{\hbar/2}$ at the cost of a greater uncertainty in the other quadrature. This allows us to measure either the position or the momentum of an oscillator with precision above the limits set by a coherent state, but not both [Caves et al., 1980].

In this spirit, we can also generate states of motion that allow us to measure other observables with higher precision than a classical experiment would allow. If we want to be maximally sensitive to the two different types of decoherence described previously (dissipation and dephasing), then we want to use states whose uncertainty is lowest in the direction

we would like to measure. If we want to measure dissipation, then we want a state that varies strongly in the radial direction, but is relatively insensitive to rotations. If we want to measure dephasing, the opposite is true: we want a state that is very sensitive to rotations but not as sensitive to radial displacements. These can both be achieved with number states $|n\rangle$ and superpositions of the form $|0\rangle + |n\rangle$, respectively (note the radial dependence of the Wigner functions in Fig. 2.2 and rotational dependence of the Wigner functions in Fig. 2.3). Comparing these Wigner functions to that of a coherent state (Fig. 2.4), we see that there is much finer structure in the more quantum-like states. This "sub-Planck" structure [Zurek, 2001] is one way of understanding the advantage gained when we use quantum states of motion.

Chapter 3

Beyond the 1-d oscillator model: trapped-ion harmonic oscillators

"Everything is a harmonic oscillator or a **two-level system**."

- Professor Thomas Degrand, University of Colorado, 2012.

In truth, as you will see, the trapped-ion system is a bit more complicated than either a harmonic oscillator or a two-level system. However, nearly all of the physics demonstrated in the experiments presented in later chapters can be distilled to a single harmonic oscillator coupled to a single two-level system. In this chapter, I will describe the physics that goes into trapping, cooling, and controlling the electronic and motional states of the ion in order to model the system in this simple way.

There are a few main elements of our system that complicate the simple 1-d oscillator model of the ion that we introduced in the previous chapter. First, the ion is in 3-d space, so it has 3 spatial motional degrees of freedom. Second, the way we generate some of the harmonic potential is by applying time-varying electric fields that oscillate at frequency $\Omega_T \gg \omega$. This causes the ion to perform oscillations at this higher frequency, called micromotion, on top of the slower, secular frequency ω of oscillation due to the time-averaged harmonic pseudopotential. Finally, our ability to control the motion of and learn information about the motional states of the ion is derived from coupling electronic and hyperfine states to the motion, so understanding the electronic states of our ion, in this case a beryllium ion, is

crucial to understanding the experiments.

3.1 Producing the harmonic potential – RF Paul traps

Owing to its nonzero net charge, an ion can be confined with certain configurations of electric fields. While static electric fields alone will not confine an ion in all three spatial dimensions simultaneously, we can set up a time-varying potential made up of an RF electric field that does confine the ion in 3-d. A simple way of demonstrating this concept is by imagining a frictionless ball sitting on the equilibrium position of a saddle-point potential under the influence of gravity (see Fig. 3.1). This potential is stable (confining) in one direction, but unstable (anti-confining) in the other direction. With any small displacement from the equilibrium position in the anti-confining direction, the ball will start to roll down the hill. But if we switch the polarity of the potential before the ball rolls a significant amount, then the previously anti-confining direction will now be confining and vice-versa, restoring the ball to the equilibrium position. If Ω_T is fast compared to the ball changing direction to roll downhill, then when averaged over one period $2\pi/\Omega_T$, the time-varying surface produces a confining pseudopotential.

In the same way, we a can set up a time-varying saddle potential for an ion using RF electric fields, which is the concept behind a Paul trap [Drees and Paul, 1964]. A linear Paul trap is composed of four linear rods, set up parallel and often equidistant to the z-axis (usually labelled the axial direction, while x and y are called the radial directions), on the lines $(x, y, z) = (\pm R, 0, z)$ and $(0, \pm R, z)$, with RF applied to the two rods intersecting the x-axis and the other two rods with static voltages applied (see Fig. 3.2). At a given time t,

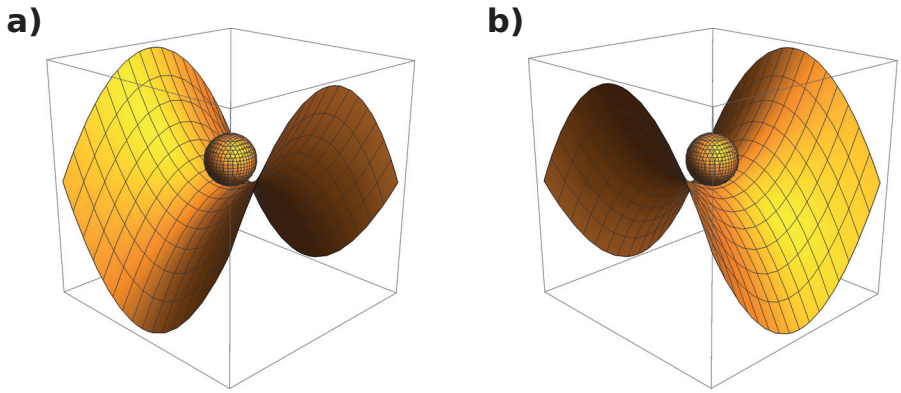

Figure 3.1: Schematic of a frictionless ball sitting on a saddle potential under influence of gravity depicting concept of a confining pseudopotential. a) At a given point in time, the potential is anti-confining in one direction, so the ball will start to roll downhill. b) If the polarity of the potential is switched fast enough, the direction the ball was originally rolling down is now confining and the ball will be forced towards its equilibrium position. If this polarity-switching is repeated periodically in time at a high enough rate, the flapping saddle produces a time-averaged confining pseudopotential that keeps the ball near the equilibrium position.

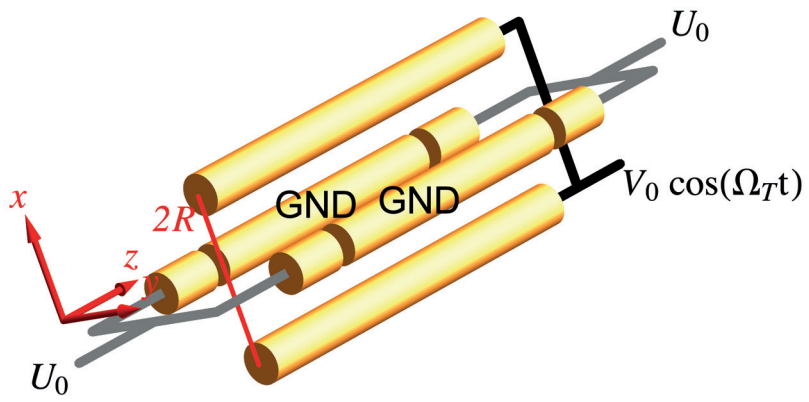

Figure 3.2: Schematic of a canonical linear RF Paul trap. It is composed of four linear rods, set up parallel and equidistant to the z-axis on the lines $(x, y, z) = (\pm R, 0, z)$ and $(0, \pm R, z)$. An RF potential $V_0 \cos(\Omega_T t)$ is applied to the two rods intersecting the x-axis and static voltages U_0 are applied to the four endcaps on the other two rods.

the potential that an ion positioned near the z-axis will feel is:

$$\Phi \simeq \frac{V_0 \cos(\Omega_T t)}{2}\left(1 + \frac{x^2 - y^2}{R'^2}\right), \tag{3.1}$$

where V_0 and Ω_T are, respectively, the amplitude and frequency of the RF potential applied to the the rods, and $R' = \kappa_{RF} R$, with κ_{RF} a geometric factor that depends on the shape, spacing, and orientation of the electrodes and is of order unity. In the z-direction, the potential is determined by a static electric field produced by the potential U_0 applied equally to all the endcap electrodes shown in Figure 3.2. The static potential produced from these electrodes is

$$\Phi_s = \kappa_{DC} U_0 \left[z^2 - \frac{1}{2}(x^2 + y^2)\right] \tag{3.2}$$

where κ_{DC} is a geometrical factor similar to κ_{RF}. In the axial direction, the potential is static and harmonic near the center of the trap, so that an ion obeys the standard harmonic oscillator equations of motion, with frequency of oscillation $\omega_z = \sqrt{2\kappa q U_0/m}$. The x- and y-dependent oscillating term from the RF potential means that the full, non-time-averaged motion in these directions is given by the Mathieu equations:

$$\frac{d^2x}{d\zeta^2} + \left[a_x + 2q_x \cos(2\zeta)\right]x = 0 \tag{3.3}$$

$$\frac{d^2y}{d\zeta^2} + \left[a_y + 2q_y \cos(2\zeta)\right]y = 0 \tag{3.4}$$

where the following substitutions were made:

$$\zeta = \frac{\Omega_T t}{2}, \tag{3.5}$$

$$a_x = \frac{4q}{m\Omega_T^2}(\kappa_{DC}\frac{U_0}{z_0^2}), \tag{3.6}$$

$$a_y = -\frac{4q}{m\Omega_T^2}(\kappa_{DC}\frac{U_0}{z_0^2}), \tag{3.7}$$

$$q_x = -q_y = \frac{2qV_0}{\Omega_T^2 m R'^2}. \tag{3.8}$$

General solutions to these equations can be found using the Floquet Theorem [Leibfried

et al., 2003; McLachlan, 1947]:

$$x_i(\zeta) = Ae^{i\beta_{x_i}\zeta} \sum_{n=-\infty}^{+\infty} C_{2n} e^{i2n\zeta} + Be^{-i\beta_i\zeta} \sum_{n=-\infty}^{+\infty} C_{2n} e^{-i2n\zeta} \tag{3.9}$$

for $x_i \in \{x, y\}$, and where β_{x_i} is a real-valued characteristic exponent and the coefficients C_{2n} are functions of a_x and q_x. Determining these coefficients based on boundary conditions is not straightforward and not especially illuminating, but in the special case where $|a_x|, |q_x|^2 \ll 1$, we can approximate the solution to lowest order in a_{x_i} and q_{x_i}:

$$x_i(t) \simeq 2AC_0 \cos\left(\beta_{x_i} \frac{\Omega_T}{2} t\right) \left[1 - \frac{q_{x_i}}{2} \cos\Omega_T t\right] \tag{3.10}$$

where $\beta_{x_i} \simeq \sqrt{a_{x_i} + q_{x_i}^2/2}$. Under these conditions, the trajectory of the ion in each radial direction is described by two different types of motion: first, the secular motion, which describes the harmonic motion from the ion moving in the pseudopotential created by the RF field. This frequency is $\omega_i = \beta_{x_i} \frac{\Omega_T}{2} \approx qV_0/(\sqrt{2}\Omega_T m R'^2)$. The second term describes the ion oscillating at the RF frequency Ω_T. This is known as micromotion, and is multiplied by a factor of $\frac{q_{x_i}}{2}$ compared with the secular motion. Given $|q_{x_i}| \ll 1$, this term can often be ignored, leaving us with an approximately harmonic 3-dimensional system defined by DC confinement in the axial direction, and RF pseudopotential confinement in the radial directions:

$$\Phi = \frac{1}{2} m(\omega_x x^2 + \omega_y y^2 + \omega_z z^2). \tag{3.11}$$

Two key features worth noting are:

- The radial secular frequencies of the ion depend inversely on the RF frequency Ω_T, mass m and the square of the distance R^2.
- The pseudopotential scales inversely with mass, so the strength of the radial confinement depends on the mass of the ion being confined.

Note that the approximation in Eq. 3.10 was performed at the location of the RF pseudopotential minimum. If the ion is significantly off of the minimum, micromotion will become much more of a concern. To minimize this effect, which typically appears in real traps due to stray fields or geometric imperfections of the electrode structures, we apply small correction voltages to overlap the static and RF potential minima. This is known as micromotion compensation and is an important calibration step before experiments are performed (see Sec. 4.8.3) .

All of the experiments presented in this thesis were performed using the axial motional mode, whose potential ideally is time-independent and only determined by static voltages. In this section we have shown that even the ion's radial confinement is harmonic under the right conditions, so all of the experiments should also be possible to implement on a radial mode of the ion.

3.2 Beryllium electronic structure

In order to cool the ion and generate non-classical states of motion, we use the ion's electronic structure to address certain internal transitions which are modified by or selectively allowed depending on the motional state of the ion. Singly-ionized ^{9}Be has a number of features that are advantageous in demonstrating motional state control. First, it has a single valence electron, so its electronic structure resembles that of alkali atoms (see Figure 3.2). The $1^2S_{1/2} \leftrightarrow 2^2P_{3/2}$ transition is dipole allowed, with a natural linewidth of $\Gamma = 2\pi \times 19.4$ MHz. This transition has a very high photon scattering rate because of the short excited-state lifetime, which makes it convenient for fluorescence detection and Doppler cooling.

A second feature that we exploit throughout this thesis is the non-zero nuclear spin, $I = 3/2$.

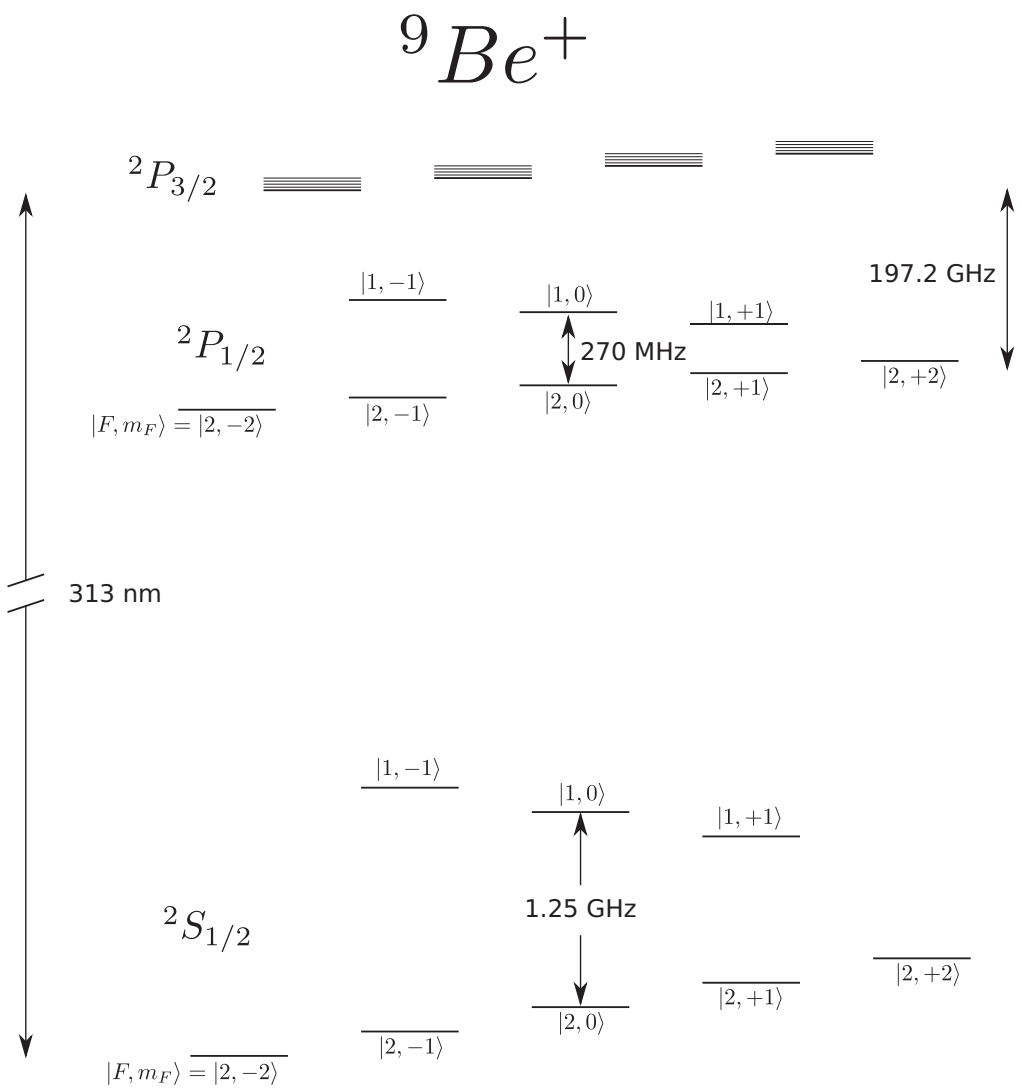

Figure 3.3: Energy level structure of singly ionized ^{9}Be. The nuclear spin is $I = 3/2$, leading to hyperfine structure. A weak magnetic field Zeeman splits the degeneracy of the m_F sublevels. This figure is adapted from reference [Jost, 2001].

This leads to hyperfine sublevels in the ground state that have extremely long lifetimes. Having a long-lived, effective two-level system which can be coupled to the motion of the ion is essential to all of the experiments in this thesis.

We will now examine this electronic structure, noting shifts and splittings in energy levels due to coupling between different excitations. The three energy levels we are concerned with are (in spectroscopic notation, $n^{2S+1}L_J$) $1^2S_{1/2}$, $2^2P_{1/2}$ and $2^2P_{3/2}$. Here, S is the quantum number denoting the spin of the electronic state, L is the orbital angular momentum, and $J = L + S$ is the total electronic angular momentum. The coupling of the electron's spin to the orbital angular momentum, given by the Hamiltonian [Griffiths, 2005]:

$$H_{so} = \left(\frac{e^2}{8\pi\epsilon_0}\right)\frac{1}{m^2c^2r^3}\mathbf{S}\cdot\mathbf{L} \tag{3.12}$$

which causes the 197.2 GHz splitting between the $^2P_{1/2}$ and $^2P_{3/2}$ levels. The electron's spin also couples to the nuclear spin, producing the hyperfine splitting.

$$H_{hf} = hA\mathbf{J}\cdot\mathbf{I} \tag{3.13}$$

where A is the hyperfine constant. In singly-ionized ^{9}Be, the nuclear spin is $I = 3/2$. The hyperfine splitting in the ground state is 1.25 GHz, in the $P_{1/2}$ state the hyperfine splitting is 237 MHz, and in the $P_{3/2}$ state the splitting is less than 1 MHz [Langer, 2006].

In the presence of a weak external field in the z-direction, the different hyperfine sublevels $|F, m_F\rangle$ with m_F describing the magnitude of the z-projection of the angular momentum quantum number F, will experience Zeeman splitting $E_Z = -g_F\mu_B m_F B$ [Griffiths, 2005], where $\mu_B = \frac{e}{2m}$ is the Bohr magneton and g_F is the g-factor. For the ground state of beryllium, g_F is $-1/2$ and $+1/2$ for F = 2 and F = 1, respectively [Langer, 2006]. We apply a field of 14.3 Gauss, so the low-field Zeeman approximation is appropriate, and the splitting in the ground state between neighboring Zeeman sublevels is approximately 10 MHz.

Finally, while we will not go into the mathematical details here, it is worth noting that the RF fields that confine the ion also cause a small amount of mixing between m_F sublevels in the trap we used for our experiments. This means that transitions that otherwise would not be allowed are weakly allowed. We will see the effect of this when looking at state-selective fluorescence later.

3.3 Doppler Cooling

To have full control of the motion of a trapped ion, we must first be able to cool the ion to its ground state. Doppler cooling is the first step in this process. First proposed in 1975 [Wineland and Dehmelt, 1975; Hänsch and Schawlow, 1975] and demonstrated in [Wineland et al., 1978; Neuhauser et al., 1978], the basic idea behind this method of cooling is to use the momentum of a photon to damp the motion of the ion. If we imagine the ion oscillating back and forth in one dimension, with laser light at frequency ω_L incident on the ion from the right (see Figure 3.4), then, in order to damp the motion rather than amplify it, we would like the ion to preferentially absorb light when it is moving in the direction opposite to the photon's momentum. We can do this by choosing a laser frequency close to, but lower than, a resonant transition in the ion. So when the ion is moving to the right in Fig. 3.4, the frequency of the photons is Doppler shifted closer to resonance in its reference frame, which increases the probability of absorbing the photon and experiencing a momentum kick against the direction of motion of the ion. When the ion moves in the opposite direction, the probability of absorption is lowered, so on average a moving ion experiences more momentum kicks that slow it down than those that speed it up.

Each absorption event is accompanied by an emission event that ejects a photon in an

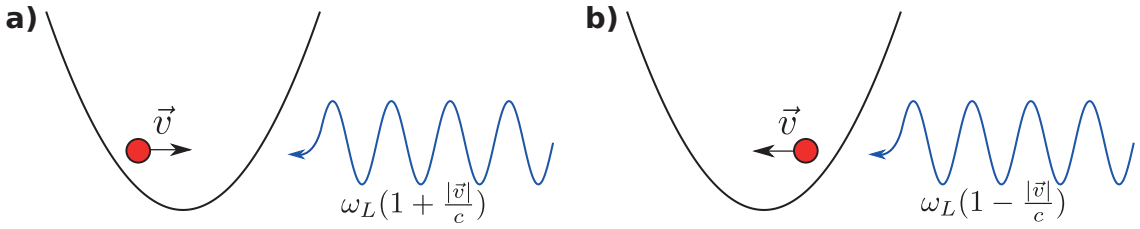

Figure 3.4: Schematic sketch depicting velocity-selective absorption of Doppler cooling light. If the light is red-detuned from an electronic transition, and a) the ion is moving with velocity $\vec{v}$ in the direction opposite the laser k-vector, then in the frame at rest with ion, the photons will be Doppler-shifted toward resonance, increasing the probability of absorption and the ion receiving a momentum kick in the direction opposite the ion's motion. b) If the ion is moving in the same direction as the k-vector, then the laser will be Doppler shifted further from resonance and the ion will be less likely to absorb a photon.

approximately random direction—this causes the ion to heat by an amount $\frac{(\hbar k)^2}{2m}$ from the recoil energy of the emitted photon, where k is the wavevector of the emitted photon and m is the mass of the atom. Because of this heating mechanism, there is a limit to the temperature that can be achieved by Doppler cooling. Following [Leibfried et al., 2003], we will now derive the minimum temperature that can be achieved with Doppler cooling in the case of an ion trapped in a one-dimensional harmonic potential:

$$V(z) = \frac{1}{2} m \omega_z^2 z^2 \tag{3.14}$$

where m and ω_z are the ion's mass and frequency of oscillation, respectively. The ion's velocity will obey simple harmonic motion:

$$v(t) = v_0 cos(\omega_z t). \tag{3.15}$$

Obviously, this is a very simplistic model—a more realistic model of a trapped ion would include all 3 modes of oscillation, the existence of micromotion, and other electronic energy levels that off-resonantly couple to the Doppler cooling light field. Nevertheless, this simplistic approach allows us to examine the physics which limits Doppler cooling, motivating the need for another method of laser cooling to reach the ground state (see next section).

We assume the weak binding limit, $\omega_z \ll \Gamma$, where Γ is the linewidth of the atomic transition. This means that a photon is absorbed and reemitted much faster than a period of mechanical oscillation. In our experiments, we use the $^2S_{1/2} \leftrightarrow {}^2P_{3/2}$ transition, so $\Gamma = 2\pi \times 19.4$ MHz. The frequency of oscillation in the axial direction is approximately 7-8 MHz, so this weak binding limit should be valid. In this limit, we can model the radiation pressure as a continuous force that depends on the velocity of the ion. This force is equal to the momentum transferred to the ion with each absorption event times the rate of absorption-emission cycles:

$$\langle F \rangle_{abs} = \hbar k \Gamma \rho_{ee} \tag{3.16}$$

where $\rho_{ee} = \langle e|\rho|e\rangle$ is the probability of being in the excited state (with ρ the density matrix of the electronic states of the ion and $|e\rangle$ denoting the excited $^2P_{3/2}$ state). With each absorption event, a photon is reemitted, but since the direction of the reemission is symmetric in z, the force the atom feels from emission is averaged to zero.

When the ion is illuminated with a laser beam traveling in the $+z$ direction, with saturation parameter $s = 2|\Omega|^2/\Gamma^2$, where Ω is the on-resonance Rabi frequency, this probability is:

$$\rho_{ee} = \frac{s/2}{1 + s + (2\delta_{eff}/\Gamma)^2} \tag{3.17}$$

where δ_{eff} is effective detuning from resonance, taking into account the Doppler shift of the light field from the reference frame of the moving ion:

$$\delta_{eff} \approx \Delta - kv_z \tag{3.18}$$

and Δ is the detuning in the lab frame, assuming $v_z \ll c$. If we also assume the velocity is low enough that the effect from Doppler broadening is much less that the linewidth Γ, then we can linearize the force in v_z:

$$F \approx F_0(1 + \kappa v_z) \tag{3.19}$$

where

$$F_0 = \hbar k\Gamma \frac{s/2}{1 + s + (2\Delta/\Gamma)^2} \tag{3.20}$$

is the velocity-independent, average radiation pressure that displaces the ion's equilibrium position by a small amount, and

$$\kappa = \frac{8k\Delta/\Gamma^2}{1 + s + (2\Delta/\Gamma)^2} \tag{3.21}$$

is a "friction coefficient" which leads to damping when $\Delta < 0$. The cooling rate, averaged over many oscillation periods is

$$\dot{E}_c = \langle F_a v_z\rangle \approx F_0(\langle v_z\rangle + \kappa\langle v_z^2\rangle) = F_0\kappa\langle v_z^2\rangle \tag{3.22}$$

since $\langle v_z \rangle = 0$ for a confined particle. This treatment neglects that the laser beam also acts as a heating source, particularly as $v_z \to 0$. When $v = 0$, *every* absorption or emission event will cause the ion to heat from the photon recoil. Even when v_z is non-zero, but small, the relatively broad linewidth Γ of most transitions that are used in Doppler cooling means that some absorbed photons will actually contribute to heating the ion (the ion is traveling in the same direction as the photon-momentum kick) rather than cooling. To get a sense for the magnitude of these heating events, let us look at the heating rates of the absorption and emission when $v_z = 0$. The change in the ion's energy from each absorption-emission cycle is:

$$\dot{E}_h = \frac{1}{2m}\frac{d\langle p^2 \rangle}{dt} = \dot{E}_{abs} + \dot{E}_{em} = \dot{E}_{abs}(1+\xi) = \frac{1+\xi}{2m}\hbar^2 k^2 \Gamma \rho_{ee}(v=0) \tag{3.23}$$

where the factor of ξ is inserted to take into account the fact that while the photon momentum kick from an absorption event will always be purely along $\hat{z}$ since the laser beam is pointed in the $-z$ direction, the photon can be reemitted into free space, so some of the emitted photon's recoil momentum will not contribute to heating in the z direction.

The ion will arrive at a steady-state energy when the cooling (Eq. 3.22) and heating (Eq. 3.23) rates are balanced:

$$m\langle v_z^2 \rangle = k_B T = \frac{\Gamma}{8}(1+\xi)\left[(1+s)\frac{\Gamma}{2\Delta} + \frac{2\Delta}{\Gamma}\right] \tag{3.24}$$

For a low saturation parameter, the lowest temperature is achieved when $\Delta = \Gamma/2$, which, for $\Gamma = 2\pi \times 19.4$ MHz and $\zeta = 2/5$ (for dipole radiation where the dipole is oriented along z), leads to $T \approx 1$ mK.

3.3.1 Doppler cooling in ^{9}Be$^+$

We made many assumptions in our treatment of Doppler cooling above, many of which do not perfectly hold in beryllium. One of the main assumptions that is broken is that the system can be isolated to only two electronic energy levels. As is apparent from Sec. 3.3 above, there are many hyperfine sublevels in the ground state that the ion can fall into upon the reemission of the photon. By making the polarization of the Doppler beam σ^-, the ion nearly always stays in the $^2S_{1/2}\,|2,-2\rangle \leftrightarrow\ ^2P_{3/2}\,|3,-3\rangle$ cycling transition, but occasionally, due to polarization imperfections or the RF-induced mixing of the m_F sublevels mentioned in Sec. 3.2, the ion will scatter into one of the other hyperfine states. This makes the situation significantly more complicated and I will not cover the technical details here, but by applying other laser beams resonant with the $^2S_{1/2}\,|2,-1\rangle \leftrightarrow\ ^2P_{1/2}$ and $^2S_{1/2}\,|1,-1\rangle \leftrightarrow\ ^2P_{1/2}$ transitions, we can "repump" population that has fallen outside of the cycling transition back to $^2S_{1/2}\,|2,-2\rangle$.

3.4 Stimulated Raman transitions

To cool from the Doppler temperature to the ground state of motion, we need a transition with a narrow linewidth so that nearly *every* scattered photon contributes to cooling—this is known as the resolved sideband limit. In this limit, we can tune the frequency of the laser to $\omega_L = \omega_{\downarrow\uparrow} - \omega_z$, where $\omega_{\downarrow\uparrow}$ is the frequency of the transition between the ground and excited states, and ω_z is the ion's oscillation frequency, so that each absorbed photon transfers the ion to the excited state and removes a quantum of motional energy. In $^9Be^+$, the narrow linewidth transition we use is a coherent two-photon transition between the hyperfine levels $|F, m_F\rangle = |2,-2\rangle$ and $|1,-1\rangle$ of the $^2S_{1/2}$ ground state, via a virtual excitation to the $^2P_{1/2}$ level. There are three relevant electronic energy levels: $|\downarrow\rangle = |2,-2\rangle$, $|\uparrow\rangle = |1,-1\rangle$, and

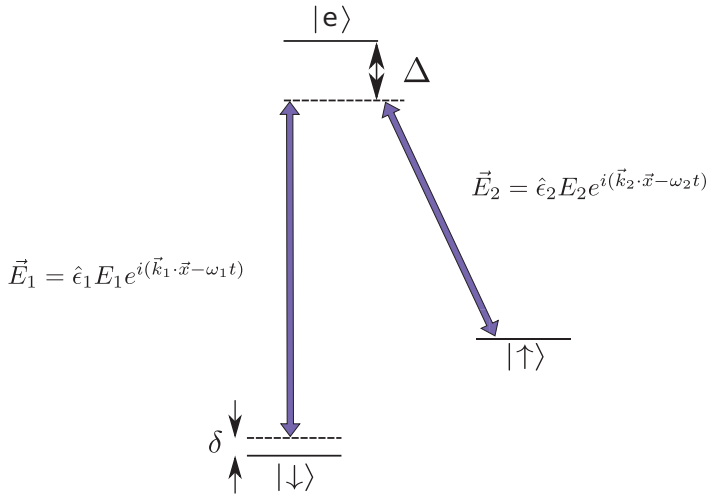

Figure 3.5: Schematic of a two-photon stimulated Raman transition from $|\uparrow\rangle$ to $|\downarrow\rangle$, via a third level, $|e\rangle$. The frequencies of the two laser beams are depicted by the length of the two purple arrows.

$|e\rangle = {}^2P_{1/2}$, as shown in Fig. 3.5. We perform a Raman transition $|\downarrow\rangle \leftrightarrow |\uparrow\rangle$ by applying two laser beams with frequencies $\omega_1 = \omega_e - \omega_\downarrow - \delta - \Delta$ and $\omega_2 = \omega_e - \omega_\uparrow - \Delta$ (also shown in Fig. 3.5).

The Hamiltonian that describes this interaction is given by:

$$H_I = -\vec{\mu} \cdot \vec{E} = -\vec{\mu} \cdot (\hat{\epsilon}_1 E_1 e^{i(\vec{k}_1 \cdot \vec{z} - \omega_1 t + \phi_1)} + \hat{\epsilon}_2 E_2 e^{i(\vec{k}_2 \cdot \vec{z} - \omega_2 t + \phi_2)}) + H.C. \tag{3.25}$$

where $\vec{\mu}$ is the electric dipole moment corresponding to the transition and $E_{1,2}$, $\hat{\epsilon}_{1,2}$, $\vec{k}_{1,2}$, and $\phi_{1,2}$ are, respectively, the amplitude, polarization, k-vector, and phase of the electric field from the laser with frequency $\omega_{1,2}$. Transforming to the interaction picture, defined by $H_0 = \hbar(\omega_\downarrow |\downarrow\rangle \langle\downarrow| + \omega_\uparrow |\uparrow\rangle \langle\uparrow| + \omega_e |e\rangle \langle e|$, this becomes

$$H_{int} = \hbar g_1 e^{i\vec{k}_1 \cdot \vec{z} + \phi_1} e^{i\Delta t} |\downarrow\rangle \langle e| + \hbar g_2 e^{i\vec{k}_2 \cdot \vec{z} + \phi_2} e^{i\Delta t} |\uparrow\rangle \langle e| + H.C. \tag{3.26}$$

where

$$g_1 = -\frac{E_1}{2\hbar} \langle\downarrow |\vec{\mu} \cdot \vec{\epsilon}_1| e\rangle \tag{3.27}$$

$$g_2 = -\frac{E_2}{2\hbar} \langle\uparrow |\vec{\mu} \cdot \vec{\epsilon}_2| e\rangle. \tag{3.28}$$

If the detuning Δ of the laser beams from the excited state $|e\rangle$ is large enough, then we can assume that $|e\rangle$ is negligibly populated and our relevant system reduces to the two-level subsystem of $|\downarrow\rangle$ and $|\uparrow\rangle$. This is known as adiabatic elimination—we will not go through the derivation here, as it can be found in Ref. [Wineland et al., 1998; Wineland, 2003]. This gives rise to an effective coupling between $|\downarrow\rangle$ and $|\uparrow\rangle$:

$$H_{int,eff} = -\hbar \left[\frac{|g_1|^2}{\Delta} |\downarrow\rangle \langle\downarrow| + \frac{g_1 g_2^*}{\Delta} e^{-i\delta t} |\downarrow\rangle \langle\uparrow| e^{-i(\vec{\Delta k} \cdot \vec{z} + \delta\phi)} + \frac{g_2 g_1^*}{\Delta} e^{i\delta t} |\uparrow\rangle \langle\downarrow| e^{i(\vec{\Delta k} \cdot \vec{z} + \delta\phi)} + \frac{|g_2|^2}{\Delta} |\uparrow\rangle \langle\uparrow| \right] \tag{3.29}$$

where $\vec{\Delta k} = \vec{k}_1 - \vec{k}_2$, $\delta = \omega_{\downarrow\uparrow} - (\omega_1 - \omega_2)$, and $\delta\phi = \phi_1 - \phi_2$. This equation captures two phenomena—the first and last terms describes an energy shift of the two levels due to the off-resonant coupling between $|e\rangle$ and either $|\downarrow\rangle$ or $|\uparrow\rangle$, or an AC Stark shift. Because the

values g_1 and g_2 depend on the intensity and polarization of laser light used, we can adjust the relative intensities and polarizations between the beams such that the difference in Stark shifts between $|\uparrow\rangle$ and $|\downarrow\rangle$ can be minimized. We can absorb these terms into H_0, leaving only the off-diagonal elements, which describe coupling between $|\downarrow\rangle$ and $|\uparrow\rangle$, with Rabi frequency $\Omega_0 = -g_1 g_2^*/\Delta$.

Since this is now effectively a two-level system, we can write the Hamiltonian in terms of the Pauli matrices:

$$\hat{\sigma}_z = \begin{pmatrix} 1 & 0 \\ 0 & -1 \end{pmatrix}, \ \hat{\sigma}_x = \begin{pmatrix} 0 & 1 \\ 1 & 0 \end{pmatrix}, \ \hat{\sigma}_y = \begin{pmatrix} 0 & -i \\ i & 0 \end{pmatrix}. \tag{3.30}$$

So Eq. 3.29 can be written as:

$$H_{int} = \hbar\Omega_0(\hat{\sigma}_- e^{-i(\delta t + \vec{\Delta k}\cdot\vec{z} + \delta\phi)} + \hat{\sigma}_+ e^{-i(\delta t + \vec{\Delta k}\cdot\vec{z} + \delta\phi)}) \tag{3.31}$$

where $\hat{\sigma}_\pm = 1/2(\hat{\sigma}_x \pm i\hat{\sigma}_y)$. We also want to include the motional energy in the Hamiltonian that defines the interaction frame. In Ch. 2, we used the variable ω_0 for this frequency. However, for the purposes of deriving the Raman interactions which couple to the motion, we will assume a perfect harmonic oscillator with no mode frequency noise, so we define $\omega_0 = \omega_z$. The new unperturbed, time-independent part of the Hamiltonian which will define our interaction frame is now (rescaling the electronic part by $\frac{\hbar\omega_{\uparrow\downarrow}}{2}$ and neglecting the $\frac{\hbar\omega_z}{2}$ harmonic oscillator zero-point energy)

$$H_0 = H^{(e)} + H^{(m)} = \hbar\frac{\omega_{\downarrow\uparrow}}{2}\hat{\sigma}_z + \hbar\omega_z\hat{a}^\dagger\hat{a} \tag{3.32}$$

In the new interaction frame, the time-independent position operator $\vec{z}$ is replaced with the time-dependent Heisenberg position operator $\vec{z}(t) = z_0(\hat{a}e^{-i\omega_z t} + \hat{a}^\dagger e^{i\omega_z t})$, where $z_0 = \sqrt{\frac{\hbar}{2m\omega_z}}$. Eq. 3.31 becomes:

$$H_{int} = (\hbar/2)\Omega_0\sigma_+ \exp[i\eta(\hat{a}e^{-i\omega_z t} + \hat{a}^\dagger e^{i\omega_z t})]e^{i(\delta\phi - \delta t)} + H.C. \tag{3.33}$$

where $\delta = \omega - \omega_{\downarrow\uparrow}$ and $\eta = \vec{\Delta k}\cdot\vec{z_0}$ is the Lamb-Dicke parameter, which is the ratio of the extent of the ion's ground state spatial wavefunction to the effective wavelength of the

Raman beams $2\pi/\Delta k$. When the detuning $\delta = m\omega_z$ with m an integer, then the Raman coupling is resonant with a transition between $|\downarrow\rangle|n\rangle$ and $|\uparrow\rangle|n+m\rangle$. When $m = 0$, no motional energy is exchanged and we call this a carrier transition. When $m > 0$ ($m < 0$), we call this a blue (red) sideband since it is blue (red) detuned from the carrier. We often refer to the magnitude $|m|$ as the *order* of the sideband, denoting the number of quanta that are added or subtracted with a single π-pulse.

3.4.1 Lamb-Dicke Approximation

If the effective wavelength of the Raman beams $2\pi/\Delta k$ is much larger than the extent of the ion's spatial wavefunction, then the ion experiences only a small part of the laser beam intensity pattern (see Fig. 3.6 a) and b)) and we can apply the Lamb-Dicke approximation, expanding the exponentials that describe the spatial intensity pattern of the light in Eq. 3.33 to lowest order:

$$H_{int}^{LD} = (\hbar/2)\Omega_0\sigma_+[1 + i\eta(\hat{a}e^{-i\omega_z t} + \hat{a}^\dagger e^{i\omega_z t})]e^{i(\phi-\delta t)} + H.C. \tag{3.34}$$

So the Rabi frequency of a transition between number states $|n-1\rangle$ and $|n\rangle$ will be proportional to $\sqrt{n}$ in the Lamb-Dicke regime.

3.4.2 Ground state cooling

After Doppler cooling to $\sim$1 mK (typically corresponding to $\bar{n} \approx 0.2 - 5$), we cool to close to the ground state by Raman sideband cooling. By using these extremely narrow[1] Raman transitions, we are deep in the resolved sideband regime, so nearly every scat-

[1] Since both states coupled by the transition are stable ground states, the spectral width of the transitions is determined by the Fourier transform of the envelope of the laser pulses driving the Raman transitions. In

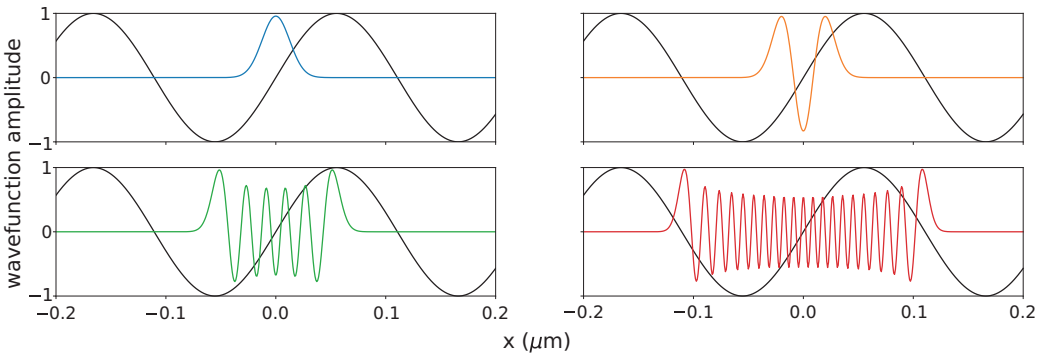

Figure 3.6: Spatial wavefunction (shown in colors) extent in a $\omega_0 = 2\pi \times 7$ MHz oscillator mode for $^9Be^+$ compared with Raman laser effective wavelength $2\pi/\Delta k$, with $\lambda_1 \simeq \lambda_2$ 313 nm and a 90 degree angle between k_1 and k_2 for number states a) $n = 0$, b) $n = 2$, c) $n = 10$, and d) $n = 40$. a) and b) For small spatial wavefunction extent compared with the wavelength, the laser intensity pattern can be approximated to be linear across the ion's wavefunction (Lamb-Dicke approximation). c) and d) As the number state increases, the wavefunction becomes more extended, so the ion sees more of the sinusoidal intensity pattern of the Raman field, and this approximation no longer holds.

tered photon contributes to cooling, suppressing many of the heating mechanisms that were present in Doppler cooling. We sideband cool by applying an approximate π-pulse on the red sideband (RSB) $|\downarrow\rangle|n\rangle \leftrightarrow |\uparrow\rangle|n-1\rangle$, then using repump beam $|\uparrow\rangle \rightarrow {}^2\mathrm{P}_{1/2}|2,-2\rangle$. The ion will decay to the ground state after scattering an average of 3 repump photons, at which point the sideband π-pulse and repump procedure can be repeated. The optimal number and duration of pulses depend on the $\bar{n}$ of the Doppler cooling limit prior to sideband cooling and the magnitude and behavior of the heating mechanisms. I will now qualitatively discuss the main heating sources that will ultimately limit the achievable temperature.

First, while the repump lasers are necessary for performing multiple sideband cooling cycles, they also contribute to heating the ion. This energy will be removed in the following RSB pulse with very high probability, except for the final repump pulse, which is not followed by a RSB pulse. For this final repump step, the probability of the repump interacting with the ion is very low, since the majority of the population will be in $|\downarrow\rangle|n=0\rangle$. If, however, the ion is found to be in $|\uparrow\rangle$, then this final repump step will impart $\bar{n} = \beta\frac{\hbar k^2}{2m\omega_z} \approx 0.05$ quanta of energy on the ion, assuming $\omega_z = 2\pi \times 7$ MHz and β is a factor of order 1 depending on the k-vector of the repump beam and directionality of the spontaneous emission event relative to the mode being cooled, and the average number of repump photons scattered before the ion decays to the desired $|\downarrow\rangle$ state. Components of the directions of the absorbed and spontaneously emitted photons that are not along the mode direction will contribute to heating the other modes.

Second, there is some probability of off-resonantly exciting the carrier or blue sideband (BSB), but this is detuned by $\delta = \omega_z$ and $\delta = 2\omega_z$, respectively, so is suppressed by $\mathrm{sinc}^2(\frac{\delta}{\Omega})$,

this work, we mostly used square pulses which have a Fourier transform proportional to $\sin(T(\omega-\omega_0))/(\omega-\omega_0)$, where ω_0 is the frequency of the carrier oscillations under the envelope and T the pulse duration.

where Ω is the Rabi frequency of the respective off-resonant transition.[2] We want to maintain a low Rabi frequency relative to the oscillation frequency to keep the probability of exciting the off-resonant carrier and BSB low. It is also worth considering the Raman intensity, which dictates the π-time t_π of the Raman interactions. The off-resonant excitation probability will be enhanced if the mode frequency falls on a peak of one of the side-lobes of the sinc^2-lineshape, which occur at $(k + 1/2)/t_\pi$ for k an integer, while it can be zero if the mode-frequency co-incides with a zero of the lineshape.

Finally, the ion suffers heating from the electric field noise from the surface of the trap chip, so the slower the cooling process, the higher the final temperature will be because of this heating rate. Finding the Raman sideband Rabi frequency that achieves a compromise between avoiding too much heating during the cooling process and higher BSB excitation probability is necessary for achieving the lowest possible $\bar{n}$.

3.4.3 Raman interactions outside the Lamb-Dicke regime

Even if we are operating with a fairly low Lamb-Dicke parameter, as n increases, the spatial wavefunction will spread out more and more, sampling larger parts of the laser beam intensity profile, and the Lamb-Dicke approximation will become less and less valid (see Fig. 3.6). In this case, we can no longer approximate the exponential function by its leading linear tem as in Eq. 3.34, and we must keep higher-order terms in the expansion. Without the Lamb-Dicke approximation, the 2-level interaction Hamiltonian is given by Eq. 3.33. A

[2] Eq. 3.34 implies that the blue sideband Rabi frequency is reduced relative to the carrier by a factor $\eta < 1$, so typically off-resonant carrier excitation is the dominant process. For this to contribute to heating, the ion has to scatter on a blue sideband during repumping, which hapens with probability $3\eta_r^2$, where $\eta_r < 1$ is the Lamb-Dicke parameter of the repump laser. After an off-resonant transition on the BSB, the ion has picked up a quantum already and is most likely to be repumped on the carrier (probability $(1 - \eta_r^2)^3 \simeq 1 - 3\eta_r^2$).

resonant transition between $|\downarrow\rangle|n\rangle$ and $|\uparrow\rangle|n+m\rangle$ can be driven when the detuning is an integer multiple of the oscillation frequency, $\delta = m\omega_z$. We can find the Rabi frequencies for a transition at a given starting number state n by expanding the exponential and reordering according to the "order" of the transition, or the change in n, of each term [Wineland et al., 1998; Leibfried et al., 2003]. The Rabi frequency for the mth order transition from level n is

$$\Omega_{n,n+m} = \Omega_0 |\langle n+m|e^{i\eta(\hat{a}+\hat{a}^\dagger)}|n\rangle| = \Omega_0 e^{-\eta^2/2}\eta^{|m|}\sqrt{\frac{n_<!}{n_>!}}L_{n_<}^{|m|}(\eta^2), \tag{3.35}$$

where $n_<$ ($n_>$) is the lesser (greater) of $n+m$ and n, and $L_n^\alpha(x)$ is a generalized Laguerre polynomial. Changes in the Rabi frequency with n are plotted for different Lamb-Dicke parameters in Fig. 3.7.

3.5 Microwave transitions

A final tool in our ion-control toolbox is the use of microwaves to couple between pairs of the sublevels in the ground state hyperfine manifolds. It is important to be able to initialize the desired internal state before any subsequent steps involving controlling the motion of the ion, because whether a sideband interactionadds or subtracts a quantum of motion depends on the initial internal state of the ion. In principle, we could use Raman carrier transitions for initialization, but the polarization of the Raman beams was chosen to maximally drive the $|2,-2\rangle \leftrightarrow |1,-1\rangle$ transition and to minimize AC Stark shifts, so only certain transitions can be driven. For example, since one beam has only σ_+ and σ_--polarized light and the other has only π-polarized light, only transitions where $\Delta m_F = \pm 1$ can be driven with the beams. If, however, we deliver microwaves to the ion with an electrode whose B-field has components both along and perpendicular to the quantization axis, then $\Delta m_F = 0$ transitions can be driven in addition to the $\Delta m_F = \pm 1$ transitions. Another reason that microwaves are preferred over Raman beams for carrier transitions is that the Raman beams

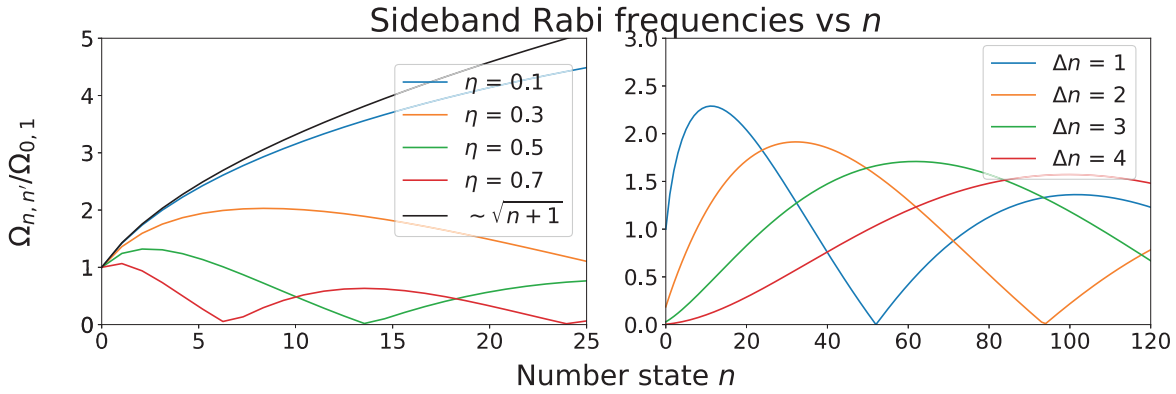

Figure 3.7: Rabi frequencies versus number state n, without the Lamb-Dicke approximation. a) Rabi frequency on the first blue sideband ($\Delta n = 1$) vs. n for different Lamb-Dicke parameters, compared with Lamb-Dicke approximation, the $\sim 1/\sqrt{(n+1)}$ line (black). b) Rabi frequency using the experimental value of $\eta \approx 0.26$ vs. n for different order sideband transitions $\Delta n = 1 - 4$.

are not infinitely detuned from the intermediate level, so the Raman transitions will suffer from spontaneous emission from this level, leading to imperfections in the Raman operations. Microwaves do not have this drawback.

We do not use the microwaves for sideband transitions. In order to be able to do this, we would need a sizable oscillating magnetic field gradient that would provide the coupling between the ion's motion and its internal energy levels, which can be difficult to achieve. While this is not an area of investigation for this thesis, this approach is being pursued by several groups [Ospelkaus et al., 2011; Harty et al., 2016] including our own [Srinivas et al., 2019], and is a promising avenue for many ion trap experiments in the future.

Chapter 4

Apparatus

Most of my work done in the Ion Storage Group falls into one of two categories: first, experiments involving the motion of a single trapped ion in a linear surface electrode trap, and second, updates made to the apparatus to accomodate a new generation of surface electrode traps for two-dimensional arrays of ions. Because of this, in this chapter, I will be describing older versions of the setup that were used in the experiments I performed and updates I and others have made in anticipation of working with future traps with larger numbers of electrodes.

4.1 Surface electrode traps

In Section 3.1, I used the canonical linear RF Paul trap geometry to describe how RF fields generate the pseudopotential that confines the ions. However, if we would like to develop a scalable architecture for trapped-ion quantum computing, then fabricating ion traps on a single, two-dimensional, microfabricated surface would be advantageous. Among other advantages, this allows us to have precise individual control of each ion's trapping potential while still maintaining a close ion-to-ion distance, and hence sufficient Coulomb coupling, between ions. Microfabricated surface-electrode traps allow us to make very small electrodes to give us this fine control of individual ions [Chiaverini et al., 2005; Seidelin et al., 2006].

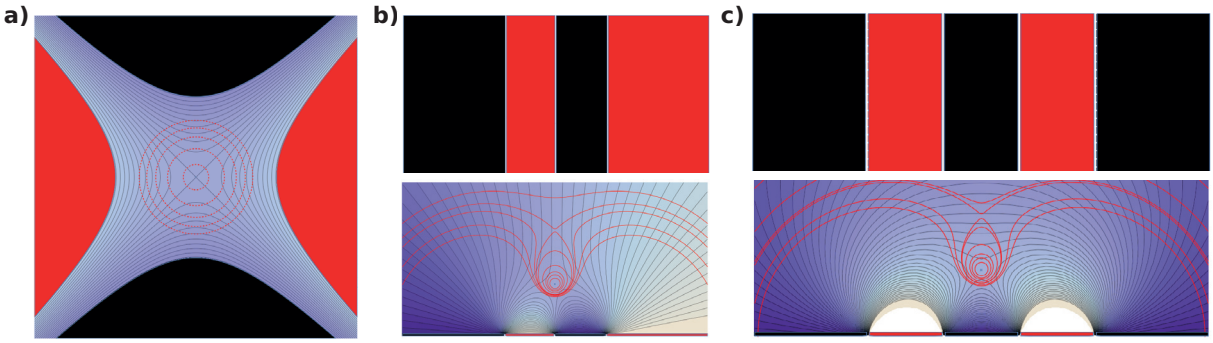

Figure 4.1: Potential contours (blue lines and background shading) and pseudopotential contours (red lines) of a a) three-dimensional RF Paul trap compared to surface electrode traps with b) a "four-wire" design and c) a "five-wire" design. For b) and c), the top panels are top-down views of the RF (red) and ground (black) electrodes, and the bottom panels are side-views.

The basic idea of the three-dimensional linear RF trap and the linear surface electrode trap is the same: the RF provides confinement in two dimensions, creating a one-dimensional, RF-null line along the axis of the trap. The ion is confined axially by DC electrodes. Applying the concept from the 3D geometry to a surface is a kind of reverse Origami. If you imagine "unfolding" the three dimensions of the macroscopic linear Paul trap onto a single plane, then you would recover the geometry of a surface electrode trap. Fig. 4.1 shows two typical designs for the RF electrode geometry of a surface electrode trap: the "four-wire" design (Fig. 4.1b) and the "five-wire" design (Fig. 4.1b). One advantage of the four-wire design is that the antisymmetry of the potentials in transverse direction rotates the radial normal modes of oscillation of the ion to each be at 45° from the trap plane, which makes it possible to cool all three modes of the ion with a laser beam parallel to the surface.

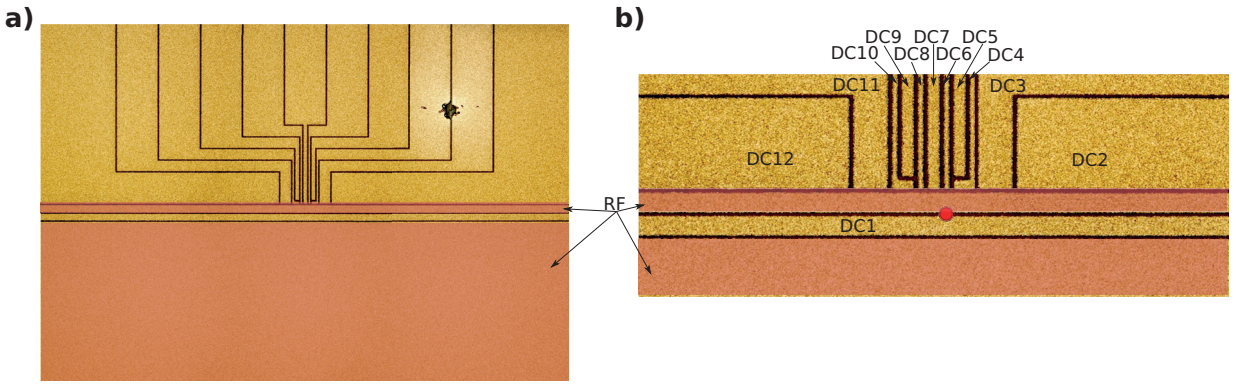

Figure 4.2: Microscope images of "double-well" surface electrode trap, with trapping RF potentials applied to shaded red electrodes and the other electrodes held at RF-ground. a) zoomed out and b) zoomed in to trapping region, where the red circle is where the ion is trapped 40 μm above the surface. DC electrodes DC1-DC12 are labeled.

4.1.1 Double-well trap

The trap used in the experiments presented in this thesis is a four-wire, surface-electrode trap designed by Kenton Brown in ca. 2010 and used in various experiments involving the coupling of two ions in two separate wells [Brown et al., 2011; Wilson et al., 2014]. Figure 4.2 shows microscope images of this trap, with its 8 μm thick gold electrodes electroplated on crystalline quartz and 5 μm-wide gaps between electrodes.

The trap has 12 DC electrodes, which are wire bonded to a "filterboard," which serves two purposes: first, it provides a breakout of the DC lines, allowing connectors to be more easily attached, and second, it contains the 3.5 nF capacitors to ground and 10 kΩ resistors that make up the RC low-pass filters, which reduce the amount of externally injected technical and Johnson noise that the ion experiences.

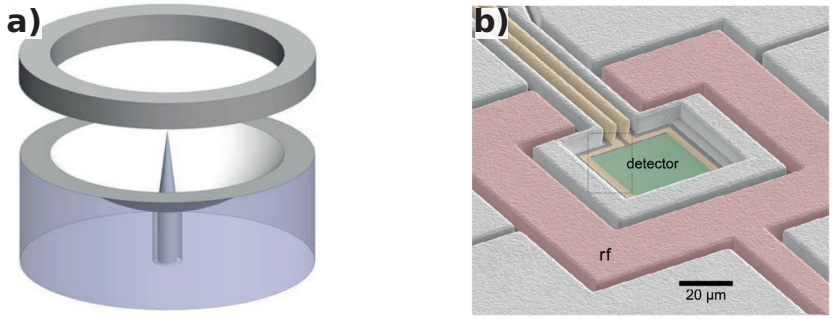

Figure 4.3: a) macroscopic, 3D needle trap, from the University of Washington ion trapping group [Shu et al., 2011]. b) The needle trap geometry unfolded onto a plane: the "detector" trap, a surface electrode trap with 3D RF confinement from Daniel Slichter of the NIST Ion Storage Group [Slichter et al., 2017].

4.1.2 Triangle trap

Up until now, I have only discussed linear RF traps, but there exists another canonical macroscopic trap design that produces a zero-dimensional RF-null point, rather than a one-dimensional RF-null line. One example of this type of trap is shown in Fig. 4.3a). The same concept of "unfolding" the 3D structure onto a 2D plane can be applied to this situation (see Fig. 4.3).

This concept applies to the triangle trap, except that its RF electrode shape was designed so that there are instead three RF null points at the corners of an equilateral triangle 40 μm above the trap surface in which the ions are confined (in fact, there are four RF nulls, but three were intentionally designed) (see Fig. 4.4). Shaping the RF electrode in such a way as to tile many pseudopotential minima in a two-dimensional plane is scalable, and could potentially serve as an alternative to the "quantum CCD" architecture [Mielenz et al., 2016] (see Fig. 4.5). Rather than being transported to different zones as in the quantum CCD idea [Wineland et al., 1998; Kielpinski et al., 2002], this "microtrap array" architecture would forego the transport of ions and allow the coupling between ions to be tuned

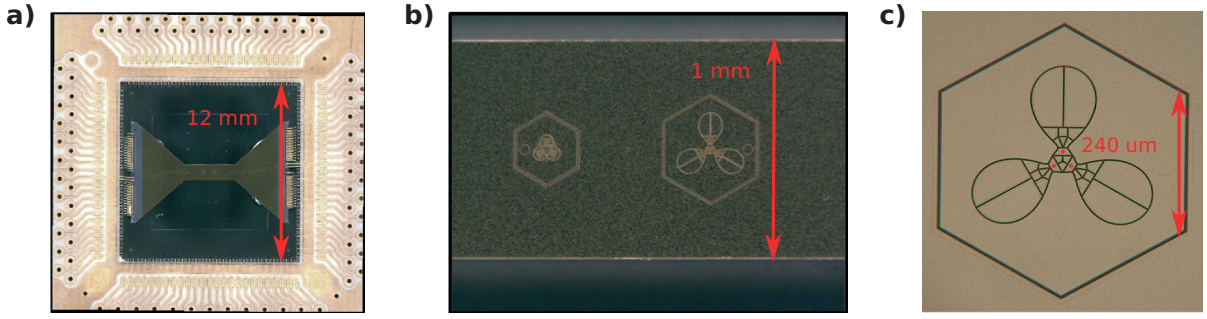

Figure 4.4: Microscope images of the triangle trap. a) Entire chip + interposer, b) zoomed in on both traps, and c) zoomed in on 30 μm triangle, with red dots indicating ion locations.

by changing the relative normal modes of oscillation between sites through the application voltages on of DC electrodes. When ions' oscillation frequencies are very different, they will oscillate independently, but when they are tuned on resonance with one another, the ions' motion can be highly coupled, allowing phonons (quanta of motion) to be exchanged between sites [Brown et al., 2011; Wilson et al., 2014].

The triangle trap we use is a multi-layer trap fabricated by Sandia National Labs (Fig. 4.4). To have full control of the ion's motion at each site, many DC electrodes are needed. Three are needed at each site to cancel any stray fields, and five each are needed to tune the field curvature (hence, the normal modes of oscillation) that the ion experiences. To avoid applying very high voltages to achieve this control, two more electrodes are added to make the problem underconstrained. There are two triangle traps on each chip, so this means that we need at least 60 electrodes on a single chip, with some of the electrodes being as small as ~ 5 μm^2. This requires more than 100 classified fabrication steps to create the elaborate electrode geometries (see Fig. 4.4) and complicated array of vias through the various layers to connect each electrode to the bond pads on the edges of the trap chip (Fig. 4.4). The two traps on the chip are both triangles, one with 30 μm distances between trapping sites and one with 20 μm distances. The trap chip is diced into bow-tie-like shape to minimize

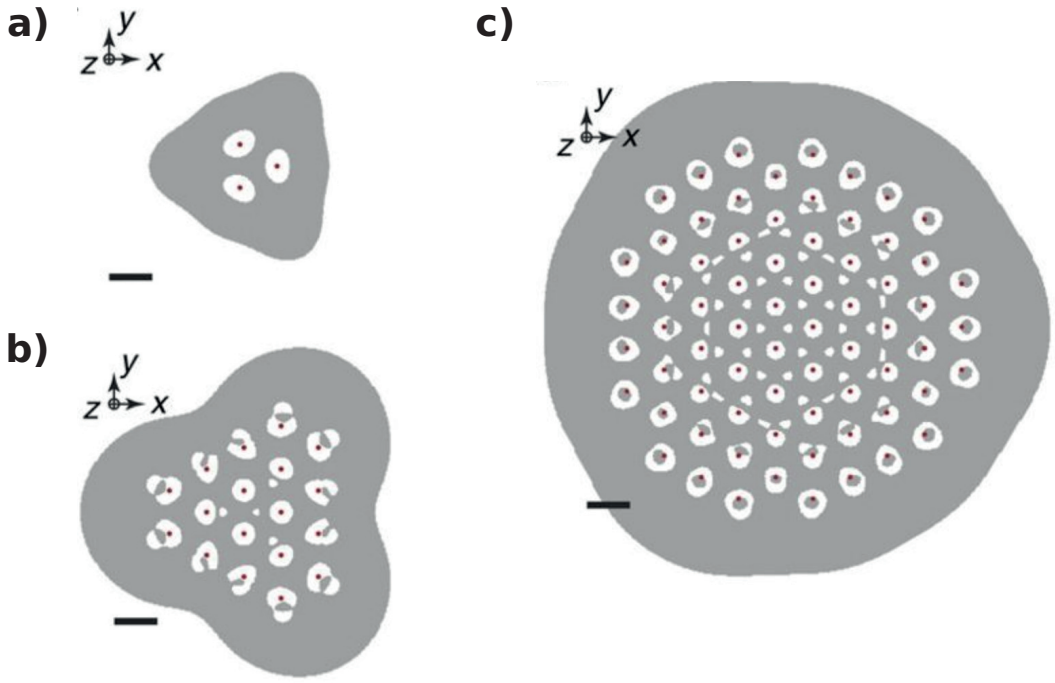

Figure 4.5: Scaled-up 2d-array traps. Conceptual design of how to scale to larger microtrap arrays. Designs for the rf electrode shape (gray region) for traps with a) 3 sites, b) 18 sites, and c) 69 sites, where each site is denoted by a red dot. Figure from [Mielenz et al., 2016].

scatter of the laser beams off of the trap surface.

The trap chip is bonded onto a silicon interposer, also fabricated at Sandia, which has integrated 1.5 nF trench capacitors to ground on each DC line to low-pass filter the DC lines. This eliminates the need to put capacitors on the filterboard as was done previously for the double-well trap, but the relatively low break-down voltage of the trench capacitors of 20 V limits the range of applicable potentials.

4.2 Laser system, microwaves, and resonant electric field excitation of motion

In order to load, cool, and control the quantum state of beryllium ions, we need lasers for photoionization, Doppler cooling, Raman transitions, and repumping (see Fig. 4.6). In addition, we use microwaves applied to electrode DC1 of the trap depicted in Fig. 4.2. With the exception of the photoionization laser, the lasers we use are all produced with the same basic scheme: two near-infrared lasers at approximately 1050 nm and 1550 nm are summed (sum-frequency generation, or SFG) together in a single-pass periodically poled lithium niobate (PPLN) non-linear crystal to produce red light at approximately 626 nm, then this light is frequency doubled (second-harmonic generation, or SHG) in a resonant bow-tie cavity with a Brewster's angle-cut β-barium borate (BBO) crystal centered at the tighter of the two cavity mode waists (approximately 200 μm and 20 μm) [Wilson et al., 2011]. The resulting 313 nm light is passed through various AOMs to achieve the desired frequency and ability to switch beams on and off, then fiber-coupled into a hydrogen-loaded and cured solid-core, photonic crystal fiber [Colombe et al., 2014]. Following the output of the fiber, the beams are collimated and the polarization suitably rotated, then each beam is focused with a 15 cm focal length lens into the UHV chamber at the trapping site of the ion.

In the next few subsections, I will describe the beam paths of the lasers, then discuss certain aspects of the setup in more detail. The SFG and SHG are covered in detail in [Wilson et al., 2011].

4.2.1 Doppler cooling and detection laser

The Blue Doppler (BD) beam can be tuned to resonance for detection or be red-detuned by 10 MHz for Doppler cooling, and is set to approximately half the saturation intensity (~ 0.1 W/cm^2, see Fig. 4.7). The Blue Doppler Detuned (BDD) is generated from the same source, but red-detuned by approximately 500 MHz so that it provides far-detuned cooling light for highly energetic ions (for example when the ion is first loaded into the trap) and repumping from other ground state hyperfine levels, including those in the $F = 1$ manifold. To this end, the BDD is detuned such that it is roughly halfway between the F=2 and F=1 manifolds to $^2P_{3/2}$ transitions and its intensity on the ions is set to approximately 10 times the saturation intensity.

To produce the BD/BDD light, we start with an NKT Photonics erbium-doped fiber laser that is sent through a fiber amplifier to produce 3 W of 1549.408 nm light. This light is combined with 2 W of light from a Koheras Boostik ytterbium-doped fiber seed laser + amplifier at 1051.132 nm. This laser produces 6 W in total but is split between the BD, RD, and Raman beamlines. After summing to 626.267 nm light, some of the light is picked off by a waveplate + polarizing beamsplitter and sent through a -290 MHz, double-pass offset AOM, then delivered to the iodine lock setup with a short optical fiber. See Fig. 4.8 for a schematic. In the iodine lock, we use Doppler-free saturated absorption spectroscopy with pump and probe beams counter-propagating in a 10 cm long iodine cell to resolve the individual hyperfine lines of the iodine molecules. We modulate the frequency of the 90 MHz

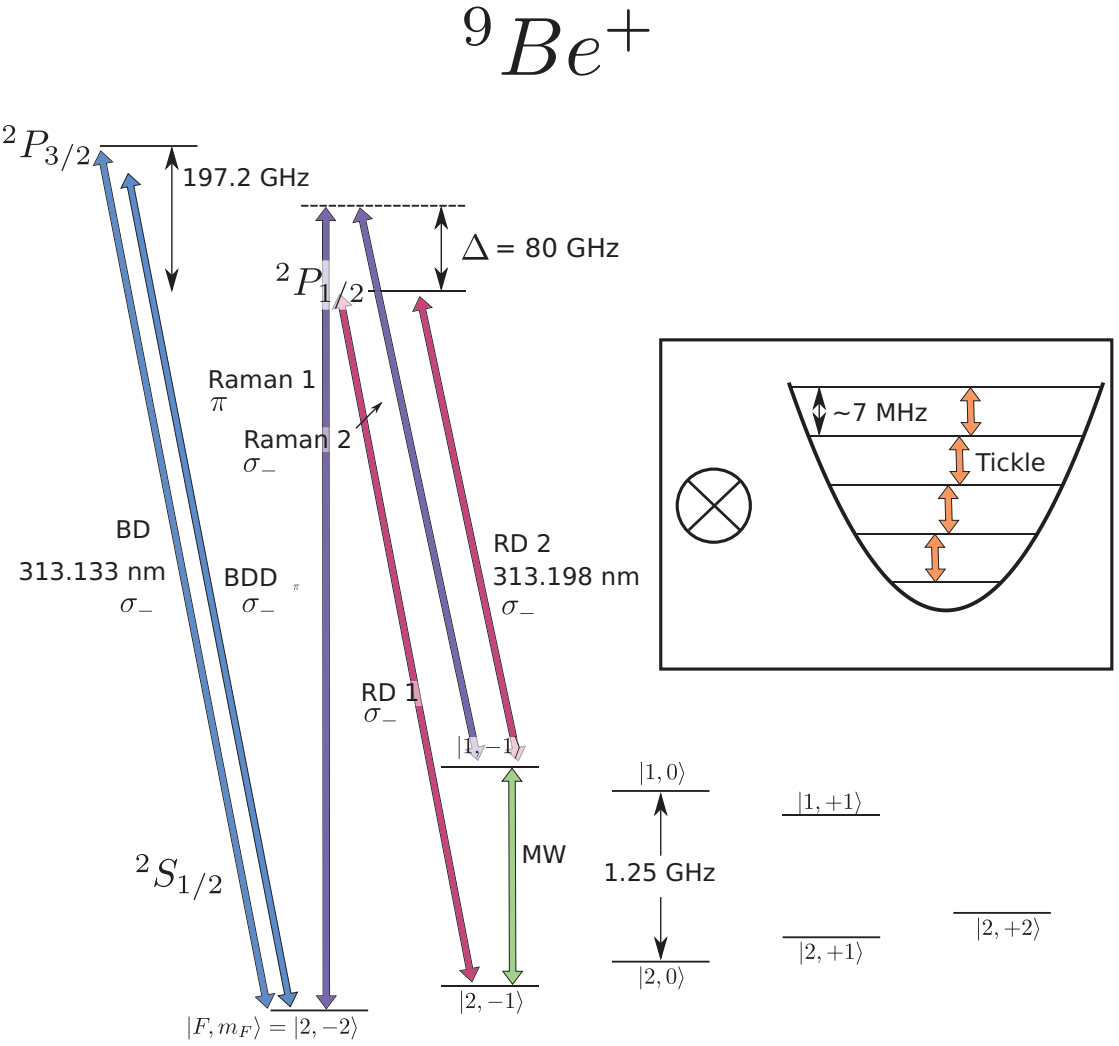

Figure 4.6: Beryllium energy levels, with laser beams and microwaves represented as colored arrows. The Blue Doppler Detuned (BDD) beam (blue arrow labeled "BDD") is used for a first stage of Doppler cooling, and the Blue Doppler (BD) beam (blue arrow labeled "BD") is used for Doppler cooling and fluorescence detection. The two Raman beams (purple arrows labeled "Raman 1" and "Raman 2") are used for resolved sideband cooling to the ground state and motional state preparation. The two Red Doppler (RD) beams (red arrows labeled "RD 1" and "RD 2") are used as repumps in case of a scattering event leaving the state in a different hyperfine state than $|2,-2\rangle$. Microwaves (green arrow labeled "MW") are delivered to the trap by running a current through a DC electrode. The microwave frequency can be set to transfer populations between any two states with $\Delta m = 0, \pm 1$ in the ground state hyperfine manifold. Finally, the electric field tickle tone (labeled "Tickle") is set to the the harmonic oscillator frequency, which coherently excites motion in the ion.

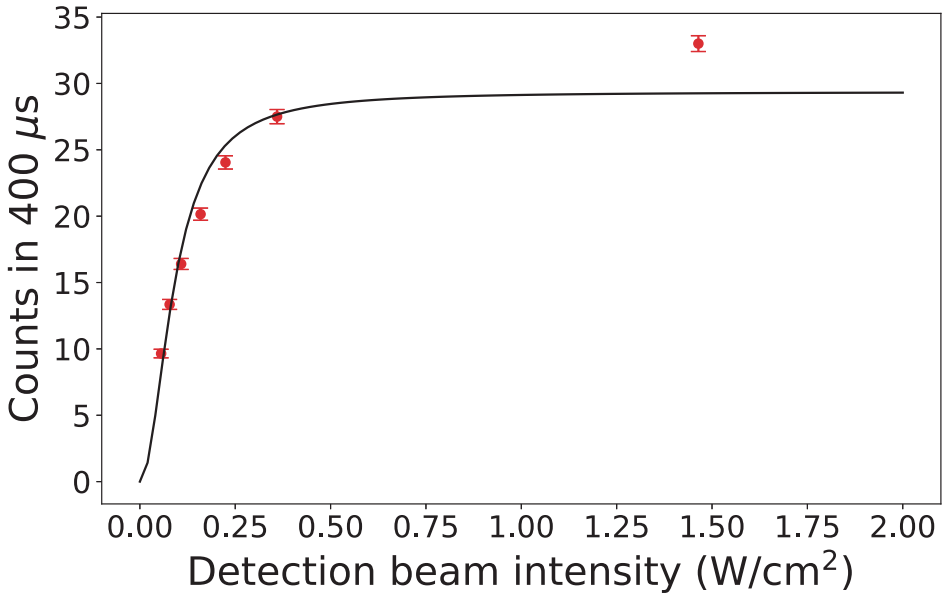

Figure 4.7: Saturation measurement of ion $^2S_{1/2}\,|2,-2\rangle \leftrightarrow\ ^2P_{3/2}\,|3,-3\rangle$ cycling transition versus intensity of detection beam. Red points are data and black line is a fit to the data. The power is measured at each point and intensity is calculated based on an estimated 20 μm beam waist at the location of the ion. Based on this measurement, we choose to set our detection beam intensity to $\sim$0.1 W/cm^2, corresponding to $\sim$15 counts when the ion is bright.

pump AOM to be able to detect the saturation signal (determined by measurement of the power of the probe beam by a photodiode) with a lock-in amplifier.

The red light is then doubled in a bow-tie cavity, followed by a 220 MHz noise-eater AOM which stabilizes the power of the beam by monitoring the photodiode signal from a small amount of the beam which is picked off by a glass plate and feeding back to noise eater AOM drive. The beam power after the noise eater is held constant by dumping a variable amount of power (roughly 5-10%) into the first order diffracted beam of the noise eater AOM (see Fig. 4.8). A 50/50 beamsplitter splits the BD and BDD light, which are double-passed through +220 MHz and -80 MHz AOMs, respectively. The same beamsplitter recombines the beams, which are then fiber-coupled into a 0.5 m long UV fiber to be focused on the ion.

4.2.2 Repump laser

The Red Doppler (RD) beam line contains two different frequencies: one is resonant with the $|\uparrow\rangle \leftrightarrow {}^2\mathrm{P}_{1/2}$ transition, and the other is resonant with the ${}^2\mathrm{S}_{1/2}|2,-1\rangle \leftrightarrow {}^2\mathrm{P}_{1/2}$ transition. These are used to repump the ion when it scatters into an undesired ground state hyperfine level and after transitions to hyperfine states other than $|2,-2\rangle$ during sideband cooling and other internal state manipulation.

The 626.385 nm red light of the RD is produced from summing an NP photonics "The Rock" fiber laser + amplifier, which produces 3 W of 1550.192 nm light, and 2 W of the shared 1050 nm laser. Some of the light is then picked off by a waveplate + polarizing beamsplitter and sent through a -204 MHz offset AOM, then delivered to the iodine lock (Fig. 4.9).

Following the doubling and noise-eater stage which is set up similar to the BD (see above),

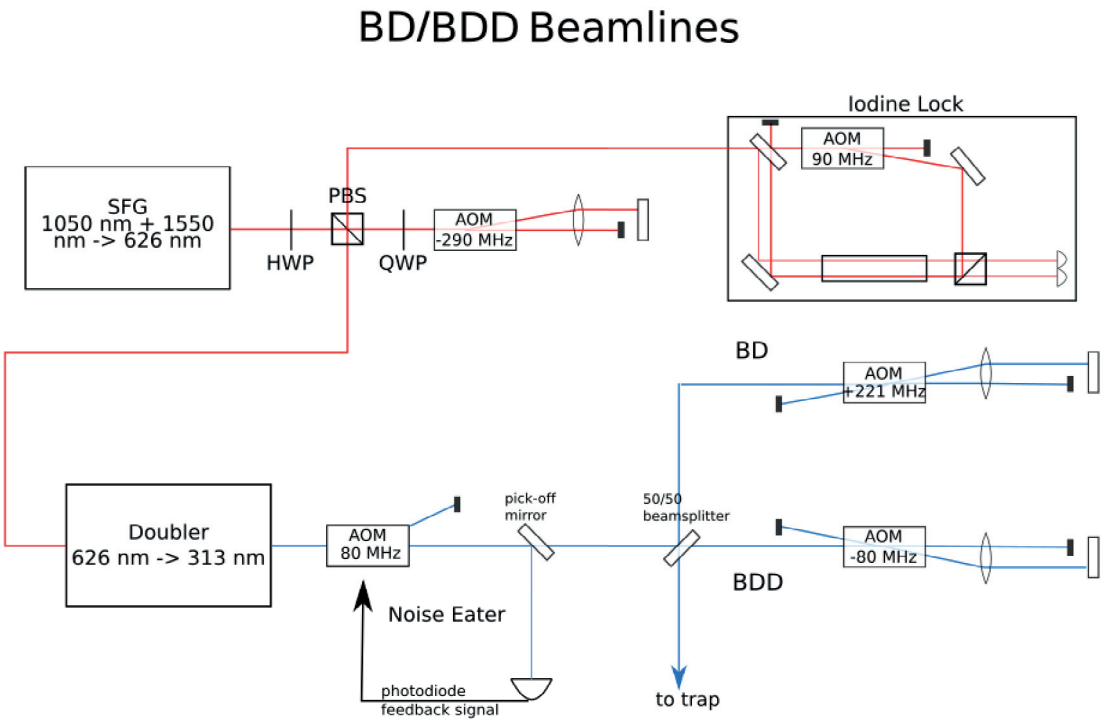

Figure 4.8: Blue Doppler beamline. Two NIR fiber lasers at approximately 1050 nm and 1550 nm are summed to generate 626 nm light, then doubled to produce 313 nm light. The beam is split into BD and BDD beamlines and double-passed through separate AOMs at +221 MHz and -80 MHz, respectively, then recombined and delivered through a fiber to the trap.

the light is split by a 50/50 beamsplitter, where one half is double-passed through a +221 MHz AOM and the other is double-passed through a -415 MHz AOM. They are recombined on the same 50/50 beam splitter, combined with the BD on a subsequent 50/50 beamsplitter, and delivered through the UV fiber to the trap along with the BD. See Fig. 4.9 for a schematic.

4.2.3 Raman laser

The two Raman beams are detuned by approximately + 80 GHz from the $^2S_{1/2} \leftrightarrow {}^2P_{1/2}$ transition and by approximately 1.3 GHz from each other to induce transitions between the $|2,-2\rangle = |\downarrow\rangle$ and $|1,-1\rangle = |\uparrow\rangle$ hyperfine levels of the ground state $^2S_{1/2}$. We also need to set the polarization of the beams so that angular momentum is conserved. One of our beams is π-polarized and the other is $\sigma_+ + \sigma_-$ polarized. Only the σ_- photons drive transitions, but it turns out that using both σ_+ and σ_- with roughly equal intensity largely cancels the AC Stark shifts difference of the levels participating in the transition from the off-resonant coupling to the upper P-levels (see Sec. 3.4).

The 626 nm red light is produced from summing 3 W of an NKT fiber laser and amplifier at 1550.032 nm with 2 W of the shared 1050 nm light with a PPLN crystal in the same way as for the BD and RD. Since fluctuations of the detuning from the $^2P_{1/2}$ level only changes the Raman Rabi frequency to second order, the absolute detuning is not so critical, so we don't lock the wavelength to an iodine feature like we do for the BD and RD.

After the 626 nm light is doubled to 313 nm and split into two beams, the relative phase stability between the two beams is very important. Because of this, we want to eliminate any path-length differences that vary in time. This would chiefly be caused by vibrating mirrors

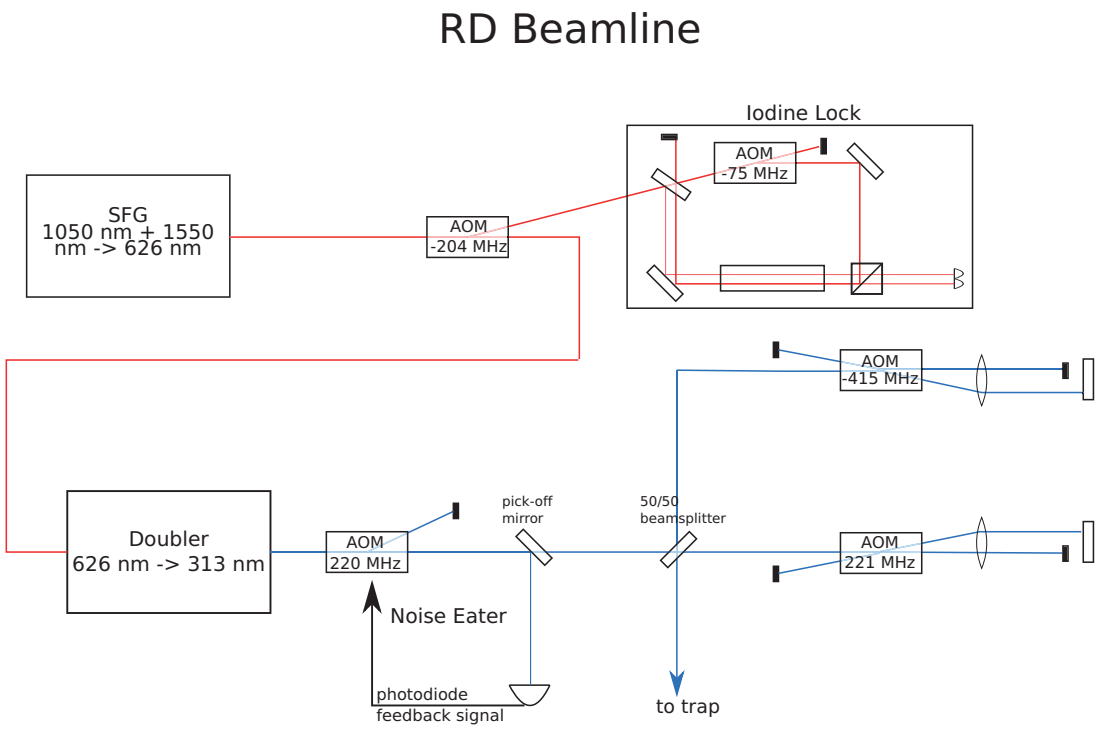

Figure 4.9: Red Doppler beamline. Two NIR fiber lasers at approximately 1050 nm and 1550 nm are summed to generate 626 nm light, then doubled to produce 313 nm light. The beam is split into RD1 and RD2 beamlines and double-passed through separate AOMs at +221 MHz and -415 MHz, respectively, then recombined and delivered through a fiber to the trap.

or other optics and air currents in the beam path. To mitigate these effects, we periscope the beam height from the typical 4-inch height down to 2 inches, so that we can use shorter posts with reduced mechanical vibration. The beam passes through a half-waveplate and a Glan laser prism to split the light into beams R1 and R2, rather than the 50/50 beam splitter used for the BD and RD, which only allows a maximum of 25% of the light to be delivered to the trap following the recombination (however, the remaining beams can be sent to another trap setup in the same laboratory). The R1 (R2) beam is then double-passed through a +320 (-320) MHz AOM, tunable over approximately ±30 MHz, with RF derived from the same source, for a total frequency difference between the two beams of $320 \times 4 = 1.28$ GHz. The beams are then recombined on the Glan laser prism, and coupled into a UV fiber to be delivered to the trap. In order to be able to have the maximum amount of light available to deliver to the trap, we spatially separate the incoming and outgoing beams in the double passes by a corner cube retro-reflector. This vertically offsets the outgoing beam, which we can then pick off with a d-shaped mirror after the two beams are recombined in the Glan laser prism. The entire double-pass setup is boxed up to eliminate air currents as much as possible. See Figs. 4.10 and 4.11 for a diagram and a picture, respectively, of the setup.

4.2.4 Frequency doubling cavity with BBO

As mentioned, much of the detail about the SHG cavities for producing the 313 nm light is covered in [Wilson et al., 2011], but we have learned of some quirks connected with using BBO crystals at relatively high powers and relatively short wavelength that we note here. First, since BBO is hygroscopic, it is necessary to gently purge the crystal with dry oxygen. Keeping the crystal mount housing at a slightly positive pressure also helps mitigate the optical tweezer effect, where dust particles are tweezed to the the part of the beam with the highest intensity. The beam waist is inside the crystal, so the dust particles get

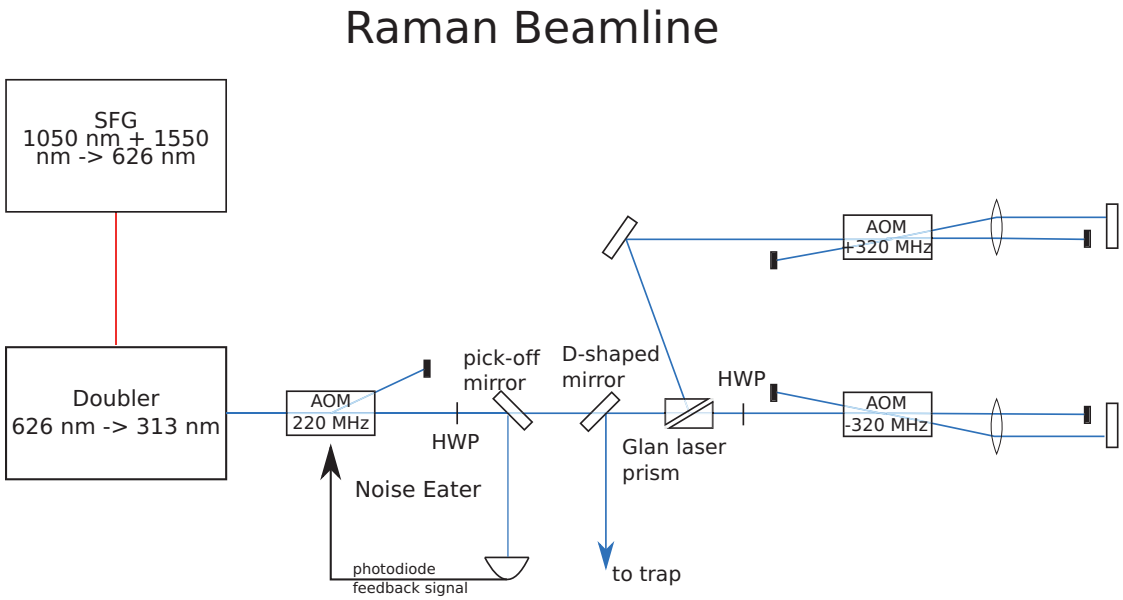

Figure 4.10: Raman beamline. Two NIR fiber lasers at approximately 1050 nm and 1550 nm are summed to generate 626 nm light, then doubled to produce 313 nm light. The beam is split into two beamlines and double-passed through separate AOMs at ±320 MHz whose frequency is controlled by the same DDS, then recombined and delivered through a fiber.

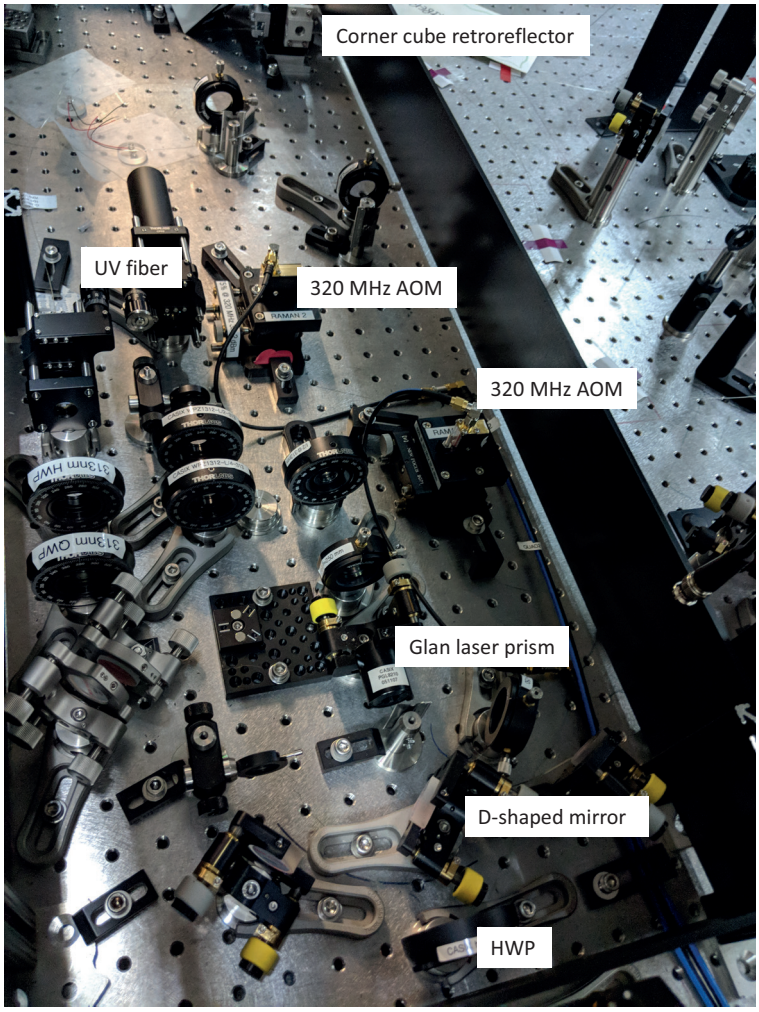

Figure 4.11: Photo of Raman double-pass AOM setup. The lid of the box protecting against air currents was removed to take this picture.

deposited on the surface of the crystal and sometimes are burned on, damaging the crystal. We suspect that oil in the oxygen line and the decomposition of certain types of tubing used to deliver the oxygen have contributed to additional surface contamination and damage of some of our crystals, so it is worth putting reasonable thought and care into this aspect of the doubler. We have an oil filter right after the oxygen cylinder regulator, and have replaced the problematic tubing with one that does not decompose to the same extent.

4.2.5 Spatial filtering of Raman beams

Because the Raman beams deliver relatively high power ($\sim$ 500 μW) in a beam waist of approximately 15 μm at the position of the ion and the ion is only 40 μm away from the trap surface, a non-negligible amount of the Raman light in the wings of the beam can scatter off of the electrode surfaces. This seems to contribute significantly to trap charging and the ion motional decoherence, so we try to minimize this scatter as much as possible. Following the output of the fiber, we send the two Raman beams through a spatial filter, where we focus them through a 25 μm diameter pinhole, cutting off approximately 20% of the light. The beam is then recollimated with a 15 cm lens. Fig. 4.12 shows the effect of the spatial filtering on the focused beam shape of the ion. Note that the side lobes are eliminated and the beam looks much closer to the ideal Gaussian profile after the filtering.

4.2.6 Photoionization laser

Beryllium is ionized with two photons at 235 nm—the first photon excites one of the valence electrons to a the first excited P-state in neutral beryllium, and the second excites the electron to the continuum, ionizing the atom. The photoionization light that we use

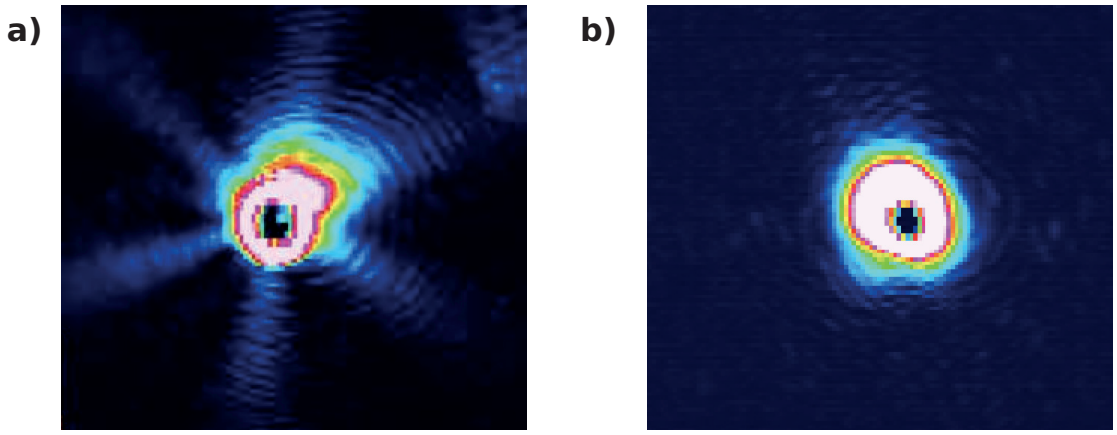

Figure 4.12: Raman beam shape a) before and b) after spatial filtering. Note that camera exposure time is set so that the center of the beam is significantly oversaturated so that we can see the weaker outer part of the beam.

is produced from a Coherent Verdi laser that pumps an M-squared CW Ti:Sapph at 940 nm, which is then doubled twice. The first doubling stage to 470 nm is achieved with a commercial M-squared doubler and the second doubling stage to 235 nm is a bow-tie cavity with BBO, adapted from the design of the 626 nm to 313 nm doublers. The 235 nm ionization light is then sent through a short (20 cm) piece of UV fiber to be spatially filtered and delivered to the trap.

4.2.7 Microwave drive

Two hyperfine sublevels can be connected via the resonant magnetic field from produced from a microwave current applied to DC electrode 1 on the trap (see Fig. 4.2). The tone is derived from a DDS with a 1 GHz clock. To avoid aliasing, we low-pass the output, limiting the frequency of the DDS signals to less than 500 MHz. To reach the desired frequency range of 1.22-1.28 GHz to connect the Zeeman sublevels between the ground hyperfine states, we use Minicircuits components to frequency quadrupole and further filter this DDS tone. After the quadrupling stage, the tone is connected to the high-pass port of a triplexer which is capacitively coupled to DC1 by a 3.5 nF capacitor (see Fig. 4.13).

4.2.8 Excitation of motion with resonant electric fields

Near-resonant excitation of ion motion with a "tickle" is a very useful technique to find the secular frequencies of the ion without needing Raman sideband transitions. This is especially useful when first testing a new trap or a trap under new conditions. We apply an oscillating voltage to a trap electrode which generates a time-dependent field at the location

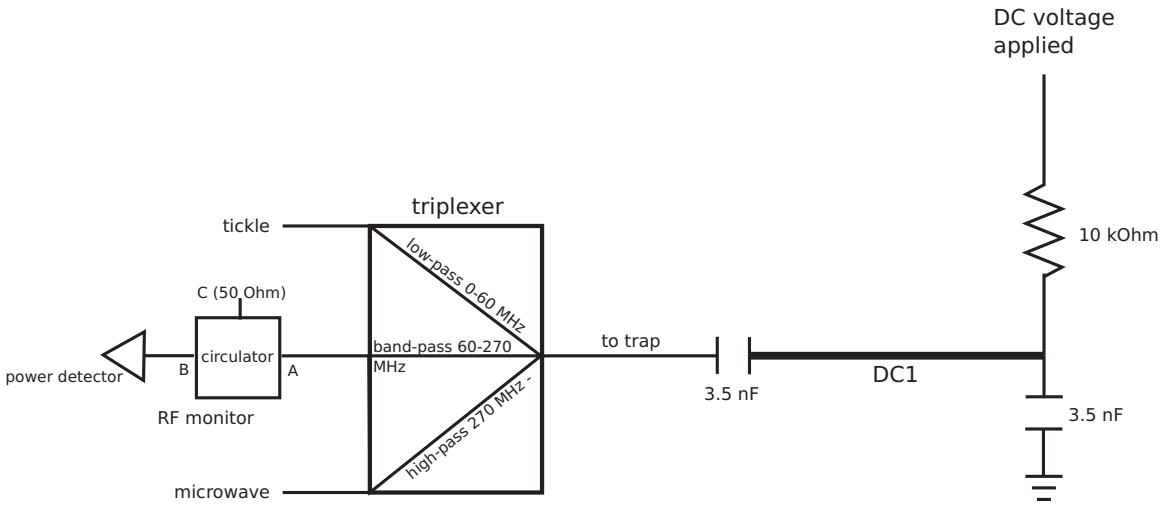

Figure 4.13: Schematic of electrical configuration for microwave, tickle, and RF monitor connections. The three are connected through a triplexer with high-pass (270 MHz -), low-pass (0 - 60 MHz), and band-pass (60 - 270 MHz) ports, which are sent to DC1 of the double-well trap through a 3.5 nF capacitor. The DC voltages are applied to the electrode from the top-right in the schematic, through a low-pass filter composed of a 10 kΩ resistor and a 3.5 nF capacitor to ground.

of the ion, $\vec{E}(t) = \vec{E}_0 \cos(\omega_{tic} t)$, that creates a driving force:

$$\vec{F} = q\vec{E}_0 \cos(\omega_{tic} t) \tag{4.1}$$

on the ion. If ω_{tic} is resonant with one of the secular frequencies of the ion and $\vec{E}_0$ has a component along the mode direction, this acts as a driven harmonic oscillator, exciting motion in the ion, which we then detect by observing a change in the fluorescence level. For higher precision, we can detect the departure of the ion from the ground state, as will be discussed in Ch. 7.

The resonant electric field is produced from a DDS at 1-20 MHz frequency, corresponding to the ion oscillation mode frequencies, and connected to the low-pass port of a triplexer which is capacitively coupled to DC1 in the double well trap by the 3.5 nF capacitor (see Fig. 4.13).

4.3 UHV copper vacuum enclosure

The experiments were performed in a copper UHV vacuum enclosure (the "pillbox") that was designed and assembled by Kenton Brown. While it was successful in housing a trap that produced many results (e.g., [Brown et al., 2011; Wilson et al., 2014]), it was not ideal for quickly switching between traps or for traps with a large number of DC electrodes. Following the lead of Daniel Slichter in the "cryo 2" experiment (another cryogenic ion trap apparatus in our lab), I also designed a new pillbox for our setup, nicknamed "cryo 1." Nearly all of the trap and oven mounting parts are identical to the cryo 2 pillbox, which should allow us to not only easily switch between traps in cryo 1, but also swap traps between cryo 1 and cryo 2. A side-by-side comparison between the old and new pillboxes is shown in Fig. 4.14. The new base plate is made of copper for good thermal conductivity

from the cryostat cold plate to the trap, but has a stainless steel ring brazed into the copper in which all of the electrical feedthroughs are welded (see Fig. 4.14b). There is also a 3/8 inch stainless steel tube welded into the ring with an L-shaped Swagelock connector on the end. In the other side of the connector, we can insert a 3/8 inch copper tube through which we pump out the pillbox, then subsequently pinch off the copper tube to create a vacuum tight seal. The lid is secured to the baseplate with an indium wire seal and has 9 viewports, 8 for laser access and one on the top of the lid for imaging, which are also sealed with indium.

Following the design and machining of the individual parts, postdoc Jonas Keller has taken over the assembly and testing of the new pillbox. He has been able to achieve 10^{-7} Torr base pressure at room temperature (without baking), with no detectable leaks, an improvement over the aging older pillbox. Installation of a re-designed triangle trap (see Ch. 8) into this new system is imminent.

4.4 Cryostat

The UHV pillbox is mounted to the cold head of a $\sim$ 1 m tall bath cryostat, which holds approximately 40 L each of liquid helium and liquid nitrogen, with both spaces isolated from each other and the surrounding room-temperature air by a 10^{-6} Torr vacuum space. Because of the need to thermally isolate the coldhead from the environment, all of the dewar spaces are attached at the top of the cryostat, constituting a 1 meter-long pendulum. Any vibrations of the cryostat will cause the trap, and hence the ion, to move relative to the laser beams. The most detrimental effect of this will be errors in the Raman beam operations from unstable optical phases and Rabi frequencies. To mitigate this as much as possible, we have added kevlar braided straps that wrap around the bottom of the coldhead in-vacuum to reduce pendulum vibrations. This provides the mechanical support needed with minimal

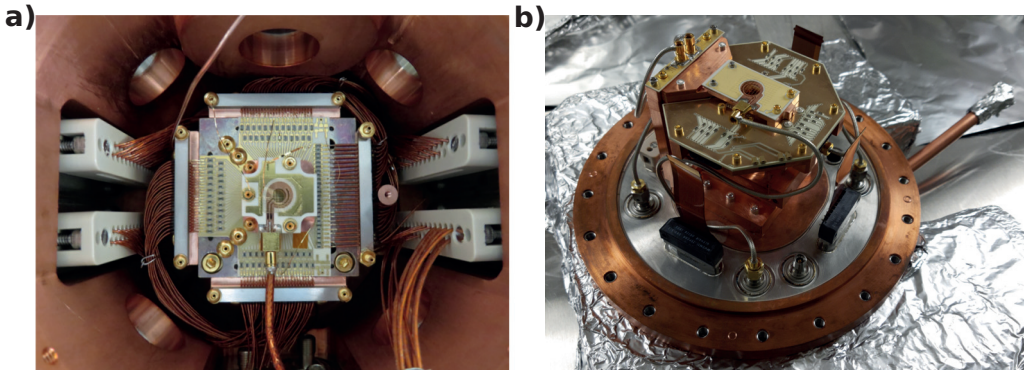

Figure 4.14: A comparison of the old and new pillboxes: a) The old pillbox. Note the handwiring of ∼100 connections, and the walls on all sides, which made taking traps in and out tricky and risky. b) The new pillbox. Commercial connectors and made-to-order flex PCB are used to break out DC wiring, and all components are mounted to and plugged in on the baseplate, allowing more maneuverability in assembly. Electrical feedthroughs and pump-out tube are welded into the stainless steel ring, which is brazed into the copper.

thermal conductivity between the 4 K space and room temperature. We also use four 2-inch diameter posts attached to the bottom of the outside of the cryostat to rigidly register the bottom of the cryostat to the optical table.

4.5 Imaging system

The imaging system used in experiments described in this thesis is an in-vacuum Schwarzschild objective, designed by previous postdoc Christian Ospelkaus, made of two mirrors optically contacted to two glass pillars and crossbar. It has fairly high magnification (adjustable between 40 and 50) with low aberrations, imaging both 313 nm and 235 nm light with the same focal distance. However, it also has a very small depth of field, which means that we have to be able to move it relative to the object we want to image in vacuum. We achieve this by using an Attocube actuator, which uses a stack of piezo-electric transducers that slip-stick against another piece, moving like an inchworm for a total travel of approximately 5 mm. This usually worked well, but after having the Attocube sieze in vacuum at 4 K repeatedly, we decided to design a new imaging system that did not have any moving parts in-vacuum.

In fact, the new imaging system is completely outside the vacuum enclosure. It uses two $f = 60$ mm, aspheric lenses made by Aspheric on as a one-to-one relay to produce a primary image approximately 180 mm from the object plane. A Thorlabs high-NA 40x microscope objective then produces a secondary image either on the Andor CCD camera or the Hamamatsu PMT (a flipper mirror that can be moved into the beam paths allows us to choose between the two).

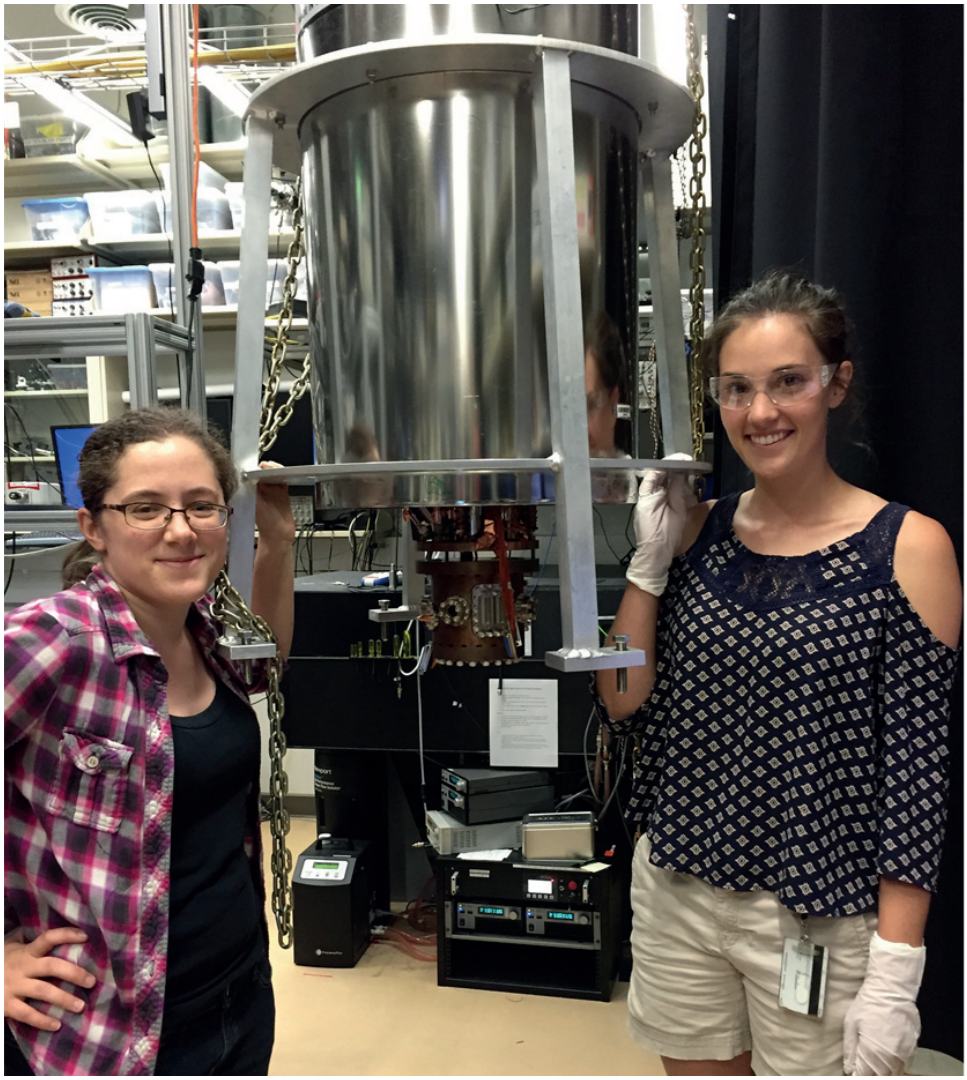

Figure 4.15: Photograph of bath cryostat, with copper pillbox attached (outer vacuum can removed). Susanna Todaro (left) and I (right) are pictured for scale. We are normal-height humans.

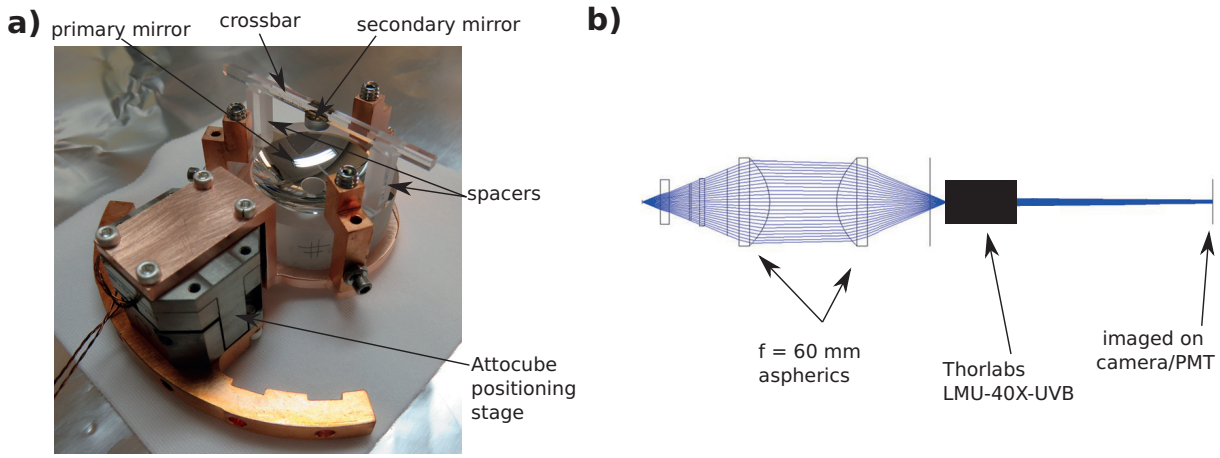

Figure 4.16: a) Photograph of Schwarzschild objective, designed by Christian Ospelkaus. The two mirrors are connected to each other through optically contacted glass spacers that need to be matched very precisely (order a few μm) in height to produce aberration-free images. The secondary mirror is held by a cross bar that requires similar tolerances as the spacers.) This is mounted onto the Attocube positioning stage. b) Ray diagram of the new, out-of-vacuum imaging system, which has replaced the Schwarzschild objective. Two f =60-mm aspheric lenses (Asphericon AFL50-60-S-X) produce an unmagnified primary image, which then is magnified by a 40x microscope objective from Thorlabs (LMU-40X-UVB).

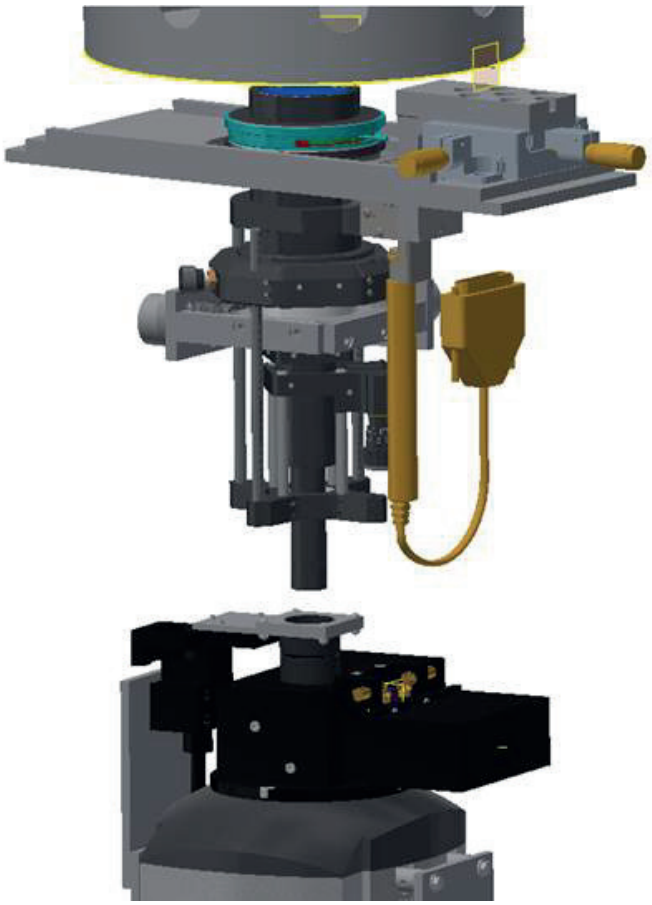

Figure 4.17: Inventor drawing of new imaging system and mounting configuration, designed by Jonas Keller.

4.6 Radio-frequency trap drive

The ions are confined by a pseudopotential created from an RF electric field oscillating at approximately 125 MHz. Because the amplitude of the RF that is applied to the trap in part determines the confinement of the ion, any amplitude noise can translate into ion mode-frequency noise, which can cause motional decoherence. So it is very important to have a stable RF source. To get a low-amplitude noise RF signal at the trap, we start with a Holzworth low phase noise synthesizer as our clock, which triggers an amplitude-stable RF source (developed by David Lucas' group at Oxford and David Allcock) that generates a square wave supplied by a very stable 5 V DC voltage source. After band-pass filtering which eliminates the higher harmonics of the square wave, we are left with a phase- and amplitude-stable sinusoidal RF signal.

Another place where care must be taken to avoid amplitude noise is in the RF resonator. This can introduce amplitude noise in two ways. First, if the quality factor of the resonator is so high that some of the input frequency excursions lie on the slope of the resonator transmission profile, then the source frequency noise gets translated into amplitude noise. For this reason, we use a resonator with a modest quality-factor of ~ 100, which, at 125 MHz RF frequency, corresonds to 1.25 MHz bandwidth, which is much larger than the RF frequency noise. Second, if mechanical vibrations cause the resonator to change its shape, hence changing its capacitive coupling, this can also affect the amplitude stability. We have addressed this by replacing our previous resonator consisting of a spring-like wound cylindrical coil, which was very susceptible to mechanical vibrations, with an inductive resonator on a printed circuit board (designed by Daniel Slichter).

We have the ability to monitor the power of the RF signal on the trap by measuring the pickup on a nearby DC electrode, DC1 (see Fig. 4.2). This DC is connected to the triplexer,

so we monitor the signal using the third and final port of the triplexer, which is band-passed from 60 MHz to 270 MHz, followed by a circulator and diode-based power detector (see Fig. 4.13).

4.7 Magnetic field coils

The quantization axis is defined by a 14.3 Gauss field at 45° from the axial direction of the trap in a plane parallel to the trap electrode surface. The field is produced with water-cooled coils in a Helmholtz configuration, with 9.69 A of current produced from an HP 6628A DC power supply. The power supply has relatively low noise, and with this setup we passively achieve 10^{-4} relative magnetic field stability. Although was not used in the experiments presented here, we also have the option of stabilizing the current. Since we are only stabilizing the current and not the field at the location of the ion, if the coils are not rigidly mounted or there are other fluctuating magnetic fields not derived from the bias field coils, we will not necessarily be able to keep the field at the ion stable to the level that is given by the current stability.

4.8 Experimental Primitives

I will briefly describe, in roughly chronological order, a few experimental procedures that we perform in either preparation of or as steps for detection of the experiments described in later chapters. These involve loading the ion, controlling and measuring the motion of the ion, and state detection primitives.

4.8.1 Loading ions into a trap

We load beryllium with a resistive "oven," which consists of 50 μm diameter beryllium wire wrapped around 100 μm diameter tungsten wire. The tungsten wire itself is then wound into a spiral of roughly 2 mm diameter. We run a current (usually $\sim$ 1.2 A) through the oven, which heats the beryllium to approximately 1300 °C, sublimating the metal and creating a flux of neutral beryllium atoms passing through the trapping region with an average velocity of 1700 m/s. While the oven emits atoms, we also apply our photoionization (PI) beam and Doppler cooling (BD/BDD) beams focused on the trapping region. If a neutral beryllium atom passes through this region, the PI can ionize the atom through a two-photon process, with one photon bringing the atom from the ^{1}S ground state to the ^{1}P$_0$ first excited state, and a second photon exciting the electron to the continuum. Generally, the potential depth in surface electrode traps are around 20-30 meV, so we expect that we are only trapping a velocity class at the lower-end tail of the velocity distribution. This question, among other questions relating to ion production and loading efficiency, is the subject of study of Hannah Knaack's current project.

4.8.2 Doppler and ground state cooling

We first Doppler cool the ion, using the BD and BDD beams. The BDD serves two purposes: it is responsible for initially cooling the ion when it is first loaded and very hot. Second, it acts as a repumper if the ion scatters into the wrong hyperfine sublevel, making the BD now blue-detuned. The BD is detuned by $-\Gamma/2 \approx$ -10 MHz from the $^2\mathrm{S}_{1/2}\,|2,-2\rangle \leftrightarrow\ ^2\mathrm{P}_{3/2}\,|3,-3\rangle$ cycling transition and cools the ion to near the Doppler temperature of $\sim$1 mK.

Following the Doppler cooling stage, in most experiments, we ground state cool using pulsed Raman sideband transitions interspersed with repumping pulses from the RD. Using the predicted $\bar{n}$ based on our Doppler temperature and mode frequency, we apply a certain number of red sideband pulses (usually 10-20 on the axial mode and 5-10 on the radial modes, since they are higher frequency so have lower $\bar{n}$), with each sideband pulse followed by an RD pulse to repump to the $|2,-2\rangle$ state. After this, we typically achieve $\bar{n} \approx 0.05$ on the axial mode and $\bar{n} \approx 0.01$ on the radial modes. Sometimes, since the initial occupations in the radial modes are already so low after Doppler cooling, we do not need to sideband cool them. The trade-off is between suffering more charging of the trap surface due to the increased number of Raman pulses for sideband cooling and having slightly smaller Debye-Waller factors [Wineland et al., 1998] due to the increased occupation in the radial modes.

4.8.3 Micromotion compensation

In order to have an ion whose radial motion is well described by a harmonic oscillator at the secular frequency and that scatters near-resonant photons at the optimal rate, we must compensate stray electric fields at the position of the ion. We apply voltages on various DC electrodes to create an electric field that is equal and opposite to the stray field at the postion of the ion, so that the position of zero static field overlaps with a position where the RF field is minimal and micromotion is negligible. We use a few different techniques to accomplish this.

First, to find the correct position perpendicular to the electrode plane, we scan the voltage applied to the "mesh," which is an electrically floating gold screen parallel to and ~ 2 mm above the trap surface (so that the ion is sandwiched between the trap chip and the mesh). Applying a voltage to the mesh creates a nearly homogeneous electric field (similar

to a parallel plate capacitor) that is perpendicular to the trap surface and pushes the ion vertically, which, for the double well trap, primarily affects the micromotion in the plane of the trap chip that has a component along the wave-vector of the BD beam. For an ion with micromotion due to the RF field, the micromotion velocity varies with time according to $\vec{v} = \vec{v}_0 \cos(\Omega_T t)$, where Ω_T is the RF frequency. In the ion's oscillating frame, the the first-order Doppler shift can be expressed as a phase-modulation of the laser field [Keller et al., 2015]:

$$\vec{E}(t) = \Re(\vec{E}_0 e^{i(\omega_L t + \phi(t))}) = \Re(\vec{E}_0 e^{i(\omega_L t + \frac{\vec{k}\cdot\vec{v}_0}{\Omega_T}\cos(\Omega_T t))}), \tag{4.2}$$

thereby modulating the fluorescence from the near-resonant BD beam that has frequency ω_L and k-vector $\vec{k}$. If the trap drive frequency is larger than the linewidth of the transition, $\Omega_T > \Gamma$, this modulation causes the fluorescence to follow a zero-order Bessel-function pattern with modulation index $\vec{k} \cdot \vec{v}_0/\Omega_T$ as we scan the mesh voltage [Riehle, 2004]. To minimize micromotion in the direction parallel to the BD, we apply a voltage on the mesh corresponding to the maximum of the zero-order Bessel function.

Second, we find the correct axial position. This is not stricly compensating micromotion, since the ion is confined by DC voltages in the axial direction, but there exist stray electric fields in this direction that cause the ion's equilibrium position to differ from the intended, simulated position. We find that the ion is better behaved if we compensate in this direction also. Axial compensation is accomplished by looking at the position of the ion on the camera and changing the "scale," which is a common scaling factor applied to the linear combination of voltages to the different DC electrodes that generates the harmonic confinement in the axial direction (added compensation voltages are unaffected by this scale parameter). If the ion moves after the scale has been changed, we know that the stray fields have not been entirely canceled. Then we apply an axial shim voltage to push the ion until the stray field and compensation field cancel each other. In this case, the ion does not move when the

harmonic potential is scaled.

Finally, we need to compensate the stray field in the remaining direction. The direction of micromotion induced by a stray field in this direction is perpendicular to the electrode plane and BD beam, so we can't use the fluorescence to compensate. Instead, we use the fact that the electrode that we use for microwaves produces a magnetic field gradient along the direction of this micromotion. We drive a current in this electrode at a frequency that is detuned by the RF frequency Ω_T from the $|F, m_f\rangle = |2, 0\rangle \leftrightarrow |1, 0\rangle$ "clock" transition. Due to the micromotion, the magnetic field gradient is translated into an amplitude modulation of the microwave field. An amplitude-modulated oscillating field can be decomposed into the sum and the difference frequency of its carrier oscillation and the frequency of the amplitude modulation. One of these components is on resonance with the clock transition and can drive it with a strength that is proportional to the micromotion amplitude. By adjusting a shim to maximize the π-time of this transition, we can compensate in this final direction. Some amount of iteration among all three of these techniques is necessary to compensate simultaneously in all directions, probably because the compensation fields are not perfectly orthogonal.

4.8.4 State-selective fluorescence detection

Regardless of the experiment we are performing, the information we receive is the number of PMT counts detected when observing ion fluorescence for a given detection period. In nearly all cases, we want to determine whether the ion is "bright," in the $|\downarrow\rangle$ state, or "dark," in the $|\uparrow\rangle$ state or another hyperfine state not resonantly excited by the BD beam. Since there is a non-zero level of background counts (mostly due to stray light from the BD beam), the nominally dark state has an average of 0.3 counts in a 400 μs detection window,

and the bright state typically has an average of 12-15 counts, with both obeying approximately Poissonian statistics. We set a detection threshold of 3 counts, labeling everything below 3 to be dark and everything with 3 counts and above to be bright. We suffer a slightly elevated error compared to ideal Poissonian distributions centered at 0.3 and 15 counts that have very little overlap. Our bright state histogram is not exactly a Poissonian because the bright state can be depumped into other hyperfine levels during the detection period. The deviation of an example bright state histogram from an ideal Poissonian distribution is shown in Fig. 4.18. To some extent this can be mitigated by making sure we have perfectly σ_--polarized light, but the presence of off-resonant magnetic fields produced by the RF trap drive mixes the m_F sublevels, causing some amount of depumping to be unavoidable.

Another possible source of error in the state detection is off-resonantly driving a transition from $|\uparrow\rangle$ into the cycling transition. For this reason we apply two microwave π-pulses, $|\uparrow\rangle \rightarrow |2,-1\rangle$ and $|2,-1\rangle \rightarrow |1,1\rangle$, to shelve $|\uparrow\rangle$ to $|F=1,m_F=1\rangle$ which scatters fewer photons on average.

4.8.5 Motional state analysis

All of the experiments I will describe in the remainder of this thesis involve the motion of an ion, so we need a way of detecting the motion. We can do this by transferring information about the motion to the hyperfine levels of the ion, then reading out via state-selective fluorescence as described above. If the hyperfine state is $|\downarrow\rangle$ and the motional state is restricted to being in only two number states, usually the two lowest, where $|\psi\rangle = |\downarrow\rangle(\alpha|n=0\rangle + \beta|n=1\rangle)$, then we simply need to apply a RSB π-pulse on $|n=1\rangle$, which will flip the spin of the part of the state in $|n=1\rangle$ and remove a quantum of motion, but leave the $|n=0\rangle$ part untouched, so $|\psi\rangle = (\alpha|\downarrow\rangle + \beta|\uparrow\rangle)|n=0\rangle$. We can then detect

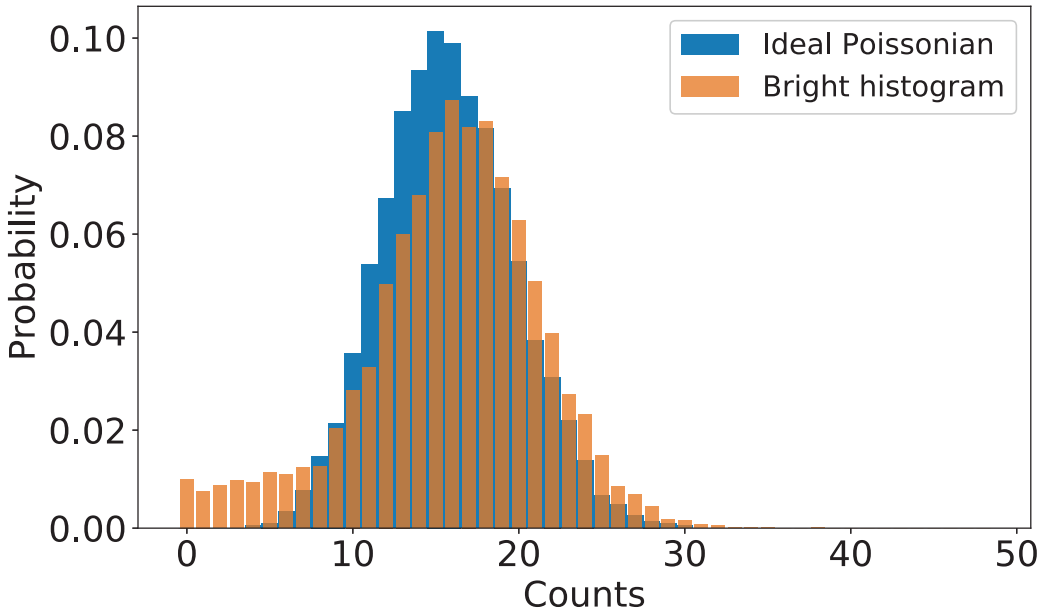

Figure 4.18: Comparison of bright histogram to an ideal Poissonian histogram of same average value. The tail of the histogram is due to depumping from the bright state to darker states during the 400 μs detection period.

in the usual way, by applying the BD resonant laser and observing fluorescence. The probability of observing fluorescence counts above the treshold will be approximately equal to $|\alpha|^2$.

If the motional state is not restricted to two number states, then more complicated techniques are required. Instead of applying a RSB π-pulse, if we scan the duration of the RSB pulse (or BSB or carrier, which work equally well) and observe the fluorescence of the ion as a function of this pulse duration, we obtain a flopping trace, where each part of the motional superposition state is Rabi flopping simultaneously, but with different Rabi frequencies. By determining the Fourier components in the flopping curve, we can determine the relative populations of the various number states that are occupied [Meekhof et al., 1996].

However, the flopping method does not give us all of the relative phase information between different components of the motional state. In order to know everything about the state, we need to perform state reconstruction. One method involves applying a known and variable displacement before obtaining the flopping trace, then repeating the flopping experiments described above many times for different displacement values to obtain the Wigner function of the state [Leibfried et al., 1996]. This is a time-consuming analysis tool that is only performed in rare cases, and in fact is not used in any of the experiments presented here, but I mention it for the sake of completeness.

Chapter 5

Number states

In developing control of the quantum state of a trapped-ion oscillator, a good starting point is to make individual number states. We can use this experiment as a benchmark to measure against other harmonic oscillator systems, including previous trapped-ion experiments [Meekhof et al., 1996], photons [Hofheinz et al., 2008], and mesoscopic mechanical oscillators [Chu et al., 2018]. This is also a metrologically useful class of states for measuring forces that displace the state in phase space [Ziesel et al., 2013; Wolf et al., 2018]. Below I will discuss how we generate the states, our experimental results, and sources of error. I will also propose a protocol for force sensing with high number states outside the Lamb-Dicke regime.

5.1 Producing pure number states

Starting from $|\downarrow\rangle|0\rangle$, the generation of higher number states can be accomplished by first applying a microwave π-pulse to transform the initial state to $|\uparrow\rangle|0\rangle$, followed by a series of alternating red ($|\uparrow\rangle|k\rangle \rightarrow |\downarrow\rangle|k+1\rangle$, RSB) and blue ($|\downarrow\rangle|k\rangle \rightarrow |\uparrow\rangle|k+1\rangle$, BSB) sideband π-pulses at frequencies $\omega_{\downarrow\uparrow} - \omega$ and $\omega_{\downarrow\uparrow} + \omega$ respectively, where ω is the harmonic oscillator frequency. Here, each pulse flips the spin of the internal state and adds a quantum of motion [Meekhof et al., 1996] (Figure 5.1 a and b). In general, we can use sidebands of order l

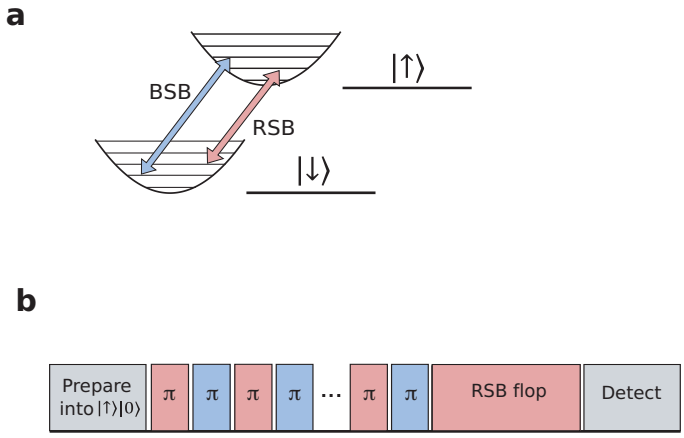

Figure 5.1: Generating number states. a) Relevant energy levels and transitions for motional state creation. Blue sideband (BSB) pulses transfer population between $|\downarrow\rangle|k\rangle$ and $|\uparrow\rangle|k+1\rangle$, while red sideband (RSB) pulses transfer population between $|\uparrow\rangle|k\rangle$ and $|\downarrow\rangle|k+1\rangle$. b) Pulse sequence for generating a harmonic oscillator number state. Alternating RSB and BSB π-pulses are applied, with each pulse adding one quantum of motion (or more quanta on higher order sidebands, see text) and flipping the spin of the state. To analyze the resulting state, a RSB pulse is applied for a variable duration (labeled "RSB flop") and the final spin state is detected via state-selective fluorescence.

at frequencies $\omega_{\downarrow\uparrow} - l\omega$ and $\omega_{\downarrow\uparrow} + l\omega$ to add l quanta of motion with a single π-pulse. While the Rabi frequencies of higher order sidebands on a mode with Lamb-Dicke parameter $\eta < 1$ are suppressed by η^l for small n, for higher number states, the Rabi frequencies can be much larger than that of the first-order sideband [Leibfried et al., 2003] (see Fig. 5.2 d).

We demonstrate control over the motional state of the ion by preparing it in different (approximately pure) number states and Rabi-flopping on RSBs to determine the contrast, decay, and n-dependent Rabi frequency [Meekhof et al., 1996; Leibfried et al., 2003] (see Fig. 5.2 a). With the use of only first-order sidebands to create $|\uparrow\rangle|n = 40\rangle$, we are able to achieve RSB flopping ($|\uparrow\rangle|n = 40\rangle \leftrightarrow |\downarrow\rangle|n = 41\rangle$) with greater than 70 % contrast. If we make use of up to fourth-order sidebands to create the motional state, we observe approximately 50 % contrast when we flop $|n = 100\rangle$ on the fourth-order RSB (Fig. 5.2 b). To verify that the population participating in the fourth-sideband flopping is in the desired number state, we also flop on the second and third-order sideband (Fig. 5.2 c), which have a distinctly different Rabi frequencies, and compare the Rabi frequencies of second to fourth order flopping to theory (colored symbols in Fig. 5.2 d). For the second sideband, we measured a Rabi frequency (in units of Ω_{01}) of 0.2183 ± 0.008 for $n = 100$, which agrees with theory within one standard deviation. The calculated Rabi-frequencies in $n = 99$ and $n = 101$ are more than three standard deviations away from this measured value. Similar comparisons for other values of n further establish confidence that intermediate states are prepared as desired and we can indeed transfer approximately 50 % of the population to $n = 100$.

5.2 Time scales of experiments

The state preparation consists of Doppler cooling (~ 120 μs) followed by ground state cooling (~ 110 μs) and a microwave carrier π-pulse $|\downarrow\rangle \rightarrow |\uparrow\rangle$ (~ 5 μs). At the end of each

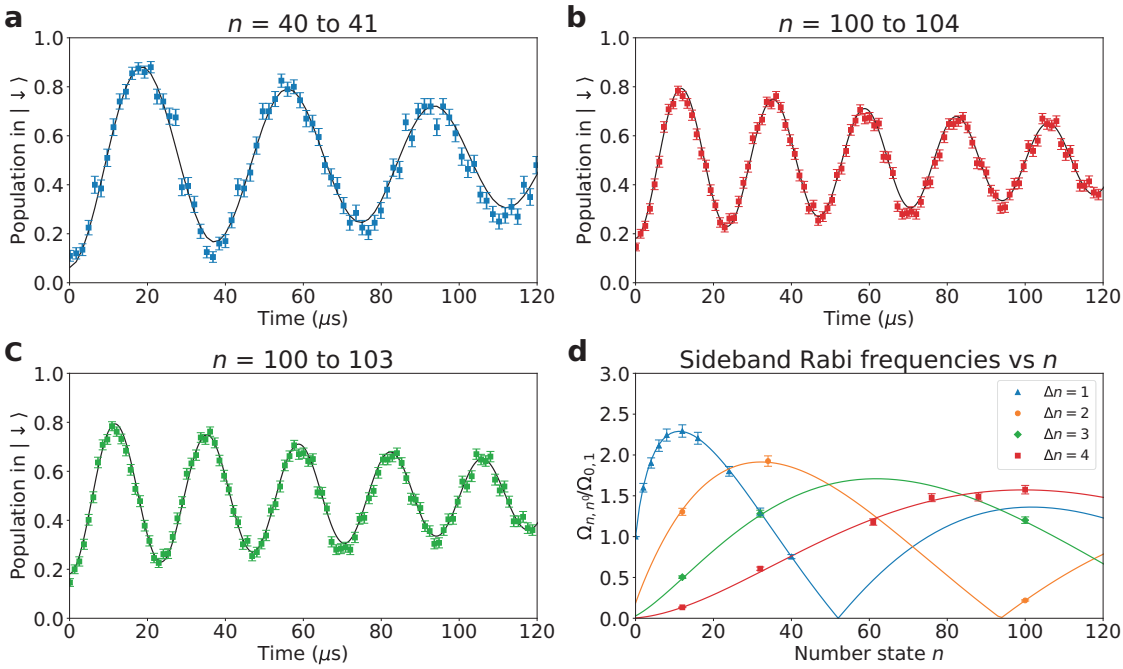

Figure 5.2: Sideband flopping on number states. a) RSB flopping on the 1st-order sideband of an $|\uparrow\rangle|n = 40\rangle$ state prepared using 1st-order RSB and BSB pulses. The curve shows the probability of measuring $|\downarrow\rangle$ as a function of pulse duration during 1st RSB flopping to $|\downarrow\rangle|n = 41\rangle$. Each point represents an average over 200 experiments. The error bars represent one standard deviation of the mean in all figures. Solid black lines show theory fits to the data with the Rabi frequency, the initial contrast and an exponential decay constant as fit parameters. b) RSB flopping on the 4th-order sideband of $|\uparrow\rangle|n = 100\rangle$. The curve shows the probability of measuring $|\downarrow\rangle$ as a function of pulse duration during 4th-order RSB flopping to $|\downarrow\rangle|n = 104\rangle$. Each point represents an average over 500 experiments. c) Same as b on the 3rd-order sideband of $|\uparrow\rangle|n = 100\rangle \leftrightarrow |\downarrow\rangle|n = 103\rangle$. d) First to 4th-order sideband Rabi frequencies. All 1st-order data points (blue triangles) are fit to determine the Lamb-Dicke parameter $\eta = 0.2632(2)$. Curves for higher-orders are plotted for the same η. Measured Rabi-frequencies for higher-order sidebands (colored symbols) are consistent with theory (solid colored lines) for all orders. The π-pulse duration from $|n = 0\rangle$ to $|n = 1\rangle$ is approximately 13 μs. Pulse durations required to produce higher number states can be calculated based on this and the calculated Rabi frequencies for higher number states (see Sec. 5.2).

n	T($\|n\rangle$) (μs)
2	22
4	38
6	51
8	63
12	86
16	109
20	133
40	196
80	293
100	335

Table 5.1: Duration of pulse sequences to produce number states, with a base Rabi frequency $\Omega_{0,1} = \pi/(13\ \mu\text{s})$. Beyond $n = 40$, we make use of higher-order sidebands, which allows us to use transitions with higher Rabi frequencies and skip "rungs" as we move the ion up the number-state ladder.

experiment, a 400 μs detection pulse on the cycling transition is applied. The Raman red sideband $|\uparrow\rangle|0\rangle \rightarrow |\downarrow\rangle|1\rangle$ π-time, which sets the Rabi-frequency $\Omega_{0,1}$, is approximately 13 μs, so the duration of individual experiments can be calculated by using the measured $\Omega_{0,1}$ as a "base" unit to calculate the sideband π-times for higher n according to (see also Eq. 7.10):

$$\Omega_{n,n+s}/\Omega_{0,1} = \eta^{|s|-1}\sqrt{\frac{n_<!}{n_>!}}L_{n_<}^{|s|}(\eta^2) \tag{5.1}$$

where $L_n^{|s|}$ is the generalized Laguerre polynomial and $n_>$ ($n_<$) is the greater (lesser) of $n+s$ and n (these Laguerre functions are plotted in Fig. 5.2d). We can then sum the durations of the individual sideband pulses used. Table 5.1 lists durations of the sequences used to generate the number states. It is possible to substantially decrease these durations, as long as the sidebands are still resolved.

5.3 Exploring error sources and resulting populations through simulations

We believe that the decay in contrast of the high-n flopping traces is largely due to Raman beam pointing fluctuations on the ion, causing the intensity (and hence, the Rabi frequency) to fluctuate. This not only will cause decay in contrast even for a perfectly prepared number state (since we are averaging over 100s of flopping experiments with slightly different Rabi frequencies), but it will also contribute significantly to imperfect state preparation.

We think that, while there is some dispersion around the nominal n value from heating, most of our initial loss in flopping contrast and subsequent decay is due to small amounts of population left in each number state as we move the ion up the number state ladder.

Figure 5.3a shows the resulting 3rd sideband flopping from a simulation with a random error ($\sigma = 3\%$) in each preparation pulse and including heating (rate of 17 quanta/s determined in independent experiments). The final state has 44(2)% population in the target $n = 100$ level (see Fig. 5.3b) in the histogram obtained by averaging over 30 runs of the simulation. The flopping trace produced by this distribution looks very similar to the experiment (Fig. 5.2c).

5.4 Potential application: force-sensing with number states

Number states up to $n = 3$ have recently been demonstrated to exhibit quantum-enhanced sensitivity to displacements [Wolf et al., 2018]. Notably, this enhancement is in all directions, regardless of the phase of the displacement, unlike squeezed states, for example.[1] We believe that with our ability to produce very high number states, we can potentially

[1] If one has two harmonic oscillators, it is possible to measure displacements in both phase space quadratures by using two-mode squeezed states. With only one harmonic oscillator, though, Fock states are the

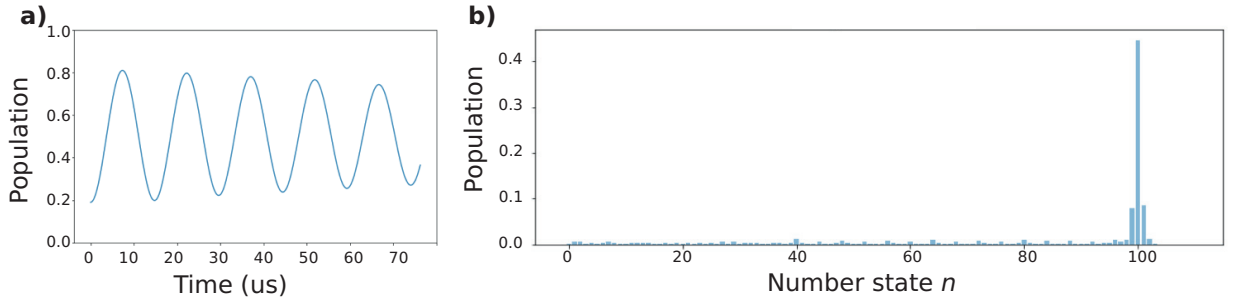

Figure 5.3: Simulation of $n = 100$ number state creation with random error ($\sigma = 3\%$) per sideband pulse and 17 quanta/s heating rate. a) 3rd-order sideband flopping on resulting state, and b) histogram of population in number states up to $n = 110$.

demonstrate an even higher sensitivity to forces than this previous work from [Wolf et al., 2018], which demonstrated a 1.3 dB enhancement over the standard quantum limit with an $n = 1$ number state. A typical method for detecting displacements from the ground state is to apply a RSB π-pulse to an ion in $|\downarrow\rangle|m\rangle$, where $|m\rangle$ is the motional state. The RSB transfers information about the motion into the spin, which allows us to read out via state-selective fluorescence (see Ch. 4.8.5). The main feature of the ground state that allows this method to work is that the RSB does not couple to $|\downarrow\rangle|n = 0\rangle$. There are other values of n which do not couple, or couple very weakly, to certain sideband interactions; these are the points of zero Rabi frequency, plotted for our Lamb-Dicke parameter in Fig 5.2d above. If we produce a number state $|n\rangle$ and then the state is displaced by a small amount ϵ, the resulting state following this displacement is:

$$|\Psi\rangle = \hat{D}(\epsilon)|\downarrow\rangle|n\rangle \approx |\downarrow\rangle C(\epsilon\sqrt{n+1}|n+1\rangle - \epsilon^*\sqrt{n}|n-1\rangle + |n\rangle), \tag{5.2}$$

where $\hat{D}(\epsilon) = e^{\epsilon\hat{a}^\dagger - \epsilon^*\hat{a}}$ is the displacement operator and $C = \frac{1}{\sqrt{|\epsilon|^2(2n+1)+1}}$ is a normalization factor. If the Rabi frequency $\Omega_{n,n'} = 0$, then following an approximate sideband π-pulse on the $|\downarrow\rangle|n+1\rangle \leftrightarrow |\uparrow\rangle|n'+1\rangle$ and the $|\downarrow\rangle|n-1\rangle \leftrightarrow |\uparrow\rangle|n'-1\rangle$ transitions, then the probability of measuring the state in $|\uparrow\rangle$ is:

$$P(|\uparrow\rangle) \approx |\epsilon|^2(2n+1) \tag{5.3}$$

optimal state for the phase-insensitive measurement.

for $\epsilon \ll 1$. The use of the number state enhances the signal by a factor of order n over the displaced ground state experiment. Fig. 5.4 shows an example of the signal vs. displacement for different number states, compared with the ground state. In this simulation, the Lamb-Dicke parameter is adjusted from $\eta \approx 0.22$ (for $n = 70$) to $\eta \approx 0.30$ (for $n = 40$) so that the target number state coincides with a zero of either the 1st- or 2nd-order sideband Rabi frequency (switching from 1st- to 2nd-order for $n = 60$ and higher to maintain reasonable values of η). Adjusting η can be achieved by adjusting the strength of the ion's confinement to change the extent of the ground-state wavefunction or by changing the k-vector difference of the Raman beams. The values in Fig. 5.4 correspond to a range of mode frequencies from approximately 5 MHz to 9.3 MHz, which is easily achieved in our apparatus. These initial simulations hold promise for potentially measuring displacements 25 times smaller than we could with the ground state. Similar performance with a squeezed state of motion would require nearly 30 dB of squeezing, and would only be sensitive to displacements along directions with reduced uncertainty in the squeezed state.

For small displacements, this method is equivalent to measuring the overlap of the state prior to displacement with the final, displaced state, as in Ref. [Wolf et al., 2018]. In this reference, they also show that a perfect overlap measurement saturates the Quantum Cramer-Rao bound. Our proposal is an alternative scheme for measuring the overlap, which might be more practical for higher number states.

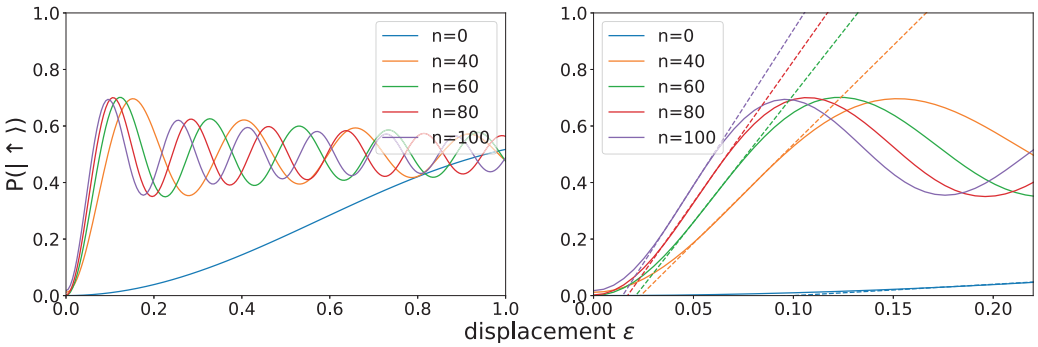

Figure 5.4: a) Simulation of force-sensing protocol for number states up to n=100. b) Zoomed in, with dashed lines tangent to curves at point of maximal slope.

Chapter 6

Mode-frequency sensing with number state superpositions

As mentioned in Ch. 2, superpositions of the form $|0\rangle+|n\rangle$ are great tools for measuring the harmonic oscillator frequency. In fact, given the constraint that we cannot use number states higher than $|n\rangle$, the $|0\rangle + |n\rangle$ state allows us to measure the oscillation frequency with the best sensitivity possible, at the Heisenberg limit. Below I will discuss how we use these states to measure the oscillation frequency, how we generate the states, and our experimental results involving characterizing the states and measuring the ion oscillation frequency over time. Finally, I will discuss possible extensions of this work.

6.1 Principle of operation

Enhanced interferometric sensitivity of superpositions of eigenstates depends on the difference in energy between the two states—in the experiments here where the first state of the superposition is the ground state this energy difference scales linearly with n. We consider a harmonic oscillator with a frequency of oscillation $\omega_0 + \delta\omega(t)$, where $\delta\omega(t)$ is a small, time-dependent correction due to noise and drift relative to the frequency ω_0 of an ideal reference oscillator, which we will call a local oscillator in keeping with common terminology. We implement a Ramsey-type experiment, where the first effective $\pi/2$-pulse creates the state $|\Psi_n\rangle = \frac{1}{\sqrt{2}}(|0\rangle + |n\rangle)$, where n denotes the Fock state number (in the remainder of this chapter we will omit normalization). In a frame rotating at the local

oscillator frequency, $|0\rangle$ and $|n\rangle$ will acquire a relative phase between the two states that is proportional to n and equal to the integral of the fluctuations $\delta\omega(t)$ over time T. After a duration T the state is

$$\begin{aligned} |\Psi_n\rangle_T &= |0\rangle + e^{in\phi}\,|n\rangle\,, \\ \phi &= -\int_0^T \delta\omega(t)dt. \end{aligned} \tag{6.1}$$

Subsequently, a second effective $\pi/2$-pulse synchronous with the local oscillator recombines the number-state superposition to the ground state if $n\phi = (2m+1)\pi$ or to $|n\rangle$ if $n\phi = 2m\pi$ with m an integer. For general ϕ, the final state (up to a global phase) is $|\Psi_n\rangle_f = \cos(n\phi/2)\,|n\rangle - i\sin(n\phi/2)\,|0\rangle$, with a probability of being in the ground state given by

$$P_0 = 1/2[1-\cos(n\phi)]. \tag{6.2}$$

To characterize the harmonic oscillator in interferometric measurements, we want to determine small deviations of ϕ around some nominal value with maximal sensitivity. This occurs when the slope $|\partial P_0/\partial\phi| = |n/2\ \sin(n\phi)| = n/2$, namely when $n\phi \simeq m\pi/2$, with m an odd integer ($m = \pm 1$ in the tracking experiments described below). We want to minimize

$$\delta\phi = \frac{\Delta P_0}{|\partial P_0/\partial\phi|}, \tag{6.3}$$

where $\Delta P_0 = \sqrt{\langle P_0^2\rangle - \langle P_0\rangle^2}$ is the standard deviation of a population measurement that can discriminate between $|0\rangle$ and $|n\rangle$. To a good approximation, the measurement is projection noise limited [Itano et al., 1993], which implies $\Delta P_0 = \sqrt{P_0(1-P_0)}$. For $n\phi \simeq m\pi/2$, $\Delta P_0 = 1/2$ and $\delta\phi = 1/n$, which is the Heisenberg limit and can only be reached with nonclassical oscillator states. In fact, the state $|0\rangle + |n\rangle$ satisfies the Margolus-Levitin bound for the maximal rate of evolution [Margolus and Levitin, 1998], implying that no other combination of states with quantum numbers between 0 and n can produce interference fringes with higher sensitivity to motional frequency changes. The phase uncertainty of classically behaving interferometers, which we define as those that use coherent oscillator states of the

same average excitation number $\bar{n} = n/2$ and measurements of the oscillator energy (equivalent to the mean occupation number), will only reduce as $\delta\phi_{\text{class}} = \sqrt{1/n}$ (see Appendix A).

In practice, the effective $\pi/2$-pulses will not have perfect fidelity and there will be added noise above the fundamental projection noise. Such imperfections reduce the contrast C ($0 \leq C \leq 1$) from the ideal value $C = 1$, which can be incorporated as $P_0 = C/2[1-\cos(n\phi)]$. In our experiments C decreases as the complexity of preparing superpositions increases with larger n. Additionally, since a single experiment only gives us one bit of information (the ion is found in either $|0\rangle$ or $|n\rangle$), we need to perform multiple experiments to accumulate statistics to determine a phase shift. If the mode-frequency noise is not stable over the time period required to acquire statistics, then the contrast of our interferometer is reduced. This becomes more of a problem with the higher order interferometers, since the susceptibility to mode-frequency noise increases with n. This limits the measurable gains in sensitivity to $n \leq 12$ in our specific experimental setting (see below).

6.2 Number-state superposition creation

The motional superposition $|\uparrow\rangle(|0\rangle + |2\rangle)$ is straightforward to prepare by replacing the first RSB pulse by a $\pi/2$-pulse $|\uparrow\rangle|0\rangle \rightarrow |\uparrow\rangle|0\rangle + |\downarrow\rangle|1\rangle$ followed by a BSB π-pulse, which transforms $|\downarrow\rangle|1\rangle \rightarrow |\uparrow\rangle|2\rangle$ while not affecting $|\uparrow\rangle|0\rangle$ (see Fig. 1 a). To realize the effective $\pi/2$-pulse $|0\rangle \rightarrow |0\rangle + |n\rangle$ when $n > 2$, after the initial RSB $\pi/2$-pulse the $|\uparrow\rangle|0\rangle$ component is "shelved" with a microwave π-pulse to $|\text{aux}\rangle|0\rangle$ that is unaltered by subsequent pairs of BSB and RSB π-pulses that promote the $|\downarrow\rangle|k\rangle$ component to $|\downarrow\rangle|k+2\rangle$. The preparation is finished by a final microwave π-pulse $|\text{aux}\rangle|0\rangle \rightarrow |\uparrow\rangle|0\rangle$ and a BSB pulse $|\downarrow\rangle|n-1\rangle + |\uparrow\rangle|0\rangle \rightarrow |\uparrow\rangle(|0\rangle + |n\rangle)$ that promotes the $|\downarrow\rangle|n-1\rangle$ component to $|\uparrow\rangle|n\rangle$ while leaving the $|\uparrow\rangle|0\rangle$ component unaltered.

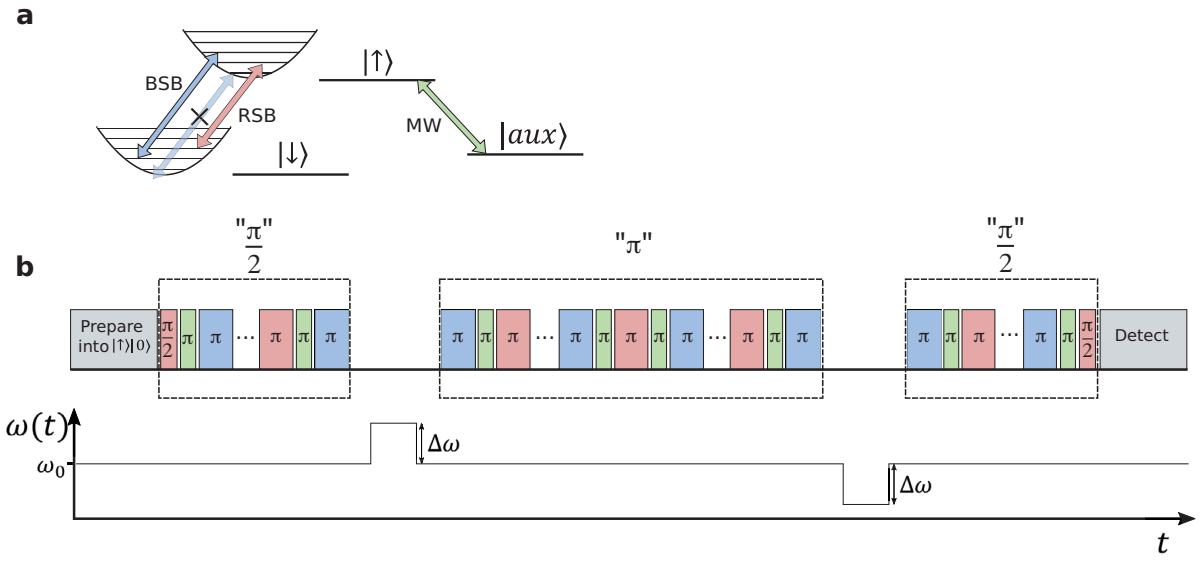

Figure 6.1: Generating superpositions of number states. a) Relevant energy levels and transitions for motional state creation. Blue sideband (BSB) pulses transfer population between $|\downarrow\rangle|k\rangle$ and $|\uparrow\rangle|k+1\rangle$, while red sideband (RSB) pulses transfer population between $|\uparrow\rangle|k\rangle$ and $|\downarrow\rangle|k+1\rangle$. The blue sideband does not couple to $|\uparrow\rangle|0\rangle$ (crossed out, faded blue arrow) because there is no energy level below the ground state. Transitions between the states $|\uparrow\rangle$ and $|aux\rangle$ are driven by a microwave field (MW, indicated in green), which does not change k. b) Pulse sequences and trap frequencies for number-state interferometers. To characterize the interferometers, the first effective $\pi/2$-pulse (labeled "$\pi/2$") creates $|0\rangle+|n\rangle$, followed by a free-precession period during which the mode frequency is deliberately increased by $\Delta\omega$. An effective π-pulse ("π") swaps the phase of the superposition, $|0\rangle + e^{i\phi}|n\rangle \rightarrow e^{i\phi}|0\rangle + |n\rangle$. After another free-precession period with the mode frequency reduced by $\Delta\omega$, a final effective $\pi/2$-pulse closes the interferometer. For the composition of effective pulses see text.

6.3 Interferometer characterization

We characterize the enhanced sensitivity of each interferometer by inserting an effective "spin-echo" type π-pulse between wait periods of duration T and purposely induce trap frequency changes $\Delta\omega$ with equal magnitude and opposite sign before and after the echo pulse (Fig. 6.1 c). We use this echo technique because trap frequency fluctuations or drifts that alter the mode frequency by approximately the same amount in both arms are suppressed. For the first wait period this ideally results in an order-dependent phase $\phi = -n\ \Delta\omega\ T$. The echo pulse is composed of the following steps: first the pulses of the effective $\pi/2$-pulse are applied in reverse order to ideally give $|\uparrow\rangle(|0\rangle + e^{i\phi}|n\rangle) \rightarrow |\uparrow\rangle|0\rangle + e^{i\phi}|\downarrow\rangle|1\rangle$. Second, a RSB π-pulse results in $e^{i\phi}|\uparrow\rangle|0\rangle + |\downarrow\rangle|1\rangle$, which is then walked up the number-state ladder as described for the first effective $\pi/2$-pulse. Ideally the effective echo π-pulse accomplishes $|0\rangle + e^{i\phi}|n\rangle \rightarrow e^{i\phi}|0\rangle + |n\rangle$. In this way, the induced trap frequency change $-\Delta\omega$ during the second wait period constructively adds to the interferometer phase $e^{i\phi}|0\rangle + |n\rangle \rightarrow e^{i\phi}|0\rangle + e^{-i\phi}|n\rangle$, which is transformed to $-i\sin(\phi)|\downarrow\rangle|1\rangle + \cos(\phi)|\uparrow\rangle)|0\rangle$ by the final effective $\pi/2$-pulse, so the induced interferometer phase ϕ can be read out by measuring the probability to find $|\downarrow\rangle$.

We find that as we increase n in the superposition for $T = 100\ \mu$s, the phase accumulation increases linearly with n as expected, but, due to accumulated imperfect state preparation steps, the contrast of the interference fringes (and therefore the fringe slope) is reduced (see Fig. 6.3 a), reducing the signal in Eq.(6.3) of the higher-order interferometers. Given this effect, we observe the highest sensitivity with the $|0\rangle + |12\rangle$ superposition state, which achieves a 8.5(2) dB (7.1(4) times) improvement over a perfect $|0\rangle + |1\rangle$ interferometer (Fig. 6.3 b). The $n = 12$ interferometer also performs 3.2(2) dB better than an ideal classical interferom-

eter (see Appendix A). To similarly increase sensitivity with ideal squeezed states [Loudon, 2000], we would require approximately 6 dB of squeezing below the vacuum noise for the ideal interferometer.

6.4 Mode-frequency tracking with number-state interferometers

We can use this enhanced sensitivity to precisely track motional mode frequency changes over time. We perform two Ramsey-type experiments with the phase of the final effective $\pi/2$-pulses equal to $\pm\pi/2$ so that when the pulses are resonant with the mode frequency, the resulting $|\downarrow\rangle$ population from each Ramsey experiment is ideally 1/2. A difference between the populations for the $+\pi/2$ and $-\pi/2$ cases provides an error signal that we feed back to the local oscillator to follow the fringe pattern as the mode frequency drifts due to changes in stray electric fields and the sources providing the electrode potentials.

This procedure is complicated by the fact that the sideband transition frequencies are shifted by the AC Stark effect from the Raman beams. These result in phases beyond those described in Eq. (1) that shift the interferometer fringes. To mitigate this effect, as well as to subtract out non-zero phase accumulation during the creation of the superposition state, we use auto-balanced Ramsey spectroscopy [Sanner et al., 2017]. Instead of using two Ramsey experiments that provide the error signal used to feed back to the pulse frequency, we interleave four Ramsey experiments with two different Ramsey times, T_{short} and T_{long} (typically 20 μs and 100 μs, respectively). The phase between the two $\pi/2$-pulses is adjusted to compensate for systematic phases according to the error signal from the short Ramsey experiments, and the frequency of the local oscillator is adjusted according to that from the long Ramsey experiments. These phase and frequency adjustments are applied equally to both the short- and long-pulse Ramsey experiments. This suppresses all contributions to

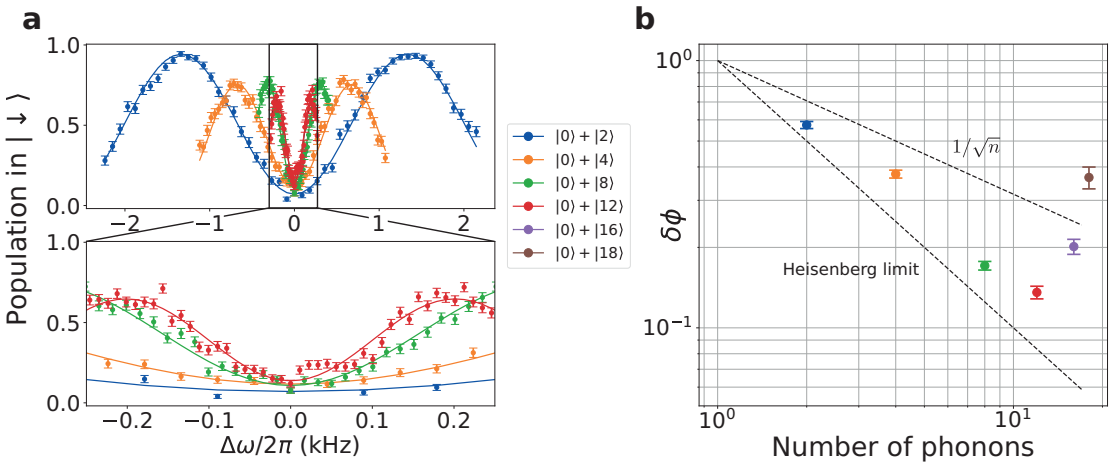

Figure 6.2: Interference and sensitivity of different number-state superpositions. a) Interference fringes for number state interferometers with n= 2, 4, 8 and 12. Each data point is averaged over 250 experiments and uses a wait time of 100 μs before and after the effective π-pulse. The fringe spacing is reduced as $1/n$ as expected for Heisenberg scaling. At the same time, the fringe contrast is reduced with higher n due to the larger number of imperfect pulses and the higher susceptibility to mode-frequency changes that are not stable over all 250 experiments for each data point. This reduces the fringe slopes for $n > 12$ below the maximal slope reached for $n = 12$. b) Experimentally determined noise-to-signal ratio $\delta\phi$ as defined in Eq.(6.3) as a function of order n (colored dots) together with the theoretical lines for a perfect classical interferometer at $1/\sqrt{n}$ and the $1/n$ Heisenberg limit valid for ideal number-state interferometers.

phase accumulation other than the phase difference accumulated due to the different free-precession times, which is unperturbed by laser beam couplings [Sanner et al., 2017]. This procedure is described in more detail in Sec. 6.5.3 below.

When tracking the mode frequency in this way we can record the frequency error versus time for different-n interferometers. We can then determine the overlapping Allan deviation [Howe et al., 1981] as a function of averaging interval and compare it for the different interferometers (Fig. 6.4 a). This data was taken while interleaving experiments with the $|0\rangle + |2\rangle$, $|0\rangle + |4\rangle$, $|0\rangle + |6\rangle$ and $|0\rangle + |8\rangle$ interferometers to allow for a direct comparison of their sensitivity under the same noise and drift conditions. For long averaging periods, trap frequency drifts dominate the uncertainty. As expected, this gives the same asymptotic long-time slope of the Allan deviation for all interferometers. Importantly, the increased sensitivity of higher-n interferometers reduces the time interval required to average down to a certain level for $n \leq 8$. For the $n = 8$ interferometer, we observe the minimum Allan standard deviation at approximately 23 s of averaging in this interleaved comparison. By running only the $n = 8$ interferometer sequences, we increase the measurement duty cycle which accelerates the rate with which the Allan deviation approaches its minimum. Under these conditions, the minimal fractional frequency Allan deviation of $2.6(2)\times10^{-6}$ ($\sim$ 19 Hz at 7.2 MHz) is reached at approximately 4 seconds of averaging (red triangles in Fig. 6.4 b). To further increase the measurement rate, we record the population differences determined in all four Ramsey experiments comprising the auto-balance sequence without feeding back on the local oscillator frequency. This eliminates the latency due to computer control of the frequency tracking. As long as the populations of four Ramsey experiments uniquely determine the frequency change, we can run a series of $n = 8$ interferometer experiments, each taking 4 ms, without feedback to shorten the time to reach the minimum of $2.9(4)\times10^{-6}$ to approximately 0.5 s before the uncompensated mode frequency drift produces an increasing Allan deviation (Fig. 6.4 b, blue circles). While the minimum value of the Allan deviation

is not lower when taking data in this fashion as compared to when tracking the drift, this experiment gives an idea of how quickly we could average down to the level of a few parts in 10^{-6} if tracking latency is minimized. We suspect that the Raman beams contribute to charging the trap and increasing mode-frequency instabilities (see Sec. 6.5.2), so we attribute the difference in drift rate between Fig: 6.4a) and b) to the difference in Raman beam duty cycle.

6.5 Experimental details

6.5.1 Time scales of experiments

As with experiments described in Ch. 5, the state preparation consists of Doppler cooling ($\sim$ 120 μs) followed by ground state cooling ($\sim$ 110 μs) and a microwave carrier π-pulse $|\downarrow\rangle \rightarrow |\uparrow\rangle$ ($\sim$ 5 μs). At the end of each experiment, a 400 μs detection pulse on the cycling transition is applied. The Raman red sideband $|\uparrow\rangle|0\rangle \rightarrow |\downarrow\rangle|1\rangle$ π-time, which sets the Rabi-frequency $\Omega_{0,1}$, is approximately 13 μs, so the duration of individual experiments can be calculated by using $\Omega_{0,1}$ as a "base" unit to calculate the sideband π-times for higher n according to Eq. 7.10. We can then sum the durations of the individual sideband pulses and of the $\sim$ 5 μs microwave $|\uparrow\rangle \rightarrow |aux\rangle$ π-pulses used. Table 6.1 lists durations of the sequences used to generate number state superpositions. It is possible to substantially decrease these durations, as long as the sidebands are still resolved.

The sidebands in our interferometers rely on the same Raman laser coupling that is used in most two-qubit gates, so the time scale for a single BSB or RSB pulse is on the same order as a typical gate time. This limits the usefulness for improving gate fidelity, but interferometric tracking would certainly help with longer-term drifts and reduce the duration required to measure the trap frequency with a certain precision.

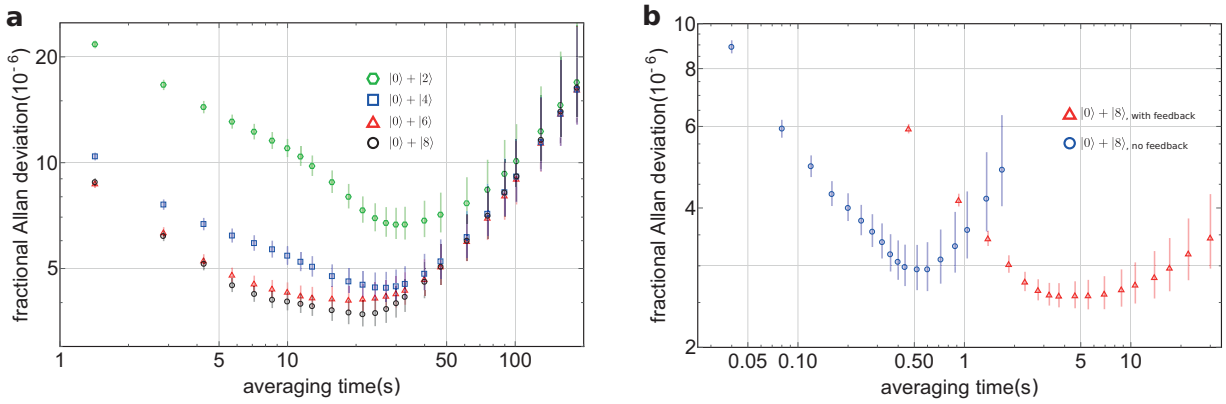

Figure 6.3: Oscillator frequency tracking using number-state interferometers. a) Interleaved comparison of the Allan standard deviation of tracked fractional trap frequencies vs. averaging time found with $n = 2$, $n = 4$, $n = 6$ and $n = 8$ interferometers. The repetition rate of a single run, comprised of long (100 μs Ramsey time) and short (20 μs Ramsey time) auto-balance sequences on both sides of the fringe respectively, was approximately 7/s. The $n = 8$ interferometer produces the lowest fractional frequency Allan deviation. Trap frequency drifts begin to dominate the Allan deviation at 10's of seconds. b) Fractional mode-frequency uncertainty vs. averaging time for two series of $n = 8$-only interferometer runs to maximize measurement duty cycle. We are able to achieve a minimal fractional frequency Allan deviation of 2.6(2) $\times 10^{-6}$ at approximately 4 seconds of averaging time with feedback activated (red triangles) and an experiment rate of approximately 43/s as defined above. The Allan standard deviation for averaging times up to 1 s without feedback activated is shown by the blue circles. The minimum is reached after 0.5 s with the experiment rate increased to approximately 250/s.

n	T($\|0\rangle + \|n\rangle$) (μs)
2	16
4	41
6	54
8	66
12	89
16	112

Table 6.1: Duration of pulse sequences to produce number-state superpositions, with a base Rabi frequency $\Omega_{0,1} = \pi/(13\ \mu\text{s})$.

6.5.2 Sources of decoherence

At the 7.2 MHz axial mode frequency, the heating rate is relatively low, approximately 17 quanta/s. Consequently, the dominant source of decoherence in these experiments is dephasing due to fluctuations in the mode frequency. These fluctuations probably arise from technical noise from the voltage source, uncontrolled charging from stray light scattering off the dielectric material between the trap electrodes and amplitude instabilities in the rf source that generates the pseudo-potential. We also attribute longer time-scale drift, on the order of minutes to hours and a magnitude of $\sim 1 - 10$ Hz/s to uncontrolled charging and discharging. This charging affects mode-frequency tracking experiments and leads to unpredictable deviations from the ideal white-noise $1/\sqrt{\tau}$ behavior during experimental runs to determine Allan-variances. A more detailed investigation of this noise and ways to further suppress it is currently in progress in our laboratory.

6.5.3 Auto-balanced frequency tracking experiments

The auto-balanced sequence (see Fig. 6.4) for mode-frequency tracking is comprised of four interleaved Ramsey experiments, two each with Ramsey times t_{short} and t_{long}, where the phase of the second effective $\pi/2$-pulse is $+\pi/2$ relative to the first $\pi/2$-pulse for one of the experiments and $-\pi/2$ for the other. For a given Ramsey time, the two experiments with $+\pi/2$ and $-\pi/2$ relative phase interrogate the fringe close to its largest positive and negative slope respectively. If the long Ramsey experiments are on exact resonance, both should result in the same average population in $|\downarrow\rangle$, so the signal difference is zero on average. If the Ramsey experiment is off resonance, the signal difference provides a non-zero error

signal p_{long} which is used to calculate the offset $\delta\omega$ between the assumed mode frequency ω_a and the actual mode frequency. The offset $\delta\omega$ is fed back to the local oscillator (LO), which updates its frequency to $\omega = \omega_a + \delta\omega$. This in turn updates the frequency of the BSB and RSB pulses to $\omega_{LO} = \omega_{\downarrow\uparrow} + \omega_a + \delta\omega$ and $\omega_{LO} = \omega_{\downarrow\uparrow} - \omega_a - \delta\omega$, respectively, where $\hbar\omega_{\downarrow\uparrow}$ is the energy difference between $|\uparrow\rangle$ and $|\downarrow\rangle$, as described in the main text. The short Ramsey experiments provide an error signal p_{short}, as described above, which is now used to compute a phase offset $\delta\phi$ that is added to the relative phase between the two effective π-pulses, $\phi_{LO} = \pm\pi/2 + \delta\phi$. Feedback on this phase reduces "frequency pulling" due to non-zero phase accumulation during the pulses, which can be caused by slowly drifting, pulse-synchronous systematic errors such as AC-Stark shifts. For a more detailed description of the auto-balanced Ramsey technique, see Ref. [Sanner et al., 2017].

6.5.4 Anharmonic contributions

We do not expect the anharmonicity of the trapping potential to be a significant limitation or source of systematic error. Previous calculations [Home et al., 2011] for a similar trap and estimates based on a numerical simulation of our current trap predict an anharmonic component of a few parts in 10^{-7} per quantum on the axial mode frequency. With a maximal superposition state of $|0\rangle + |8\rangle$ used in the mode-tracking experiments, this would cause an offset of $\sim 1 \times 10^{-6}$, which is within the minimum measurement uncertainty.

6.6 Extensions to work

In a natural extension of the work presented here, it should be possible to observe such mode-frequency noise during free precession by refocusing with one or more effective π-pulses. This would allow us to filter the response of the ion to certain spectral components

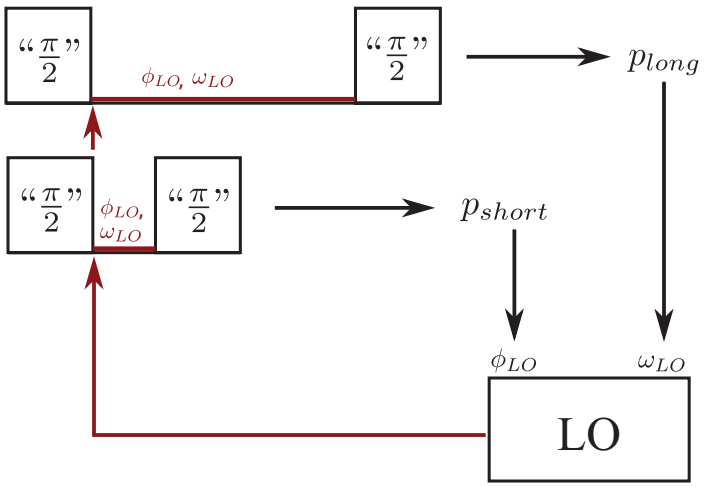

Figure 6.4: Schematic illustrating the auto-balanced feedback loop applied to local oscillator (LO), a frequency source used as a reference to compare to the ion's oscillation frequency. The LO controls the phases and frequencies of the BSB and RSB laser-pulses (see Fig. 6.1) during mode-frequency tracking experiments. The difference between the populations measured after a pair of Ramsey experiments with long wait times provides an error signal, p_{long}, used to feed back on the LO frequency, ω_{LO}. Similarly, a second pair of Ramsey experiments with short wait times provides and error signal, p_{short}, used to feed back on an additional LO phase offset ϕ_{LO} between the first and second effective $\pi/2$-pulses. The long and short Ramsey experiments are interleaved, with ϕ_{LO} and ω_{LO} applied equally to both. For more details on auto-balanced Ramsey experiments, see Ref. [Sanner et al., 2017].

of the motional mode-frequency noise, providing a quantum lock-in analyzer in analogy to characterizations of magnetic field noise with a trapped ion [Kotler et al., 2011]. By using number-state superpositions, we can transfer the quantum advantage demonstrated in the experiment reported here to achieve "quantum gain" in such lock-in measurements. These quantum-enhanced spectrum analysis experiments have been led by Jonas Keller and will be written up soon.

More generally, we expect that the techniques demonstrated here can be applied to characterize other harmonic oscillators in the quantum regime with increased precision and on time scales that were previously inaccessible. Such capabilities could support quantum metrology and improve the prospects of fault-tolerant quantum information processing, where some of the most advanced experimental platforms are limited by harmonic oscillator coherence.

Chapter 7

Mode-frequency sensing with coherent displacements

The third set of experiments based on generating a "quantum" state of motion I will discuss is with coherent displacements [McCormick et al., 2019b]. As discussed previously, coherent states are classically behaving quantum states, so we will not gain quantum enhancement from this method, unless we perhaps coherently displace non-classicial states of motion in a hybrid approach. The coherent displacements are produced by tickling (see Sec. 4.2.8) the ion, which is relatively simple to implement in the lab. Because of the ease of implementation and short operation time (typically $\sim 1\ \mu$s), we still are able to characterize the ion's motion with a sensitivity on the order of that of the best superposition state we used by operating at higher average occupation numbers. In this chapter, I will discuss the quantum theory of coherent displacements and experiments we performed involving coherent displacements of number states, including spectral analysis of the mode frequency noise using a series of coherent displacements with alternating signs.

7.1 Introduction

The manipulation of quantum states of a harmonic oscillator is a theme of current interest across a wide range of experimental platforms. Often the methods developed on one platform, in our case a single, harmonically bound atomic ion, can be adapted to many other

platforms, after suitable modifications of the original procedures. An important example is resolved sideband-cooling of micro-fabricated oscillators, theoretically described in [Wilson-Rae et al., 2007; Marquardt et al., 2007], that bears strong analogies to the methods that were first developed for single-ion mechanical oscillator systems [Neuhauser et al., 1978; Wineland and Itano, 1979; Diedrich et al., 1989]. In this chapter, ground-state cooling is combined with another basic idea that is widely applicable across harmonic oscillator platforms, namely coherent displacements that can be conveniently implemented with a classical force that is near resonant with the harmonic oscillator frequency [Carruthers and Nieto, 1965]. The added ingredient used here is a suitable two-level system, in our case two internal electronic states of a single ion, that can be coupled to the harmonic oscillator motion and read out with a projective measurement to gain information about the state of the harmonic oscillator. A superconducting qubit is just one example of an effective two-level system that has been coupled to a co-located micro-fabricated harmonic oscillator [Chu et al., 2018]. Therefore, the methods described in this chapter might also be adaptable and useful to the rapidly growing community that studies harmonic oscillator systems in the quantum regime.

Exciting the harmonic oscillator motion of trapped charged particles with a weak oscillating electric field has long been used to determine motional frequencies and subsequently the charge-to-mass ratio in various ion trap based devices, for example in ion-trap mass spectrometers [Paul and Steinwedel, 1953; Myers, 2013] (see also Sec. 4.2.8). The response of the ions can be detected by counting resonantly ejected particles, by resonance absorption of the driving field [Dehmelt and Major, 1962], or through image currents in the trap electrodes [Dehmelt and Walls, 1968]. For certain atomic ions, it is possible to detect the ion motion through changes of scattered light that depends on velocity via the Doppler effect [Wineland et al., 1983] (see also Sec. 4.2.8). An important practical advantage of a tickle is that it only interacts with the charge of the ion, therefore it is immune to magnetic field or AC-Stark shifts that may restrict how well the harmonic oscillator frequency can be

determined spectroscopically, for example by resolving the motional sidebands of internal transitions of ions [Leibfried et al., 2003]. Many other harmonic oscillator systems have analogous mechanisms available, for example excitation of a micro-fabricated resonator by driving it with a piezo-electric element or with a capacitively coupled electric circuit.

The tickle method can be further refined with atomic ions that are cooled close to the ground state of their motion and can be coupled to a two-level system through resolved sideband transitions [Wineland and Itano, 1979; Leibfried et al., 2003]. Near the ground state of motion ($\bar{n} \ll 1$), the probability of driving a "red sideband" transition, where the internal state change of the ion is accompanied by reducing the number of quanta in the motional state $|n\rangle \rightarrow |n-1\rangle$, is strongly suppressed; this can be used to determine the average harmonic oscillator occupation number $\bar{n}$ [Diedrich et al., 1989; Monroe et al., 1995; Leibfried et al., 2003]. Starting near the ground state, a resonant tickle can add quanta of motion such that the red sideband can be driven again, as discussed qualitatively in [Home et al., 2011]. For weak excitation, $\bar{n} \leq 1$, we observe responses close to the Fourier limit of the tickle pulse, as I will describe in more detail and have experimentally demonstrated.

If the tickle excitation acts longer or with a larger strength, an ion in the ground state can be displaced to coherent states with an average harmonic oscillator occupation number $\bar{n} \gg 1$. The Rabi frequency of sideband transitions depends non-linearly on $\bar{n}$, which leads to collapse and revival of internal state changes that are one of the hallmarks of the Jaynes-Cummings model [Jaynes and Cummings, 1963; von Förster, 1975; Meekhof et al., 1996]. Here we examine the probability of changing the internal state theoretically and experimentally, as a function of tickle detuning relative to the frequency of a harmonic oscillator motional mode of the ion. When probing the red sideband transition after displacing to $\bar{n} \gg 1$, we observe rich sets of features with steep and narrow side lobes around the resonance center. Such nonlinear responses can in principle be used to find the frequency of

the motion with better signal-to-noise ratio than what the Fourier limit implies for smaller coherent states where $\bar{n} \leq 1$ and the response of the ion is essentially linear.

A sequence of coherent displacements alternating with free evolution of the motion, inspired by spin-echos [Hahn, 1950] and dynamical decoupling [Ernst et al., 1987; Álvarez and Suter, 2011], can be used to obtain a frequency-filtered response of the ion. We implement and characterize such sequences by observing and modeling the ion response to deliberately applied, monochromatic modulations of the trapping potential curvature. Similar sequences can then be used without applied modulations. In this case, the response of the ion can be attributed to harmonic oscillator frequency noise that is intrinsic to our system, allowing us to characterize noise on the trap potential in a frequency range of 500 Hz to 400 kHz, a wide frequency range that has not been studied in detail in previous work [Talukdar et al., 2016]. With this method, several narrow band technical noise components (spurs) in our setup were identified through the direct response of the ion. The noise was traced back to digital-to-analog converters (DACs) used in our setup and was eliminated by replacing the DACs with analog power supplies.

7.2 States and ion fluorescence signals from coherent displacements

We consider a single ion with charge q and mass m confined in a harmonic trapping potential with minimum position at $\mathbf{r_0}$, such that the motion of the ion can be described by three normal harmonic oscillator modes with approximate frequencies $\omega_z \leq \omega_y \leq \omega_x$. By using a coordinate system where the axis directions coincide with the normal mode directions, we can write the ion position as $\mathbf{r} = \mathbf{r_0} + \delta\mathbf{r}$. The interaction of the ion with an

additional uniform electric field $\mathbf{E}$ can be described as

$$H_{\mathrm{E}} = q(\mathbf{E} \cdot \delta\mathbf{r}). \tag{7.1}$$

For the normal mode in the z-direction we introduce ladder operators $\hat{a}$ and $\hat{a}^\dagger$ to write a time independent Hamiltonian as

$$H_0 = \hbar\omega_z \hat{a}^\dagger \hat{a}. \tag{7.2}$$

We have suppressed the ground state energy since it is a constant term that does not change the dynamics. The real oscillator we observe in the experiment has frequency noise and is therefore not always sufficiently described by H_0. We will consider the change in dynamics due to frequency noise in more detail in section 3. We replace δz by its equivalent quantum mechanical operator $\delta\hat{z} = z_0(\hat{a}^\dagger + \hat{a})$ with $z_0 = \sqrt{\hbar/(2m\omega_z)}$ the ground state extent of the oscillator. For the normal mode in this direction, and in the interaction picture relative to H_0, the interaction with an oscillating electric field $E_z(t) = E_0 \cos(\omega t + \phi)$ becomes

$$\begin{aligned} H_I &= \hbar\Omega_z(\hat{a}^\dagger e^{i\omega_z t} + \hat{a}e^{-i\omega_z t})(e^{i(\omega t+\phi)} + e^{-i(\omega t+\phi)}) \\ &= \hbar\Omega_z(\hat{a}^\dagger e^{-i(\delta t+\phi)} + \hat{a}e^{i(\delta t+\phi)} + \hat{a}^\dagger e^{i(\sigma t+\phi)} + \hat{a}e^{-i(\sigma t+\phi)}), \end{aligned} \tag{7.3}$$

with the coupling $\Omega_z = qE_0 z_0/(2\hbar)$ and $\delta = \omega - \omega_z$, $\sigma = \omega_z + \omega$. If the oscillating field is close to resonance with the normal mode, $|\delta| \ll \sigma$, the faster-rotating terms containing σ can be neglected to a good approximation and the interaction takes the form of a coherent drive detuned by δ

$$H_I \simeq \hbar\Omega_z(\hat{a}^\dagger e^{-i(\delta t+\phi)} + \hat{a}e^{i(\delta t+\phi)}). \tag{7.4}$$

We can formally integrate the equation of motion for H_I [Carruthers and Nieto, 1965; Glauber, 1963; Leibfried et al., 2003] to connect an initial state $|\Psi(0)\rangle$ at $t = 0$ when the electric field is switched on to the coherently displaced state after evolution for duration t, $|\Psi(t)\rangle$

$$|\Psi(t)\rangle = \hat{D}(\alpha(t))e^{i\Phi(t)} |\Psi(0)\rangle , \tag{7.5}$$

where

$$\begin{aligned}\hat{D}(\alpha) &= \exp(\alpha\hat{a}^\dagger - \alpha^*\hat{a}),\\ \alpha(t) &= -i\Omega_z e^{-i\phi}\int_0^t e^{-i\delta\tau}d\tau = -\Omega_z e^{-i\phi}\frac{1-e^{-i\delta t}}{\delta},\\ \Phi(t) &= \mathrm{Im}\left[\int_0^t \alpha(\tau)\{\partial_\tau\alpha^*(\tau)\}d\tau\right] = \left(\frac{\Omega_z}{\delta}\right)^2[\sin(\delta t)-\delta t].\end{aligned} \tag{7.6}$$

The phase $\Phi(t)$ can play an important role, for example, in two-qubit gates [Leibfried et al., 2003; Lee et al., 2005] or interferometric experiments that combine internal degrees of freedom of the ion with motional states [Monroe et al., 1996; Hempel et al., 2013]. Here, we will be interested only in the average occupation number $\bar{n} = \langle\Psi(t)|\hat{a}^\dagger\hat{a}|\Psi(t)\rangle$, which does not depend on $\Phi(t)$. If the initial state is the harmonic oscillator ground state, $|\Psi(0)\rangle = |0\rangle$ the average occupation is

$$\bar{n}(t) = |\alpha(t)|^2 = 2\left(\frac{\Omega_z}{\delta}\right)^2[1-\cos(\delta t)]. \tag{7.7}$$

On resonance ($\delta = 0$) the coherent state amplitude grows linearly in t as $\alpha(t) = e^{i\phi}\Omega_z t$ and the energy of the oscillator quadratically as $\bar{n}(t) = \Omega_z^2 t^2$. For a coherent state (displaced $n = 0$ ground state), the probability distribution over number states $|m\rangle$ is a Poisson distribution with average $\bar{n}$

$$P_m^{(0)} = \frac{\bar{n}^m e^{-\bar{n}}}{m!}. \tag{7.8}$$

An initial number state with $|\Psi(0)\rangle = |n\rangle$, displaced by $\hat{D}(\alpha_d)$, results in a more involved probability distribution [Carruthers and Nieto, 1965]

$$P_m^{(n)} = \bar{n}^{|n-m|}e^{-\bar{n}}\frac{n_<!}{n_>!}(L_{n_<}^{|n-m|}(\bar{n}))^2, \tag{7.9}$$

where $\bar{n} = |\alpha_d|^2$, $n_<$ ($n_>$) is the lesser (greater) of the integers n and m and $L_n^a(x)$ is a generalized Laguerre polynomial.

In our experiments, the harmonic oscillator motion is coupled by laser fields to a two-level system with states labelled $|\downarrow\rangle$ and $|\uparrow\rangle$ with energy difference $E_\uparrow - E_\downarrow = \hbar\omega_{\downarrow\uparrow} > 0$. The

internal state is initialized in $|\downarrow\rangle$ by optical pumping. After the state of motion is prepared, the state $|\downarrow\rangle|\Psi(t)\rangle$ can be driven on a red sideband, resulting in population transfer $|\downarrow\rangle|m\rangle \leftrightarrow |\uparrow\rangle|m-1\rangle$ for all $m > 0$ while the state $|\downarrow\rangle|0\rangle$ is unaffected [Leibfried et al., 2003]. The Rabi frequencies depend on $m > 0$ as

$$\Omega_{m,m-1} = \Omega_0 e^{-\eta^2/2} \eta \sqrt{\frac{1}{m}} L_{m-1}^1(\eta^2), \tag{7.10}$$

where Ω_0 is the Rabi frequency of a carrier transition $|\downarrow\rangle \leftrightarrow |\uparrow\rangle$ of an atom at rest, $\eta = k_z z_0$ is the Lamb-Dicke parameter, with k_z the component of the effective wavevector along the direction of oscillation. After driving the red sideband of state $|\downarrow\rangle|\Psi(t)\rangle$ (where the state prior to displacement is $|\Psi(0)\rangle = |n\rangle$) for duration τ, the probability of having flipped the internal state to $|\uparrow\rangle$ is

$$P_\uparrow(\tau) = \frac{1}{2}\left[1 - P_0^{(n)} - \sum_{m=1}^{\infty} P_m^{(n)} \cos(2\Omega_{m.m-1}\tau)\right]. \tag{7.11}$$

We set the red sideband drive duration to be equivalent to a resonant π-pulse on the $|\downarrow\rangle|1\rangle \leftrightarrow |\uparrow\rangle|0\rangle$ transition, which implies $2\Omega_{1,0}\tau = \pi$. For an arbitrary displaced number state the probability of the ion to be in $|\uparrow\rangle$ for this pulse duration becomes

$$P_\uparrow^\pi = \frac{1}{2}\left[1 - P_0^{(n)} - \sum_{m=1}^{\infty} P_m^{(n)} \cos(\pi \frac{\Omega_{m.m-1}}{\Omega_{1,0}})\right]. \tag{7.12}$$

This probability is not a monotonic function of $\bar{n}$ and exhibits maxima and minima as the displacement changes. Experimental observations of this behavior for displaced number states and comparisons to the predictions of Eq. (7.12) will be discussed in section 7.4.2. When the detuning in Eq. (7.7) is $\delta \neq 0$, the coherent drive displaces $|\Psi(0)\rangle$ along circular trajectories in phase space that can turn back onto themselves. For $\delta\ t = m\pi$ with m a non-zero integer, $|\alpha(t)|$ will reach a maximum of $2\Omega_z/\delta$ for m odd and return to zero for m even. The non-monotonic behavior of $P_\uparrow^\pi$ with respect to $\bar{n}$ creates feature-rich lineshapes when this probability is probed as a function of the displacement detuning δ relative to the harmonic oscillator frequency.

7.3 Noise sensing with motion-echo sequences

The motion displacements discussed above enable sensitive tests of the ion's motional coherence. Electric field amplitude noise that overlaps with the motional frequencies heats the ion out of the ground state, and is observed in all traps at a level that often exceeds resistive heating by orders of magnitude. This "anomalous heating," is well documented [Turchette et al., 2000; Brownnutt et al., 2015; Talukdar et al., 2016], but the sources are not well understood. On much longer time scales than the ion-oscillation period, motional frequencies are known to drift over minutes and hours due to various causes, for example slow changes in stray electric fields and drifts of the sources that provide the potentials applied to the trap electrodes (see also Sec. 6.4). Much less work has been done to characterize noise in the frequency range in between the harmonic oscillator frequency and slow drift [Talukdar et al., 2016]. The high Q of most trapped-ion systems implies that this lower frequency noise contributes negligibly to heating, but does cause dephasing of the ion's motional state that can be detected with coherent displacements. Here, we construct sequences of coherent displacements that alternate with periods of free evolution and suppress the sensitivity to slow drifts of the harmonic oscillator frequency. This allows us to isolate harmonic oscillator frequency noise in a specific frequency band, in analogy to an AC-coupled electronic spectrum analyzer. This method is suitable for detecting noise at frequencies in a range of 500 Hz to 400 kHz in the experiments described here. Measurements at lower frequencies are in part limited by the heating rate of the system, while the highest noise frequencies we can characterize are determined by the duration of coherent displacements, which in our system can be implemented on time scales of order a few μs.

7.3.1 Basic principle

The sequences of coherent displacements discussed here are closely related to spin-echo experiments and dynamical decoupling in two-level systems [Hahn, 1950; Ernst et al., 1987; Álvarez and Suter, 2011]. In analogy to the classic

$$(\pi/2\text{-pulse})\text{-}\tau_a\text{-}(\pi\text{-pulse})\text{-}\tau_a\text{-}(\pi/2\text{-pulse})$$

spin-echo sequence [Hahn, 1950] with τ_a the duration of a free-precession period, the ideal "motion-echo"pulse sequence consists of

$$\hat{D}(\Omega_z\tau_d/2)\text{-}\tau_a\text{-}\hat{D}(-\Omega_z\tau_d)\text{-}\tau_a\text{-}\hat{D}(\Omega_z\tau_d/2),$$

where τ_d characterizes the duration of the displacement and the minus sign in the argument of the second displacement indicates that the phase ϕ of the displacement drive has changed by π relative to the other displacement operations. To simplify this initial discussion, we assume that all displacements are instantaneous and not affected by fluctuations in the oscillator frequency. This condition is similar to the "hard-pulse" limit for spin-echo sequences. If the frequency of the oscillating electric field in Eq. (7.1), which we call the "local oscillator frequency" in this context, is on resonance with the harmonic oscillator frequency, the displacements in the sequence add up to zero, so any initial state is displaced back onto itself at the end of the sequence (see Fig. 7.1 (a)). In analogy to a spin-echo sequence, if the local oscillator differs from the harmonic oscillator frequency by a small, constant detuning $\delta \ll 2\pi/\tau_d$, the sequence will still result in a final state that is very close to the initial state (see Fig. 7.1 (b)). However, if the detuning changes sign between free-precession periods (see Fig. 7.1 (c)), the final state will not return to the initial position and in general information about the oscillator frequency fluctuations can be gained from the final displacement. This basic echo sequence can be expanded by including additional blocks of the form

$$\tau_a\text{-}\hat{D}(\Omega_z\tau_d)\text{-}\tau_a\text{-}\hat{D}(-\Omega_z\tau_d)$$

after the first displacement $\hat{D}(-\Omega_z\tau_d)$ in analogy to dynamical decoupling sequences in two-level systems. Ideally, this increases the number of free-precession sampling windows which

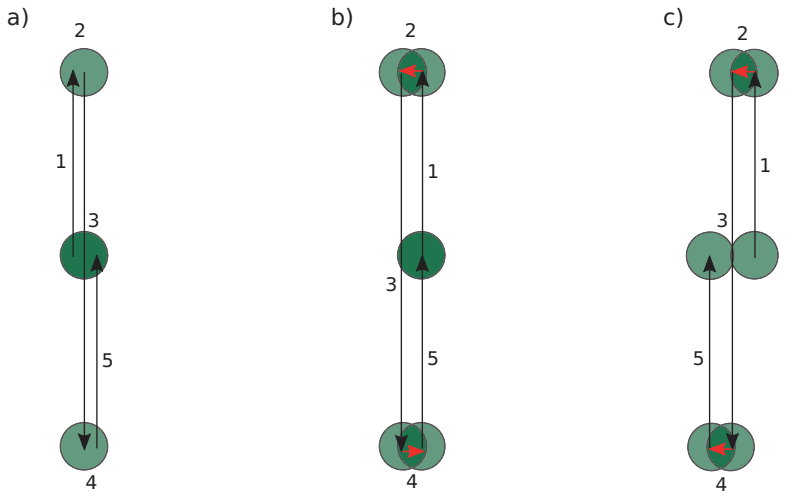

Figure 7.1: Schematic phase-space sketch of the displacements in the simplest motion-echo sequence. Here, all displacements are assumed to act instantaneously (hard-pulse limit), such that the effect of oscillator detuning during displacements can be neglected. (a) Without fluctuations of the oscillator frequency, the ground-state minimum uncertainty disk (green) is coherently displaced by $\Omega_z \tau_d/2$ (step 1), then remains stationary during a free-precession period (step 2), it is then displaced symmetrically through the origin by $-\Omega_z \tau_d$ (step 3), followed by another free-precession period (step 4). The final displacement by $\Omega_z \tau_d/2$ (step 5) returns the state to the origin. (b) With a small, constant detuning, the state drifts perpendicular to the direction of the first displacement in step 2. However, it drifts an equal amount in the opposite direction during step 4, to therefore return to the ground state after step 5. This immunity to constant detuning can be thought of as a harmonic oscillator analogy to a spin-echo sequence in a spin-1/2 system. (c) If the detuning changes sign between steps 2 and 4, the state does not return to the origin. In all three cases (a)-(c), the final state reflects the sum of additional displacements during the operation of the sequence that are caused by time-dependent changes in harmonic oscillator detuning.

leads to a longer sampling time and narrower filter bandwidth of the extended sequence, while still producing no net displacement from the initial state if the harmonic oscillator is stable, even if the local oscillator is slightly detuned from the harmonic oscillator resonance.

7.3.2 Effects of oscillator frequency fluctuations

If the local oscillator frequency is not on resonance with the harmonic oscillator frequency, or if the detuning is not constant in time, a realistic coherent drive (not assuming the hard-pulse limit) will not always displace the state of motion along a straight line. To model this situation, we define ω_0 to be the time-independent frequency at which the interaction frame with respect to H_0 rotates and set this to be equal to the local oscillator frequency and $\omega_0 = \omega - \delta(t)$. The differential equation describing the coherent displacement $\alpha(t)$ as a function of time becomes

$$\dot{\alpha}(t) = \alpha i\delta(t) - i\Omega_z e^{-i\phi}, \tag{7.13}$$

where $\delta(t)$ is the instantaneous detuning between the harmonic oscillator and the local oscillator at time t. In the special case where δ does not depend on time and $\alpha(0) = 0$, the solution is consistent with $\alpha(t)$ from Eq. (7.6) after taking the change of reference frame into account. If there is noise on the trap frequency, $\delta(t)$ will fluctuate randomly as a function of t. A general solution of Eq. (7.13), at time $t_0 + \tau$ as it evolves from the initial state $\alpha(t_0)$ at time t_0, can be formally written as

$$\alpha(t_0, \tau) = \exp[iI_1(t_0, \tau)][\alpha(t_0) - i\Omega_z e^{-i\phi} I_2(t_0, \tau)], \tag{7.14}$$

with

$$\begin{aligned} I_1(t_0, \tau) &= \int_{t_0}^{t_0+\tau} \delta(\tau_1) d\tau_1, \\ I_2(t_0, \tau) &= \int_{t_0}^{t_0+\tau} \exp\left[-i \int_{t_0}^{\tau_2} \delta(\tau_1) d\tau_1\right] d\tau_2. \end{aligned} \tag{7.15}$$

This form is useful for numerical calculations and can be explicitly solved for special cases of $\delta(t)$. Motion-echo sequences are most useful if the accumulation of phase during τ is small, $I_1(t_0,\tau) \ll 2\pi$. In such cases, we can expand the exponential functions in Eqs. (7.14) and (7.15) to linear order and make the approximation

$$\begin{aligned} \alpha(t_0,\tau) &\simeq \{\alpha(t_0) - i\Omega_z\tau e^{-i\phi}\} + i(\alpha(t_0) - i\Omega_z\tau e^{-i\phi})I_1(t_0,\tau) \\ &\quad -\Omega_z e^{-i\phi} I_3(t_0,\tau), \\ I_3(t_0,\tau) &= \int_{t_0}^{t_0+\tau} \left(\int_{t_0}^{\tau_2} \delta(\tau_1) d\tau_1 \right) d\tau_2. \end{aligned} \tag{7.16}$$

The different terms in Eq. (7.16) have straightforward interpretations: the term in curly braces characterizes the displaced coherent state for no detuning, $\delta(t) = 0$. Finite detuning rotates this state around the origin in phase space and to lowest order this effect is captured by the term proportional to $I_1(t_0,\tau)$. The final term reflects the effect of the detuning during displacement, which results in a correction proportional to $I_3(t_0,\tau)$. For a free-precession period, $\Omega_z = 0$; during displacement, $\Omega_z \neq 0$.

In this linear approximation, it is straightforward to keep track of the displacements and the corrections from $\delta(t) \neq 0$ when periods of driving and free precession are concatenated. Because corrections on earlier corrections are higher order than linear, the correction from each period only acts on the zero-order displacement of any previous period. This implies that the zero-order terms in curly brackets and the corrections can be summed up separately for a sequence. In this way, we can calculate the total zero-order displacement α_n and first order correction $\Delta\alpha_n$ of a sequence with n steps starting at time $t = 0$ in state $|\alpha(0)\rangle$. For the k-th step starting at t_k, the displacement drive Rabi frequency is $\Omega_{z,k}$, the drive duration τ_k, and the phase ϕ_k. In the linear approximation with $\alpha(0) = \alpha_0$ the sums are

$$\alpha_n = \alpha_0 - i\sum_{k=1}^{n} \Omega_{z,k}\tau_k e^{-i\phi_k}, \tag{7.17}$$

$$\Delta\alpha_n = i\sum_{k=1}^{n} \left\{ \left(\alpha_{k-1} - i\Omega_{z,k}\tau_k e^{-i\phi_k}\right) I_1(t_k,\tau_k) - \Omega_{z,k} e^{-i\phi_k} I_3(t_k,\tau_k) \right\}. \tag{7.18}$$

7.3.3 Motion-echo sequences

We restrict ourselves to sequences with N steps acting on an initial ground state, $\alpha_0 = 0$, where the sum over all unperturbed displacements of a sequence is $\alpha_N = 0$. In this way, the actual final state is equal to $|\Delta\alpha_N\rangle$ and directly reflects the effects of non-zero detuning. Moreover, we can construct the displacements in such a way, that a constant detuning $\delta \neq 0$, results in $\Delta\alpha_N = 0$. This mimics the feature of spin-echo sequences that small constant detunings have no effect on their final spin state. The motion-echo sequences preserve this feature, if the linear approximation is valid, even when taking the effect of the detuning of the displacement operations into account. For constant δ, the integrals $I_1(t_k, \tau_k) = \delta\tau_k$ and $I_3(t_k, \tau_k) = 1/2\ \delta\tau_k^2$ are independent of t_k and the total displacement simplifies to

$$\Delta\alpha_N = i\delta \sum_{k=1}^{N} \tau_k(\alpha_{k-1} + i/2\ \Omega_{z,k} e^{-i\phi_k}\tau_k). \tag{7.19}$$

For the motion-echo sequences, $\Omega_{z,k} = \Omega_z$ is the same for all displacements and the coherent state parameter before each of the $\hat{D}(\pm\Omega_z\tau_d)$ operations is $\mp\Omega_z\tau_d/2$. In this case, the second contribution in the (...) braces is $\pm 1/2\Omega_z\tau_d$, equal and opposite to the initial state parameter, so all displacement terms in the sum Eq. (7.19) are equal to zero individually, except for the first and last displacement which is $\hat{D}(\Omega_z\tau_d/2)$. However, since $\alpha_0 = 0$, these terms sum to $i\delta\tau_d/2(1/2\Omega_z\tau_d/2 - \Omega_z\tau_d/2 + 1/2\Omega_z\tau_d/2) = 0$, which leaves only the free-precession terms to be considered. All sequences contain an even number $2n_a$ of free-precession periods ($n_a > 0$, integer), with half of them contributing $i\delta\tau_a\Omega_z\tau_d/2$ each and the other half $-i\delta\tau_a\Omega_z\tau_d/2$, so, as previously noted (see Fig. 7.1) these terms also sum to zero and $\Delta\alpha_N = 0$ for a constant detuning.

7.3.4 Response to a monochromatic modulation

Next, we can determine the response to a monochromatic modulation at frequency ω_n of the form $\delta_n(t) = A_n \cos(\omega_n t + \phi_n)$. On the one hand, the harmonic oscillator frequency can be deliberately modulated in this way, which enables us to compare the response of the motion-echo sequence to the theoretical expectation. On the other hand, some of the frequency noise acting on the oscillator can be characterized as a noise spectrum consisting of a sum of such modulation terms with distinct frequencies $\omega_{n,j}$, generally varying amplitudes $A_{n,j}$ and random phases $\phi_{n,j}$. In addition, the harmonic oscillator may be affected by noise with a continuous spectrum, but we will restrict ourselves to discrete, narrow-band noise spurs here. The noise spectrum can be characterized with motion-echo sequences, if the response to a monochromatic modulation at ω_n allows for determination of that frequency within a band that depends on the resolution of the sequence. The amplitude of the response $\Delta\alpha_N$ is proportional to the noise amplitude and is zero when averaged over the random noise phase ϕ_n (denoted by $\langle ... \rangle$), but because the final occupation $\bar{n}_{\mathrm{fin}}$ is proportional to $|\alpha_N|^2$, after integrating over ϕ_n, we get an average final occupation

$$\langle \bar{n}_{\mathrm{fin}} \rangle = \frac{1}{2\pi} \int_0^{2\pi} |\Delta\alpha_N|^2 d\phi_n. \tag{7.20}$$

This is proportional to the noise power (proportional to A_n^2) inside the filter bandwidth of the motion-echo.

For the monochromatic modulation, the integrals I_1 and I_3 have analytic solutions:

$$\begin{aligned} I_1(t_0,\tau) &= \frac{A_n}{\omega_n}[\sin(\omega_n(t_0+\tau)+\phi_n) - \sin(\omega_n t_0 + \phi_n)] \\ I_3(t_0,\tau) &= \frac{A_n}{\omega_n^2}[\cos(\omega_n t_0 + \phi_n) - \cos(\omega_n(t_0+\tau)+\phi_n) - \\ &\quad -\omega_n \tau \sin(\omega_n t_0 + \phi_n)]. \end{aligned} \tag{7.21}$$

The integrals depend on t_0 and τ, therefore the sum over a motion-echo sequence is non-zero in general. Inserting the integrals into Eq. (7.17) and summing over the motion-

echo sequences is tedious but straightforward, and yields closed expressions for the final displacement $\Delta\alpha_N$ and the corresponding average occupation number of the motion $\bar{n}_{\rm fin} = |\Delta\alpha_N|^2$. Taking the average over the random phase ϕ_n yields

$$\begin{aligned}\langle\bar{n}_{\rm fin}\rangle &= \frac{8A_n^2\Omega_z^2}{\omega_n^4}\sin^2[\omega_n\tau_d/4]\{\cos[\omega_n\tau_d/4]-\cos[\omega_n(\tau_a+3\tau_d/4)]\}^2\times \\ &\quad\times\frac{\sin^2[n_{\rm a}\omega_n(\tau_d+\tau_a)]}{\sin^2[\omega_n(\tau_d+\tau_a)]}. \end{aligned} \tag{7.22}$$

If the free-evolution time τ_a is varied in the motion-echo sequence, the expression in the upper line produces an envelope that is oscillating at frequency ω_n with phase shifts proportional to τ_d.[1] The first main peak appears when $\omega_n(\tau_d+\tau_a) \simeq \pi$ and the spacing between adjacent main peaks is exactly $\Delta\tau_a = 2\pi/\omega_n$, which allows for determination of ω_n from this interference pattern. The width of the narrow main peaks can be characterized by the distance $\delta\tau_a$ of the two zeros of the response closest to a peak, which are spaced by $\delta\tau_a = 2\pi/(n_a\omega_n)$. It is possible to resolve a pair of main peaks produced by modulations at ω_n and $\omega_n+\delta\omega_n$ respectively, as separate maxima if $|\delta\omega_n| \geq \pi/[n_a(\tau_a+\tau_d)]$. If a continuous noise power spectral density $a_n^2(\omega_n)$ is sampled in this way, $\delta\omega_n$ determines the bandwidth of the sample filter that relates the noise power density to the actual noise power detected in this band.

To have $\langle\bar{n}_{\rm fin}\rangle$ approximately represented by the ion state population $P_\uparrow^\pi$, the average mode occupation should be kept below $\langle\bar{n}_{\rm fin}\rangle \leq 1$, which is possible by reasonable choices for the displacement $\Omega_z\tau_d$ and the number of free-precession periods $2n_a$. Choosing either the size of the displacement or the number of displacements to be too large has the same effect as over-driving the mixer in an electronic spectrum analyzer, which leads to a response that is not linear in the input signal, resulting in a distorted output.

[1] The expression in the lower line is equivalent to the intensity far-field pattern of a transmission grating with n_a slits [Born and Wolf, 1980] and describes a n_a-times sharper response that produces a more narrowly peaked interference pattern with nearly symmetric side lobes.

7.4 Experimental implementation and results

7.4.1 Experimental setup

Experiments are performed with the linear surface-electrode trap described in Sec. 4.1.1. The coherent displacements are performed on the axial mode, with frequency $\omega_z \simeq 2\pi \times 8$ MHz. Direct "carrier"-transitions between the states $|\downarrow\rangle|n\rangle$ and $|\uparrow\rangle|n\rangle$ are driven by microwave fields induced by a $\omega_0 \simeq 2\pi \times 1.281$ GHz current through electrode DC1 (Fig. 4.2).

The ion is prepared in $|\downarrow\rangle|0\rangle$ with a fidelity exceeding 0.99 by Doppler laser cooling, followed by ground-state cooling and optical pumping. Sideband transitions $|\downarrow\rangle|n\rangle \leftrightarrow |\uparrow\rangle|n \pm 1\rangle$ are implemented with stimulated Raman transitions driven by two counter-propagating laser beams. This allows us to prepare nearly pure number states of the motion as described in more detail in [McCormick et al., 2019a] and Ch. 5. We implement the tickle as described in Sec. 4.2.8 and distinguish measurements of the $|\uparrow\rangle$ and $|\downarrow\rangle$ states with state-dependent fluorescence (see Sec. 4.8.4).

In the experiments detailed below, the signal indicates the deviation of the final motional state from $|n = 0\rangle$. Population in the ground state of motion is discriminated from that in excited states of motion by performing the RSB pulse theoretically described in Sec. 4.8.5 and Eq. (7.12), connecting population in $|\downarrow\rangle|n > 0\rangle$ to $|\uparrow\rangle|n - 1\rangle$ while leaving population in $|\downarrow\rangle|n = 0\rangle$ unchanged. For average excitation $\bar{n} \leq 1/2$ the probability $P_{\uparrow}^{\pi}$ of changing the internal state is approximately equal to $\bar{n}$. A subsequent microwave carrier π-pulse exchanges population in $|\downarrow\rangle$ and $|\uparrow\rangle$ followed by detection. The $|\uparrow\rangle$ state has a low average count rate, which minimizes shot noise in the photomultiplier signal. This is helpful when determining small deviations from $|n = 0\rangle$ with high signal-to-noise ratio.

7.4.2 Displaced number states

As briefly described in [Home et al., 2011], tickling an ion that has been cooled to near the motional ground state to determine the ion oscillation frequency is a practical calibration tool. The experiment is performed as follows: the ion is cooled to near the ground state and prepared in $|\downarrow\rangle$, then a tickle tone with a fixed amplitude and detuning δ is applied for a fixed duration $\tau_d = 13$ μs. The resulting coherent state is characterized by applying a RSB π-pulse for the $|\downarrow\rangle|1\rangle \rightarrow |\uparrow\rangle|0\rangle$ transition followed by a microwave carrier π-pulse, then detection of the internal state via state-selective fluorescence as described above.

The symbols with error bars (1-σ statistical error, from shot noise in the photo-multiplier counts averaged over 600 experiments per detuning value) in Fig. 7.2 show the measured $P_{\downarrow}^{\pi}$ as a function of tickle detuning for low on-resonance occupation ($\bar{n} = 0.61(1)$). The line shape is well described by Eqs. (7.7) and (7.12). The solid line is a fit to these equations with $\bar{n} = 0.61(1)$ as the only free parameter after subtracting an offset of 0.05(1) due to stray light background and imperfect ground state cooling that was determined independently. In this case, $P_{\downarrow}^{\pi}$ is roughly linear in $\bar{n}$ and reflects the sinc^2-shape of the Fourier transform of the square-envelope tickle pulse. Keeping the excitation small gives us the practical advantage that only one prominent peak in $P_{\downarrow}^{\pi}$ versus detuning exists, making fitting to find the resonance frequency straightforward. However, the precision with which we can determine the frequency of oscillation is Fourier-limited by the pulse duration.

With the development of a theoretical understanding of line shapes for larger displacements, where $P_{\downarrow}^{\pi}$ is non-linear in $\bar{n}$, we have found that we can determine the resonant frequency with a precision that increases approximately linearly with the size of the excitation $|\alpha|$ in the range of $0 < |\alpha| < 17$, which implies that we can improve on the Fourier limit of the

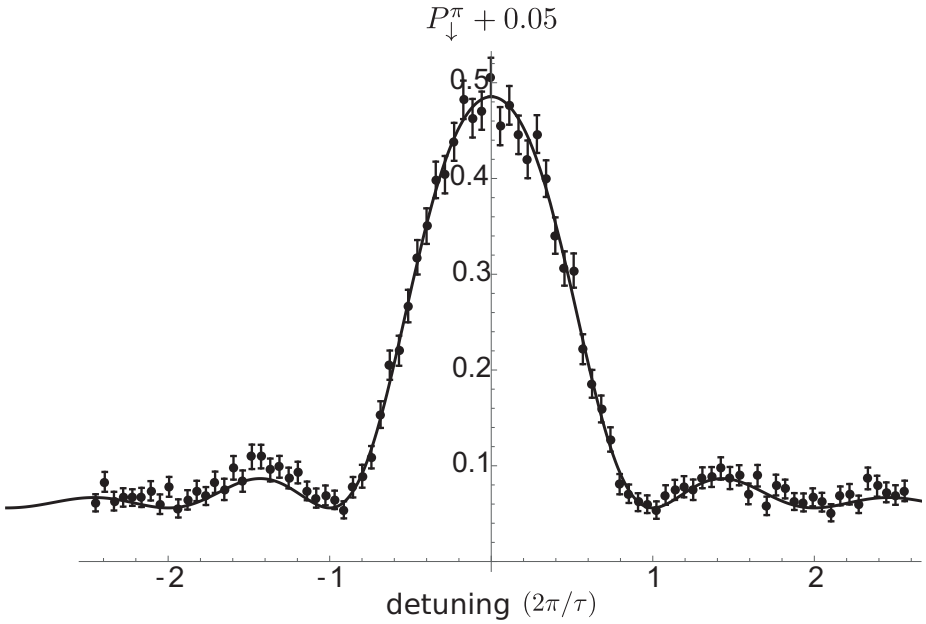

Figure 7.2: Spin-flip probability $P_{\downarrow}^{\pi}$ (See Sec. 4.2) of ion after 13 μs tickle excitation on $|\downarrow\rangle$ versus detuning from ion oscillation frequency. The average occupation $\bar{n}$ of the ion motion in response to tickle excitation is mapped onto the spin state by applying a RSB pulse, which connects levels $|\downarrow\rangle|n\rangle$ to $|\uparrow\rangle|n-1\rangle$ for $n > 0$, while leaving population in $|\downarrow\rangle|n = 0\rangle$ unchanged. A subsequent microwave carrier π-pulse exchanges populations in $|\uparrow\rangle$ and $|\downarrow\rangle$ to reduce measurement projection noise. The solid line is a fit using Eq. (7.7), free parameter $\bar{n}$, and an experimentally determined vertical offset of 0.05(1) added to account for background counts and imperfect ground state cooling. The fit yields an on resonance average occupation of $\bar{n} = 0.61(1)$.

tickle pulse. We expect that the linear trend continues beyond $|\alpha| = 17$, but anharmonicity and trap stability will limit the useful range of $|\alpha|$.

We have measured $P_{\downarrow}^{\pi}$ (given by Eq. 7.12 following the microwave carrier π-pulse to exchange population between $|\downarrow\rangle$ and $|\uparrow\rangle$) versus detuning of the tickle frequency for various displacement amplitudes up to $|\alpha| \approx 17$, corresponding to a coherent state with an average occupation of $\bar{n} \approx 300$. Fig. 7.3 shows four such cases with $\bar{n}$ of 3.22(3) (Fig. 7.3a), 10.4(1) (Fig. 7.3b), 98.4(7) (Fig. 7.3c) and 299(1) (Fig. 7.3d). The lines are fits with free parameters Ω_z and harmonic oscillator resonance frequency ω_0. An experimentally determined vertical offset of 0.05(1) is added to the fit function to account for background counts, as in the evaluation of the data presented in Fig. 7.2.

The steep slopes of some of the line-shape features imply a stronger response to small changes in the detuning, as compared to cases where $\bar{n} \leq 1$ (dashed lines in Fig. 7.3). Moreover, the response is symmetric around $\delta = 0$, so these steeper slopes can be exploited to find $\delta = 0$ without a detailed understanding of the line shapes beyond this symmetry. This enables line-center determination with a signal-to-noise ratio beyond the Fourier limit of the linear response ($\bar{n} \leq 1$).

To validate the generalization of our theory to displaced number states with quantum numbers $n \geq 1$ (see Eq. 7.9), we produce number states up to $n = 6$, as described in Ch. 5 and [McCormick et al., 2019a] and scan the amplitude of the coherent displacement while the tickle frequency is resonant with the ion's oscillation (see also [Ziesel et al., 2013] for earlier experiments on displaced number states with n up to 3). As the amplitude of the coherent state increases, the Rabi frequency of the RSB interaction varies with n as predicted by Eqs. (7.10) and (7.12), producing the non-monotonic response of the ion's fluorescence shown in Fig. 7.4 together with fits based on Eq. (7.12), with the tickle strength Ω_z and contrast of

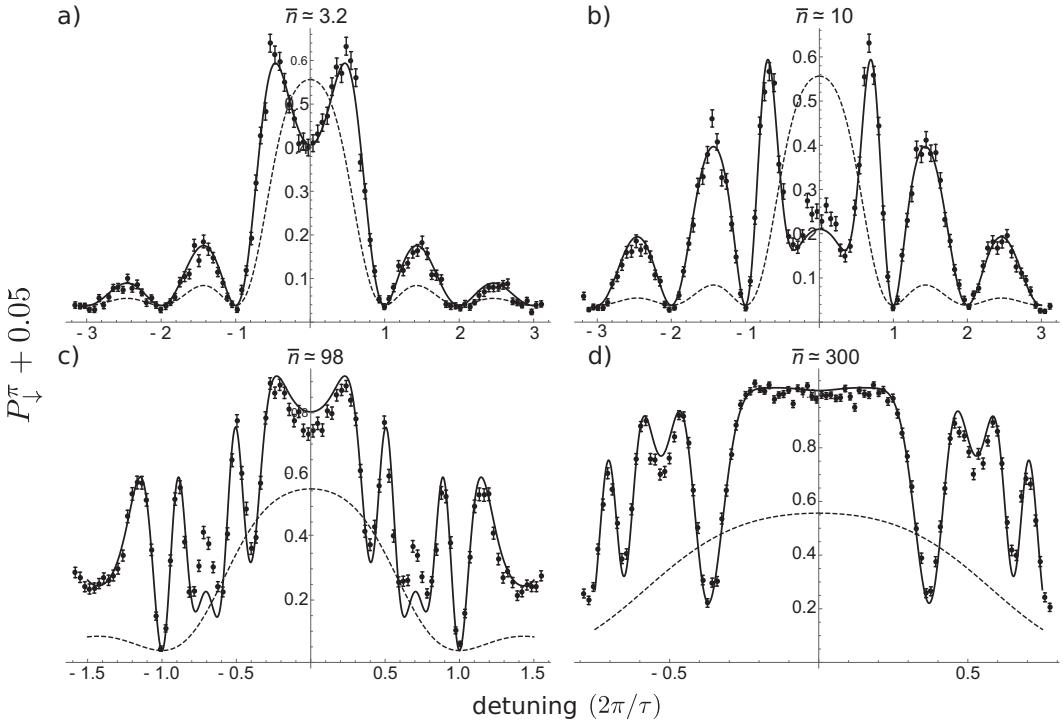

Figure 7.3: Response of ion to tickle excitation versus detuning from the ion oscillation frequency for maximal excitations on resonance of a) $\bar{n} = 3.22(3)$, b) $\bar{n} = 10.4(1)$, c) $\bar{n} = 98.4(7)$ and d) $\bar{n} = 299(1)$. As the average occupation of the coherent state increases, the line shape becomes more sharply featured. Solid lines are fits with free parameters Ω_z and ω_z. We determine the maximum excitation $\bar{n}$ of each experiment from the fitted values of Ω_z. Dashed lines represent a Fourier-limited response resulting from a weaker excitation ($\bar{n} = 0.64$) for comparison.

the final state readout as free parameters. We perform this experiment by preparing the ion in pure number states $n = 0$ (Fig. 7.4 a)), $n = 2$ (Fig. 7.4 b)), $n = 4$ (Fig. 7.4 c)) and $n = 6$ ((Fig. 7.4 d)) and applying a resonant tickle tone with fixed Ω_z for durations ranging from 0.05 to 12 μs, resulting in coherent displacements up to $|\alpha_d| \approx 20$. Displaced number states are useful to quantum-enhanced sensing of forces with high number states [Wolf et al., 2018].

7.4.3 Motion-echo experiments

We first perform the motion-echo experiments with a 10 kHz or 100 kHz tone applied to one of the trap electrodes. The tone modulates the potential curvature of the trap at the position of the ion and therefore the ion's oscillation frequency. The purpose of this is two-fold: To experimentally characterize the response of the ion and compare the results against theory for a known perturbation and to explore the range of noise that is detectable with this method in our setup. With the tone applied continuously and the phase ϕ_n changing randomly from experiment to experiment (to mimic the uncontrolled phase of noise), we perform a series of motion-echo sequences with various numbers of free-precession periods $2n_a$, scanning the wait time τ_a. We find that $P_{\downarrow}^{\pi}$ depends on the relationship between τ_a and the frequency of the applied tone in the expected manner according to Eq. (7.22). This can be seen by comparing the measured points in Fig. 7.5 to the solid lines that show fits with A_n as a free parameter. All fitted values of A_n are consistent with each other to within 2 times the standard deviation (see caption of Fig. 7.5) and indicate a relative modulation depth of $A_n/\omega_0 \simeq 1.4 \times 10^{-4}$. Similar experiments were performed with applied tones from 500 Hz to 400 kHz and while the results qualitatively agreed with theory, attenuation and distortion of the tones through various filters with uncharacterized parasitic capacitance and resistive loss at 4 K in our experimental setup prevented us from comparing quantitatively to the theory.

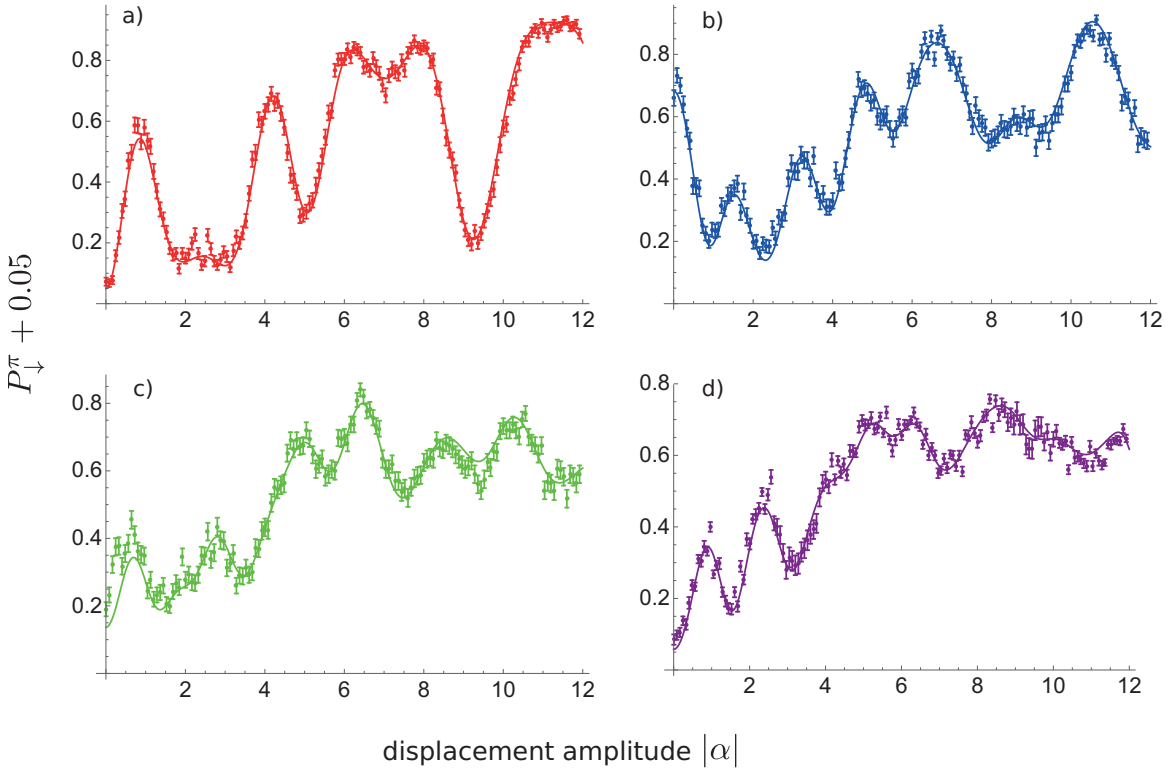

Figure 7.4: Response of ion to tickle excitation versus coherent drive duration for initial number states a) $n = 0$, b) $n = 2$, c) $n = 4$ and d) $n = 6$. As the displacement of the ion's motion increases, the Rabi frequency of the RSB interaction varies non-monotonically. Solid lines are produced with theory in Eq. (7.12) using fit parameters of the tickle strength Ω_z and contrast of the final state readout, and an experimentally determined vertical offset of 0.05(1) to account for background counts and imperfect initial state preparation. Fitted values of Ω_z and the contrast of the final state are, respectively, a) $2\pi\times$ 0.2300(2) MHz and 0.884(4), b) $2\pi\times$ 0.2453(3) MHz and 0.899(5), c) $2\pi\times$ 0.2516(6) MHz and 0.886(6) and d) $2\pi\times$ 0.2558(8) MHz and 0.894(5).

Finally, we perform motion-echo experiments without a purposely applied tone, to sense and characterize intrinsic frequency noise in our setup. With $n_a = 10$ (20 free-precession periods), $\tau_d = 4$ μs, and coherent displacements $\Omega_z \tau_d/2 = 3.44(2)$, we find several peaks in the time scan corresponding to a single narrow-band noise spur at $\omega_n \simeq 2\pi\times$ 260 kHz having an amplitude $A_n = 2\pi \times 2.4(2)$ kHz (see Fig. 7.6a), which corresponds to a relative modulation depth $A_n/\omega_0 \simeq 3 \times 10^{-4}$. In this run, the electrode potentials are supplied from digital to analog converters (DACs), so the spurs are likely caused by cross-talk of digital circuitry in the DACs to the outputs. After switching the electrode potential sources to low-noise analog power supplies, we observed a nearly uniform noise floor without the spurs (see Fig. 7.6b).

In principle the sensitivity can be increased arbitrarily by choosing a larger value of the coherent drive strength (which is proportional to Ω_z, see Eq. (7.22)). However, there will be technical limitations that will depend largely on the setup. If noise on the coherent drive begins to dominate the outcome of an experiment, then the harmonic oscillator noise can no longer be accurately deduced. Even without any noise in the harmonic oscillator or the drive, anharmonicities will eventually deform the wave-packet and reduce the overlap of the final state with the ground state.

7.5 Discussion

Coherent displacements are a universal concept that applies to all harmonic oscillators and, because they correspond to a classical, near-resonant force on the oscillator, they can often be implemented in a simple way in concrete experimental settings. Here, we characterized the responses of a single, harmonically trapped atomic ion to an electric field that oscillates close to resonance with the ion's mechanical motion. The ion response was then

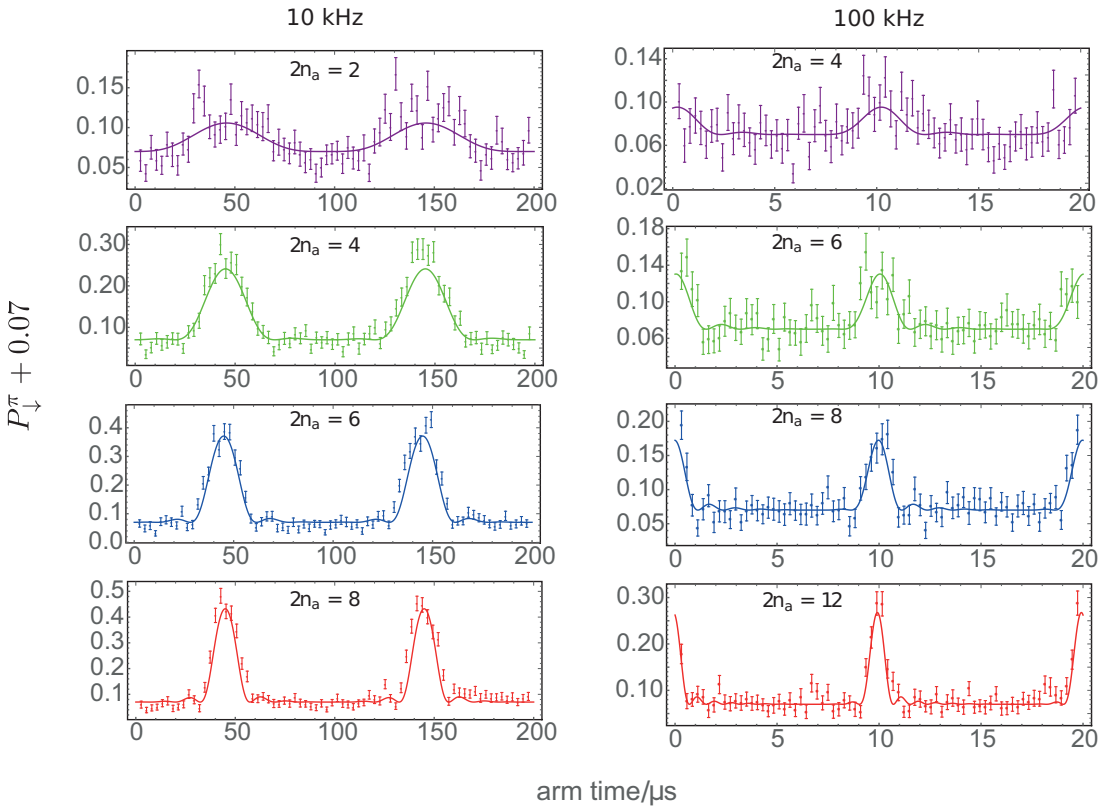

Figure 7.5: Characterization of motion-echo experiments with tones of 10 kHz and 100 kHz for various numbers of free-precession periods $2n_a$ (see top of plots). Lines are fits based on Eqs. (7.22) and (7.12) with free parameters A_n. For the experiments with the 10 kHz tone applied, fitted values of A_n were $2\pi\times$ 1.3(4) kHz, 1.5(1) kHz, 1.4(1) kHz and 1.2(1) kHz for $2n_a = 2$, 4, 6 and 8, respectively. Likewise for the 100 kHz tone, fitted values of A_n were $2\pi\times$ 1.0(4) kHz, 1.1(3) kHz, 1.1(2) kHz and 1.1(1) kHz for $2n_a = 4$, 6, 8 and 12, respectively.

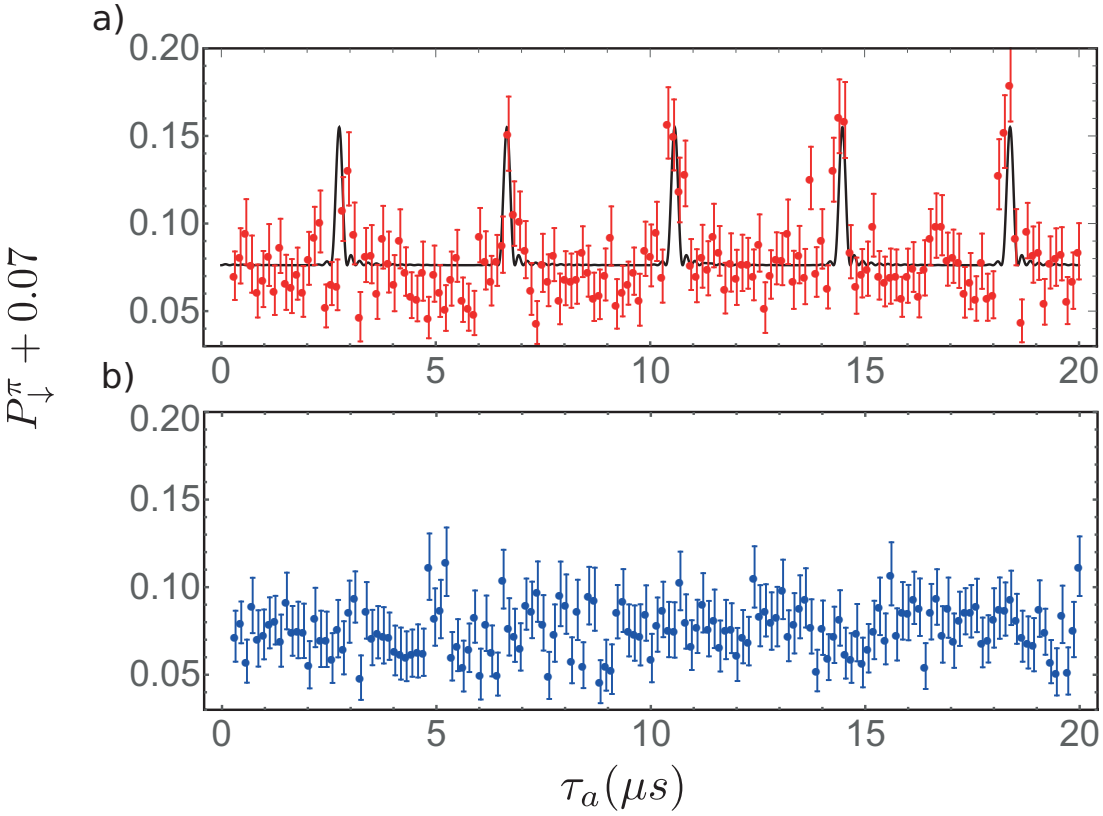

Figure 7.6: Noise sensing with motion-echo experiments. The two sub-plots compare noise on electrode potentials delivered from two different sources: a) Digital-to-Analog converters (DACs) and b) linear bench power supply. Experiments were performed with $n_a = 10$ (20 free-precession periods) and coherent displacements of $\Omega_z \tau_d/2 = 3.44(2)$. The solid black line in a) is a fit to the data taken using the DACs based on Eq. (7.22) with free parameters A_n and ω_n, and a vertical offset of 0.07 to account for background counts and imperfect state preparation. From this fit, we determine that the DACs introduce noise at $\omega_n/(2\pi) \simeq 260$ kHz with $A_n = 2\pi \times 2.4(2)$ kHz.

characterized by coupling the ion harmonic oscillator to an internal two-level system of the ion.

By applying a sequence of coherent displacements, alternating with free evolution of the state of motion, we obtained a frequency-filtered response of the harmonic oscillator. In this way, fluctuations of the harmonic oscillator frequency in a certain frequency band can be isolated and sensitively detected by the ion itself. This technique can be used as a complementary method in investigating the behavior of surface charges and answering questions about the sources of anomalous heating.

We anticipate that the basic concepts exhibited in the experiments described in this chapter can be transferred to other harmonic oscillator systems and foresee various extensions and refinements of the current trapped-ion work. For example, it should be possible to find interesting modifications of the coherent displacement sequences by utilizing different displacement patterns in phase space or by displacing non-classical quantum states [McCormick et al., 2019a; Wolf et al., 2018].

Chapter 8

Future directions: Coupled harmonic oscillators and experiments with multiple ions

One main motivation for studying the motion of a single trapped ion is for a better understanding of limitations of motional coherence in applications to quantum information processing. To this end, our next step is to apply the techniques discussed here with one ion to systems with two or three. The triangle trap has now replaced the double-well trap in our setup, which should allow us to trap three or more ions in separate, individually tunable wells in the future. An interesting first set of experiments would involve manipulating the coupling between the quantum motion in the different wells.

8.1 Previous attempt with triangle trap

Much of chapter 4 was spent describing updates to the apparatus in order to install the new triangle trap. We actually had previously installed an earlier version of the triangle trap in the setup for a brief period, had loaded ions in this trap, and were beginning preliminary characterization experiments. We were able to load in all three sites as well as a spurious trap in the center (see Fig. 8.1).

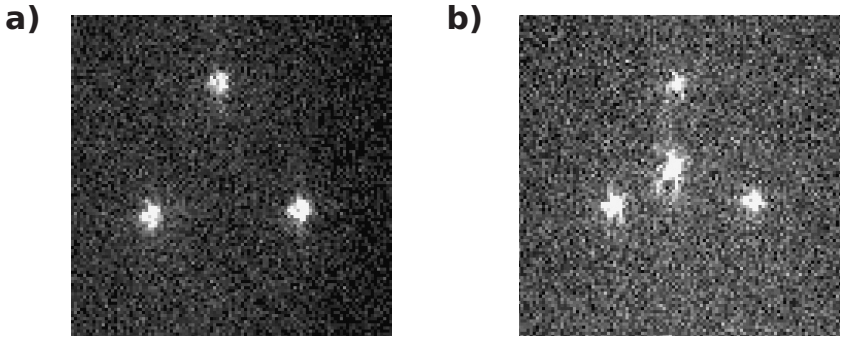

Figure 8.1: Images of a) 3 and b) 4 ions loaded in the triangle trap. The ion in the center in b) is loaded in a spurious trap that is located $\sim$10 μm out of the plane of the other ions, which is why it is slightly defocused.

8.1.1 Challenges

A major problem in controlling the ions in this triangle trap was that the DC electrode voltages necessary to compensate micromotion were much too large, particularly in the direction in the y_i directions (defined in Fig. 8.2). This is mainly due to the electrode geometry—there are very few electrodes near the ion that aren't symmetric about x_i, which means they will produce fields mainly in the x_i and z_i directions, but not the y_i directions (see Fig. 8.3).

Shortly after this discovery, the RF-electrode in the trap developed a short to ground and we were no longer able to trap ions. We suspect that a spike in the RF power shorted the RF electrode by some breakthrough mechanism. After this event, the resistance of the RF electrode to ground, which should nominally be infinite, was less than 10 Ω. Nevertheless, this short experience with the triangle trap inspired electrode geometry design changes that we think will make the new triangle trap more successful.

8.2 Design changes

There were a few main design changes made to the next generation triangle traps. First, the 20 μm triangle was abandoned—based on simulations, the ability to compensate stray fields in this was going to be even worse than in the 30 μm triangle, which was already marginal, given the upper limit of 20 V that can be applied to the DC electrodes. So, we now have two 30 μm traps, each with a slightly altered electrode geometry. One has the same number of electrodes as the previous design, but the shape of the electrodes underneath each ion is altered to provide more field in the y_i-direction for micromotion compensation (see Fig. 8.3). The alternative design mitigates this problem by changing the electrode geometry, and

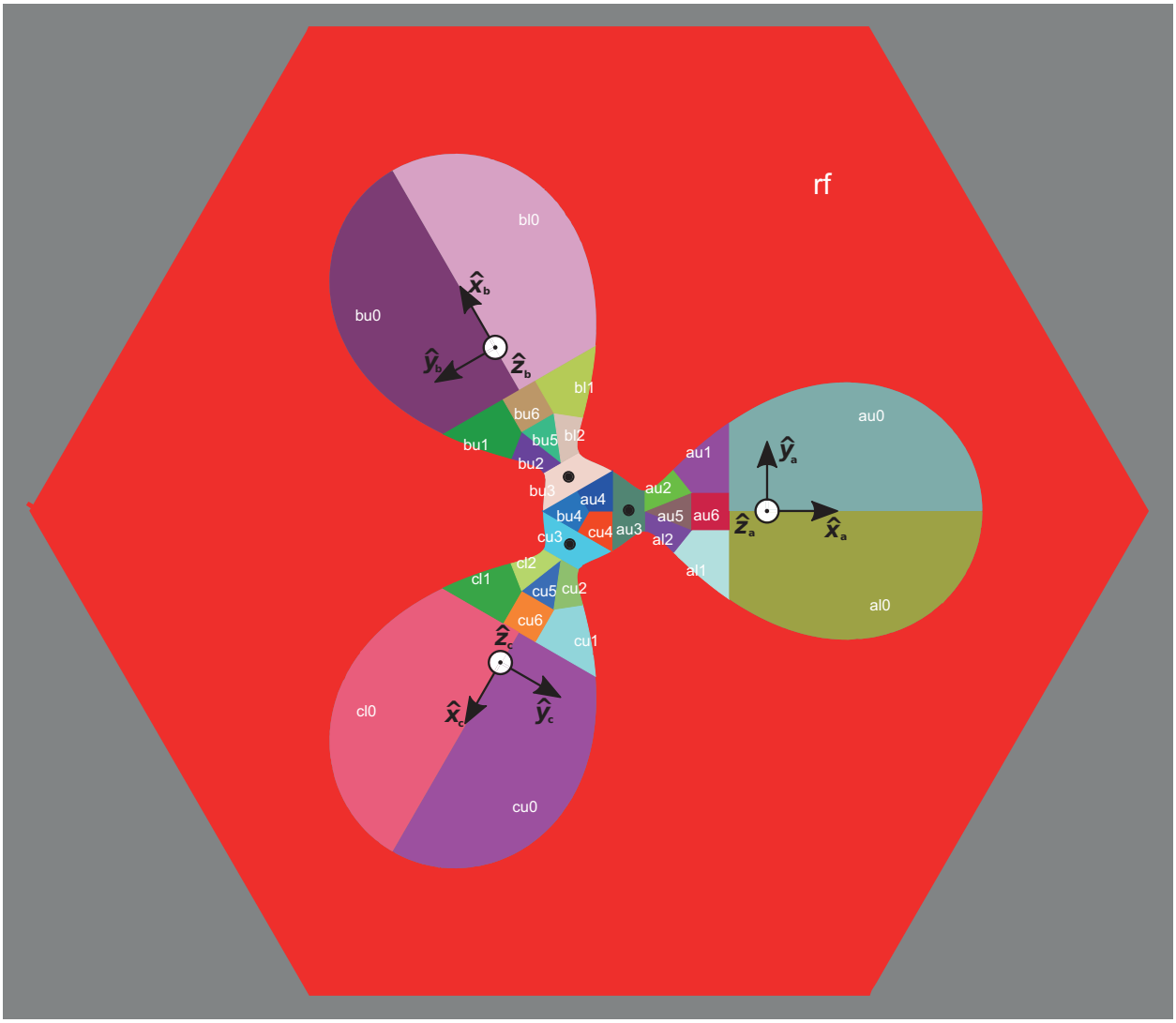

Figure 8.2: DC and RF electrodes of triangle trap used in previous experiments. Note the lack of electrodes near the trapping sites (black dots) which would produce a field in the y_i directions. This was intended to reduce the number of gaps between electrodes close to the ions but ended up as a major design flaw that hindered our ability to cancel stray fields in this direction.

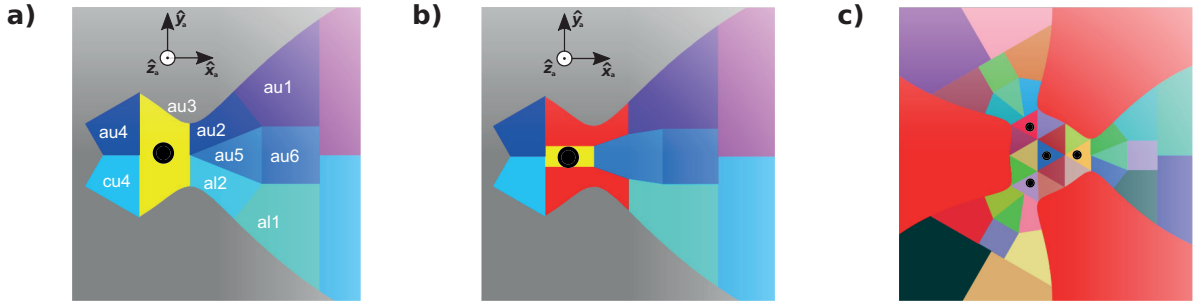

Figure 8.3: Triangle trap electrode redesigns. a) Original electrode geometry, zoomed in on one trapping site, b) new electrode geometry to provide more control over larger stray fields in the y-direction, c) second triangle electrode geometry, with more electrodes to control up to four ions, including one in the central spurious trap. Ion locations are represented by black dots.

also adds more electrodes to the center to allow us to tune the trapping parameters of the center spurious well, effectively becoming a "diamond" trap with four tunable trapping sites (see Fig. 8.3 c). Finally, a microwave antenna that provides a magnetic field with the proper polarization to drive the microwave transitions between hyperfine states (described in Sec. 4.2.7) is integrated on the chip. This allows the ion to experience higher microwave fields and gradients, since it is much closer to the ions than the previous triangle trap microwave line, which was ~ 3 mm above from the ions on a Faraday cage that surrounds the trap.

8.3 Possible experiments

A natural starting point for experiments in the triangle trap would be to perform extensions of the work described here for multiple ions. With the use of non-classical states of motion extended to multiple ion sites, we could introduce new degrees of freedom and complexity, like phonon tunneling and effective beamsplitter operations. We could think about doing Sagnac interferometry with the phonons traveling around the triangle as an

alternative to the proposed matter-wave trapped-ion Sagnac interferometer [Campbell and Hamilton, 2017].

We could also begin to explore certain bosonic many-body models and lattice gauge theories, with the phonons acting as the bosonic quasiparticles of interest. The dynamics of the phonons and interactions between neighboring sites could be controlled either by tuning the relative oscillation frequencies of the sites, or using photon-assisted tunneling (PAT), where the energy gap between neighboring sites is provided by a photon from a strong microwave or RF drive [Bermudez et al., 2012]. PAT also introduces a new degree of freedom: the phase of the driving field is imprinted on the tunneled phonon wavefunction, which allows for interesting and controllable phase differences of the phonons as they traverse the triangle with different path orientations, which mimic the phases encountered when encircling field lines that are crucial for simulating lattice gauge theories.

Chapter 9

Conclusion

By exploring the boundaries of quantum mechanics, we can refine our notions of this strange, often counter-intuitive theory, devise new tests of its validity, and facilitate advancements in quantum metrology and quantum information processing. The harmonic oscillator, an elementary and ubiquitous physical system with a simple correspondence between classical and quantum descriptions, is an ideal platform for such experiments. In this thesis, I have presented a series of experiments that extend quantum control of a harmonic oscillator over prior art. I used this control to determine the oscillation frequency with sensitivity better than the standard quantum limit, approaching the Heisenberg limit. I also presented experiments based on coherent displacements of quantum states, using these displacements to devise a spectrum analyzer for sensitive detection of mode-frequency noise over a wide range of frequencies. I discussed potential extensions to all of these experiments, including applying these techniques to multiple ions, for example in the new triangle trap. These methods highlight a growing level of quantum control in trapped-ion systems, which could benefit quantum metrology and quantum information processing and open new opportunities for quantum simulations with ions and phonons as well as mesoscopic mechanical oscillators.

Bibliography

[Aasi, 2013] Aasi, et al., J. (2013). Enhanced sensitivity of the LIGO gravitational wave detector by using squeezed states of light. Nature Photonics, 7:613–619.

[Álvarez and Suter, 2011] Álvarez, G. A. and Suter, D. (2011). Measuring the spectrum of colored noise by dynamical decoupling. Phys. Rev. Lett., 107(23):230501.

[Ballance et al., 2016] Ballance, C. J., Harty, T. P., Linke, N. M., Sepiol, M. A., and Lucas, D. M. (2016). High-fidelity quantum logic gates using trapped-ion hyperfine qubits. Phys. Rev. Lett., 117(6):060504.

[Bermudez et al., 2012] Bermudez, A., Schaetz, T., and Porras, D. (2012). Photon-assisted-tunneling toolbox for quantum simulations in ion traps. New Journal of Physics, 14:053049.

[Bollinger et al., 1996] Bollinger, J. J., Itano, W. M., Wineland, D. J., and Heinzen, D. J. (1996). Optimal frequency measurements with maximally correlated states. Physical Review A, 54(6):4649–4652.

[Born and Wolf, 1980] Born, M. and Wolf, E. (1980). Principles of Optics. Pergamon Press, Headington Hill Hall, Oxford, OX3 0BW, UK.

[Braun et al., 2018] Braun, D., Adesso, G., Benatti, F., Floreanini, R., Marzolino, U., Mitchell, M. W., and Pirandola, S. (2018). Quantum-enhanced measurements without entanglement. Rev. Mod. Phys., 90(3):035006.

[Brown et al., 2011] Brown, K. R., Ospelkaus, C., Colombe, Y., Wilson, A. C., Leibfried, D., and Wineland, D. J. (2011). Coupled quantized mechanical oscillators. Nature, 471(7337):196–199.

[Brownnutt et al., 2015] Brownnutt, M., Kumph, M., Rabl, P., and Blatt, R. (2015). Ion-trap measurements of electric-field noise near surfaces. Rev. Mod. Phys., 87(4):1419–1482.

[Campbell and Hamilton, 2017] Campbell, W. C. and Hamilton, P. (2017). Rotation sensing with trapped ions. Journal of Physics B: Atomic, Molecular and Optical Physics, 50(6):1–13.

[Carruthers and Nieto, 1965] Carruthers, P. and Nieto, M. M. (1965). Coherent States and the Forced Quantum Oscillator. Am. J. Phys., 33(7):537–544.

[Caves et al., 1980] Caves, C. M., Thorne, K. S., Drever, R. W. P., Sandberg, V. D., and Zimmermann, M. (1980). On the measurement of a weak classical force coupled to a quantum-mechanical oscillator. I. Issues of principle. Rev. Mod. Phys., 52(2):341–392.

[Chiaverini et al., 2005] Chiaverini, J., Blakestad, R. B., Britton, J., Jost, J. D., Langer, C., Leibfried, D., Ozeri, R., and Wineland, D. J. (2005). Surface-electrode architecture for ion-trap quantum information processing. Quant. Inf. Comp., 5(6):419–439.

[Chu et al., 2018] Chu, Y., Kharel, P., Yoon, T., Frunzio, L., Rakich, P. T., and Schoelkopf, R. J. (2018). Creation and control of multi-phonon Fock states in a bulk acoustic-wave resonator. Nature, 563(7733):666–670.

[Cirac and Zoller, 1995] Cirac, J. I. and Zoller, P. (1995). Quantum computations with cold trapped ions. Physical Review Letters, 74(20):4091–4094.

[Colombe et al., 2014] Colombe, Y., Slichter, D. H., Wilson, A. C., Leibfried, D., and Wineland, D. J. (2014). Single-mode optical fiber for high-power, low-loss UV transmission. Opt. Express, 22(16):19783–19793.

[Dehmelt and Major, 1962] Dehmelt, H. G. and Major, F. G. (1962). Orientation of $(He^4)^+$ Ions by Exchange Collisions with Cesium atoms. Phys. Rev. Lett., 8(5):213–214.

[Dehmelt and Walls, 1968] Dehmelt, H. G. and Walls, F. L. (1968). "Bolometric" Technique for the rf Spectroscopy of Stored Ions. Phys. Rev. Lett., 21(3):127–131.

[Diedrich et al., 1989] Diedrich, F., Bergquist, J. C., Itano, W. M., and Wineland, D. J. (1989). Laser cooling to the zero-point energy of motion. Phys. Rev. Lett., 62(4):403–406.

[Drees and Paul, 1964] Drees, J. and Paul, W. (1964). Beschleunigung von Elektronen in einem Plasmabetatron. Z. Phys., 180(4):340–361.

[Eibenberger et al., 2013] Eibenberger, S., Gerlich, S., Arndt, M., Mayor, M., and Tüxen, J. (2013). Matter-wave interference of particles selected from a molecular library with masses exceeding 10,000 amu. Physical Chemistry Chemical Physics, 15(35):14696–14700.

[Einstein, 1936] Einstein, A. (1936). Physics and reality. Journal of the Franklin Institute, 221(3):349–382.

[Einstein et al., 1935] Einstein, A., Podolsky, B., and Rosen, N. (1935). Can quantum-mechanical description of physical reality be considered complete? Physical Review, 47(10):777.

[Engelsen et al., 2016] Engelsen, N. J., Hosten, O., Krishnakumar, R., and Kasevich, M. A. (2016). Engineering spin-squeezed states for quantum-enhanced atom interferometry. page FM3C.1. Optical Society of America.

[Ernst et al., 1987] Ernst, R., Bodenhausen, G., and Wokaun, A. (1987). Principles of Nuclear Magnetic Resonance in One and Two Dimensions. Clarendon Press, Oxford.

[Gaebler et al., 2016] Gaebler, J. P., Tan, T. R., Lin, Y., Wan, Y., Bowler, R., Keith, A. C., Glancy, S., Coakley, K., Knill, E., Leibfried, D., and Wineland, D. J. (2016). High-fidelity universal gate set for $^{9}Be^{+}$ ion qubits. Phys. Rev. Lett., 117(6):060505.

[Glauber, 1963] Glauber, R. J. (1963). Coherent and Incoherent States of the Radiation Field. Phys. Rev., 131(6):2766–2788.

[Glauber, 2006] Glauber, R. J. (2006). Nobel Lecture: One Hundred Years of Light Quanta. Rev. Mod. Phys., 78(4):1267–1278.

[Griffiths, 2005] Griffiths, D. (2005). Introduction to quantum mechanics. Pearson Education, Inc.

[Hahn, 1950] Hahn, E. L. (1950). Spin Echoes. Phys. Rev., 80(4):580–594.

[Hänsch and Schawlow, 1975] Hänsch, T. and Schawlow, A. (1975). Cooling of gases by laser radiation. Optics Communications, 13:68–69.

[Harty et al., 2016] Harty, T., Sepiol, M., Allcock, D., Ballance, C., Tarlton, J., and Lucas, D. (2016). High-fidelity trapped-ion quantum logic using near-field microwaves. Phys. Rev. Lett., 117(14):140501.

[Helstrom, 1976] Helstrom, C. W. (1976). Quantum Detection and Estimation Theory. Academic Press.

[Hempel et al., 2013] Hempel, C., Lanyon, B. P., Jurcevic, P., Gerritsma, R., Blatt, R., and Roos, C. F. (2013). Entanglement-enhanced detection of single-photon scattering events. Nature Photonics, 7:630–633.

[Hofheinz et al., 2008] Hofheinz, M., Weig, E. M., Ansmann, M., Bialczak, R. C., Lucero, E., Neeley, M., O'Connell, A. D., Wang, H., Martinis, J. M., and Cleland, A. N. (2008). Generation of Fock states in a superconducting quantum circuit. Nature, 454(7202):310.

[Home et al., 2011] Home, J. P., Hanneke, D., Jost, J. D., Leibfried, D., and Wineland, D. J. (2011). Normal modes of trapped ions in the presence of anharmonic trap potentials. New Journal of Physics, 13(7):073026.

[Howe et al., 1981] Howe, D. A., W., A. D., and Barnes, J. A. (1981). Properties of signal sources and measurement methods. Proc. Freq. Cont. Symp., pages 669– 716.

[Itano et al., 1993] Itano, W. M., Bergquist, J. C., Bollinger, J. J., Gilligan, J. M., Heinzen, D. J., Moore, F. L., Raizen, M. G., and Wineland, D. J. (1993). Quantum projection noise: Population fluctuations in two-level systems. Phys. Rev. A, 47(5):3554–3570.

[Jaynes and Cummings, 1963] Jaynes, E. and Cummings, F. (1963). Comparison of quantum and semiclassical radiation theories with application to the beam maser. Proc. IEEE., 51(1):89–109.

[Joshi et al., 2019] Joshi, M. K., Hrmo, P., Jarlaud, V., Oehl, F., and Thompson, R. C. (2019). Population dynamics in sideband cooling of trapped ions outside the Lamb-Dicke regime. Physical Review A, 99(1):13423.

[Jost, 2001] Jost, J. D. (2001). Entangled Mechanical Oscillators. PhD thesis, University of Colorado, Boulder.

[Keller et al., 2015] Keller, J., Partner, H. L., Burgermeister, T., and Mehlstäubler, T. E. (2015). Precise determination of micromotion for trapped-ion optical clocks. Journal of Applied Physics, 118(10):104501.

[Kielpinski et al., 2002] Kielpinski, D., Monroe, C., and Wineland, D. J. (2002). Architecture for a large-scale ion-trap quantum computer. Nature, 417:709–711.

[Kotler et al., 2011] Kotler, S., Akerman, N., Glickman, Y., Keselman, A., and Ozeri, R. (2011). Single ion quantum lock-in amplifier. Nature, 473(7345):61–65.

[Langer, 2006] Langer, C. E. (2006). High Fidelity Quantum Information Processing with Trapped Ions. PhD thesis, University of Colorado, Boulder.

[Lee et al., 2011] Lee, K. C., R Sprague, M., J Sussman, B., Nunn, J., Langford, N., Jin, X.-M., Champion, T., Michelberger, P., F Reim, K., England, D., Jaksch, D., and Walmsley, I. (2011). Entangling macroscopic diamonds at room temperature. Science (New York, N.Y.), 334(6060):1253–6.

[Lee et al., 2005] Lee, P. J., Brickman, K.-A., Deslauriers, L., Haljan, P. C., Duan, L.-M., and Monroe, C. (2005). Phase control of trapped ion quantum gates. Journal of Optics B: Quantum and Semiclassical Optics, 7(10):S371.

[Leibfried et al., 2003] Leibfried, D., Blatt, R., Monroe, C., and Wineland, D. J. (2003). Quantum dynamics of single trapped ions. Rev. Mod. Phys., 75(1):281–324.

[Leibfried et al., 1996] Leibfried, D., Meekhof, D. M., King, B. E., Monroe, C., Itano, W. M., and Wineland, D. J. (1996). Experimental determination of the motional quantum state of a trapped atom. Phys. Rev. Lett., 77(21):4281–4285.

[Loudon, 2000] Loudon, R. (2000). The Quantum Theory of Light. Oxford University Press, Great Clarendon Street, Oxford, OX2 6DP, UK.

[Margolus and Levitin, 1998] Margolus, N. and Levitin, L. B. (1998). The maximum speed of dynamical evolution. Physica D: Nonlinear Phenomena, 120(1):188 – 195.

[Marquardt et al., 2007] Marquardt, F., Chen, J. P., Clerk, A. A., and Girvin, S. M. (2007). Quantum theory of cavity-assisted sideband cooling of mechanical motion. Phys. Rev. Lett., 99(9):093902.

[McCormick et al., 2019a] McCormick, K. C., Keller, J., Burd, S. C., Wineland, D. J., Wilson, A. C., and Leibfried, D. (2019a). Quantum-enhanced sensing of a single ion mechanical oscillator. Nature. (accepted in principle). Preprint at https://arxiv.org/abs/1807.11934.

[McCormick et al., 2019b] McCormick, K. C., Keller, J., Wineland, D. J., Wilson, A. C., and Leibfried, D. (2019b). Coherently displaced oscillator quantum states of a single trapped atom. Quantum Sci. Technol., 4.

[McLachlan, 1947] McLachlan, N. W. (1947). Theory and Applications of Mathieu Functions. Oxford University Press, Clarendon, Oxford.

[Meekhof et al., 1996] Meekhof, D. M., Monroe, C., King, B. E., Itano, W. M., and Wineland, D. J. (1996). Generation of nonclassical motional states of a trapped atom. Phys. Rev. Lett., 77(11):2346.

[Mielenz et al., 2016] Mielenz, M., Kalis, H., Wittemer, M., Hakelberg, F., Warring, U., Schmied, R., Blain, M., Maunz, P., Moehring, D. L., Leibfried, D., and Schaetz, T. (2016). Arrays of individually controlled ions suitable for two-dimensional quantum simulations. Nature Communications, 7:1–9.

[Monroe et al., 1995] Monroe, C., Meekhof, D. M., King, B. E., Jefferts, S. R., Itano, W. M., Wineland, D. J., and Gould, P. (1995). Resolved-Sideband Raman Cooling of a Bound Atom to the 3D Zero-Point Energy. Phys. Rev. Lett., 75(22):4011–4014.

[Monroe et al., 1996] Monroe, C., Meekhof, D. M., King, B. E., and Wineland, D. J. (1996). A "Schrödinger cat" superposition state of an atom. Science, 272:1131.

[Myers, 2013] Myers, E. G. (2013). The most precise atomic mass measurements in penning traps. International Journal of Mass Spectrometry, 349-350:107 – 122.

[Neuhauser et al., 1978] Neuhauser, W., Hohenstatt, M., Toschek, P., and Dehmelt, H. (1978). Optical-sideband cooling of visible atom cloud confined in parabolic well. Phys. Rev. Lett., 41(4):233–236.

[Ospelkaus et al., 2011] Ospelkaus, C., Warring, U., Colombe, Y., Brown, K. R., Amini, J. M., Leibfried, D., and Wineland, D. J. (2011). Microwave quantum logic gates for trapped ions. Nature, 476:181.

[Paul and Steinwedel, 1953] Paul, W. and Steinwedel, H. (1953). Ein neues Massenspektrometer ohne Magnetfeld. Zeitschrift für Naturforschung A, 8(7):448–450.

[Polzik and Ye, 2016] Polzik, E. S. and Ye, J. (2016). Entanglement and spin squeezing in a network of distant optical lattice clocks. Phys. Rev. A, 93(2):021404.

[Riehle, 2004] Riehle, F. (2004). Frequency Standards Basics and Applications. WILEY-VCH Verlag GmbH & Co. KGaA, Weinheim.

[Sakurai, 1993] Sakurai, J. J. (1993). Modern quantum mechanics. Addison Wesley; Revised edition.

[Sanner et al., 2017] Sanner, C., Huntemann, N., Lange, R., Tamm, C., and Peik, E. (2017). Autobalanced Ramsey spectroscopy. Phys. Rev. Lett., 120(5):53602.

[Schrödinger, 1935] Schrödinger, E. (1935). Die gegenwärtige Situation in der Quantenmechanik. Naturwissenschaften, 23.

[Seidelin et al., 2006] Seidelin, S., Chiaverini, J., Reichle, R., Bollinger, J. J., Leibfried, D., Britton, J., Wesenberg, J. H., Blakestad, R. B., Epstein, R. J., Hume, D. B., W. M. Itano, J. D. J., Langer, C., R. Ozeri, N. S., and Wineland, D. J. (2006). Microfabricated Surface-Electrode Ion Trap for Scalable Quantum Information Processing. Phys. Rev. Lett., 96(25):253003.

[Shu et al., 2011] Shu, G., Chou, C.-K., Kurz, N., Dietrich, M. R., and Blinov, B. B. (2011). Efficient fluorescence collection and ion imaging with the "tack" ion trap. J. Opt. Soc. Am. B, 28(12):2865–2870.

[Slichter et al., 2017] Slichter, D. H., Verma, V. B., Leibfried, D., Mirin, R. P., Nam, S. W., and Wineland, D. J. (2017). UV-sensitive superconducting nanowire single photon detectors for integration in an ion trap. Optics Express, 25(8):8705–8720.

[Srinivas et al., 2019] Srinivas, R., Burd, S. C., Sutherland, R. T., Wilson, A. C., Wineland, D. J., Leibfried, D., Allcock, D. T. C., and Slichter, D. H. (2019). Trapped-ion spin-motion coupling with microwaves and a near-motional oscillating magnetic field gradient. Phys. Rev. Lett., 122:163201.

[Talukdar et al., 2016] Talukdar, I., Gorman, D. J., Daniilidis, N., Schindler, P., Ebadi, S., Kaufmann, H., Zhang, T., and Häffner, H. (2016). Implications of surface noise for the motional coherence of trapped ions. Phys. Rev. A, 93(4):043415.

[Turchette et al., 2000] Turchette, Q. A., Kielpinski, King, B. E., Leibfried, D., Meekhof, D. M., Myatt, C. J., Rowe, M. A., Sackett, C. A., Wood, C. S., Itano, W. M., Monroe, C., and Wineland, D. J. (2000). Heating of trapped ions from the quantum ground state. Phys. Rev. A, 61(6):063418.

[von Förster, 1975] von Förster, T. (1975). A comparison of quantum and semi-classical theories of the interaction between a two-level atom and the radiation field. J. Phys. A: Math. Gen., 8(1):95–103.

[Wigner, 1932] Wigner, E. (1932). On the quantum correction for thermodynamic equilibrium. Phys. Rev., 40(5):749–759.

[Wilhelm et al., 2001] Wilhelm, F. K., van der Wal, C. H., ter Haar, A. C. J., Schouten, R. N., Harmans, C. J. P. M., Mooij, J. E., Orlando, T. P., and Lloyd, S. (2001). Macroscopic quantum superposition of current states in a Josephson-junction loop. Physics-Uspekhi, 44(10S):117–121.

[Wilson et al., 2014] Wilson, A. C., Colombe, Y., Brown, K. R., Knill, E., Leibfried, D., and Wineland, D. J. (2014). Tunable spin–spin interactions and entanglement of ions in separate potential wells. Nature, 512:57–60.

[Wilson et al., 2011] Wilson, A. C., Ospelkaus, C., Van Devender, A. P., Mlynek, J. A., Brown, K. R., Leibfried, D., and Wineland, D. J. (2011). A 750-mW, continuous-wave, solid-state laser source at 313 nm for cooling and manipulating trapped $^9Be^+$ ions. Applied Physics B: Lasers and Optics, 105(4):741–748.

[Wilson-Rae et al., 2007] Wilson-Rae, I., Nooshi, N., Zwerger, W., and Kippenberg, T. J. (2007). Theory of ground state cooling of a mechanical oscillator using dynamical back-action. Phys. Rev. Lett., 99(9):093901.

[Wineland, 2003] Wineland, D. (2003). Lecture notes on quantum information processing in ion traps. Ecole de Physique des Houches.

[Wineland and Dehmelt, 1975] Wineland, D. and Dehmelt, H. (1975). Proposed 10^{-14} $\Delta\nu/\nu$ laser fluorescence spectroscopy on $T1^+$ mono-ion oscillator. Bulletin of the American Physical Society, 20(637).

[Wineland et al., 1998] Wineland, D., Monroe, C., Itano, W., Leibfried, D., King, B., and Meekhof, D. (1998). Experimental issues in coherent quantum-state manipulation of trapped atomic ions. Journal of Research of NIST, 103(3):259–328.

[Wineland et al., 1983] Wineland, D. J., Bollinger, J. J., and Itano, W. M. (1983). Laser fluorescence mass spectroscopy. Phys. Rev. Lett., 50(9):628631.

[Wineland et al., 1992] Wineland, D. J., Bollinger, J. J., Itano, W. M., Moore, F. L., and Heinzen, D. J. (1992). Spin squeezing and reduced quantum noise in spectroscopy. Phys. Rev. A, 46(11):R6797 – R6800.

[Wineland et al., 1978] Wineland, D. J., Drullinger, R. E., and Walls, F. L. (1978). Radiation-pressure cooling of bound resonant absorbers. Phys. Rev. Lett., 40(25):1639–1642.

[Wineland and Itano, 1979] Wineland, D. J. and Itano, W. M. (1979). Laser cooling of atoms. Phys. Rev. A, 20(4):1521–1540.

[Wolf et al., 2018] Wolf, F., Shi, C., Heip, J. C., Gessner, M., Pezze, L., Smerzi, A., Schulte, M., Hammerer, K., and Schmidt, P. O. (2018). Motional Fock states for quantum-enhanced amplitude and phase measurements with trapped ions. Preprint at https://arxiv.org/abs/1807.01875.

[Ziesel et al., 2013] Ziesel, F., Ruster, T., Walther, A., Kaufmann, H., Dawkins, S., K Singer, F. S.-K., and Poschinger, U. G. (2013). Experimental creation and analysis of displaced number states. J. Phys. B: At. Mol. Opt. Phys., 46:104008.

[Zurek, 1991] Zurek (1991). Decoherence and the transition from quantum to classical. Physics Today, 44(10).

[Zurek, 2001] Zurek, W. H. (2001). Sub-Planck structure in phase space and its relevance for quantum decoherence. Nature, 412(6848):712–717.

Appendix A

Precision limit of "classical" measurements on "classical" states

There is fairly general agreement in the literature that any "classical" limit to measurement precision on the frequency of a harmonic oscillator will scale as proportional to $\sqrt{\bar{n}}$, where $\bar{n}$ is the average occupation number [Braun et al., 2018]. Despite this, there is no general agreement on the pre-factor to that scaling, which is necessary to fully define a "standard quantum limit." [Braun et al., 2018] The limit we establish here assumes an observer with classical resources (defined below) that are perfectly implemented.

For comparisons of our experiments to a well-defined classical reference experiment, we extend the notions of classical experiments with light fields given by Roy Glauber [Glauber, 2006] to a general harmonic oscillator. For light fields, Glauber restricted classical sources to coherent light. In this spirit, we broaden the possible physical implementations to any system that can be described as a harmonic oscillator, but limit the admissible operations to coherent displacements. Harmonic oscillator quantum observables are expressed with ladder operators $\hat{a}$ and $\hat{a}^\dagger$ and a coherent state is an eigenstate of the annihilation operator with $\hat{a}|\alpha\rangle = \alpha|\alpha\rangle$. The oscillator's average number of quanta is then given by the expectation value $\bar{n}$ of the number operator $\bar{n} = \langle\alpha|\hat{a}^\dagger\hat{a}|\alpha\rangle = |\alpha|^2$. Glauber restricted classical measurements to measuring intensities for light fields (for example the intensities arising on a screen due to the interference of the two light fields from a double slit arrangement). We generalize light field intensity to number expectation values $\bar{n}$ as the permitted classical measurements

in a harmonic oscillator. The attainable signal-to-noise of such measurements will be limited by shot-noise, given by the standard deviation of a Poisson distribution with mean $\bar{n}$, $\Delta P_{\bar{n}} = \sqrt{\bar{n}}$, for an ideal measurement on a coherent state with unit quantum efficiency and no excess noise. To compare to number-state superpositions of the form $|\Psi_n\rangle = |0\rangle + |n\rangle$, we require that the classical interferometer uses no more energy than the competing number-state interferometer, $\bar{n} = \langle\Psi_n|\hat{a}^\dagger\hat{a}|\Psi_n\rangle \leq n$. This definition of equal resources is somewhat arbitrary, for example one could also argue for the same maximal energy. However, the coherent states have no well defined maximal energy and it is always possible to rescale from our definition to another definition of equal resources. The scaling factor would likely be of order unity in most cases and irrespective of its value, the ideal non-classical interferometer will eventually outperform the classical counterpart due to its more favorable scaling in $\bar{n}$.

With the definitions above, we can devise an interferometer experiment that has the salient features of a Ramsey experiment, but is based on classical states and measurements. A Ramsey experiment consists of two excitations with known relative phase, separated by "free precession" for duration T. An example of a classical-like Ramsey experiment could be to send a short rf-pulse from a reference oscillator with known frequency and phase into a near-resonant circuit. The pulse will ring up the circuit which then evolves freely for T. A second pulse is the sent to the circuit and depending on its phase relative to the first pulse and the phase the excitation has picked up in the resonant circuit during T, the two pulses interfere constructively to further build up the field in the circuit or interfere destructively, diminishing the circuit excitation. For a general harmonic oscillator, this can conveniently be described in phase-space in a frame oscillating at the frequency of the reference oscillator. Starting in the ground state, the first excitation creates a coherent state $|\alpha_1\rangle$, where we can choose phase space coordinates that make $\alpha_1 \geq 0$ real without losing generality. During a free-precession time T the state picks up a phase ϕ_T which transforms it to $|\alpha_1\rangle_T = |\alpha_1 \exp(i\phi_T)\rangle$. In analogy to a Ramsey experiment, the second excitation is chosen

to have the same magnitude with phase ϕ relative to the first excitation, $\alpha_2 = \alpha_1 \exp(i\phi)$. This transforms the state (up to a global phase that is of no consequence to this experiment) into $|\alpha\rangle = |\alpha_1[1+\exp(i(\phi_T-\phi))]\rangle$. Following Glauber's definition of classical measurements, we measure the average occupation $\bar{n}$:

$$\bar{n} = 4\alpha_1^2\left[\frac{1}{2} + \frac{1}{2}\cos(\phi - \phi_T)\right] \tag{A.1}$$

For a fair comparison to a number-state superposition $|0\rangle + |n\rangle$, we would like to restrict our resources to $\bar{n} \leq n$ for all possible ϕ and ϕ_T, so we choose the maximum value $4\alpha_1^2 = n$. Under this restriction, we recover a classical version of the Ramsey fringes described by Eq. (6.2), where we measure $\bar{n} = 0$ when $\phi - \phi_T = (2m+1)\pi$ and $\bar{n} = n$ when $\phi - \phi_T = 2m\pi$, with m integer. We want to minimize the noise-to-signal ratio Eq.(6.3) restricted to coherent excitations and a small free-precession phase $|\phi_T| \simeq 0 \ll \pi$. The noise-to-signal ratio to minimize is

$$\delta\phi_c = \left.\frac{\Delta P_{\bar{n}}}{|\partial P_{\bar{n}}/\partial\phi_T|}\right|_{\phi_T=0} = \frac{\sqrt{n(1/2+1/2\cos(\phi))}}{n/2\sin(\phi)} = \sqrt{\frac{1}{n}}\sqrt{\frac{1+1/\cos^2(\phi)}{2}}. \tag{A.2}$$

The minimum occurs when $\phi = \pi$, which describes two equal and opposite displacements that put the harmonic oscillator back to the vacuum state if the free-precession phase $\phi_T = 0$. Noise and signal both vanish for this interferometer in such a way that their ratio stays finite at $\delta\phi_c = 1/\sqrt{n}$.

This is the best one could possibly do in the case of no excess noise in the system. In practice, when some added noise is present, we would choose a value of ϕ that maximizes the signal, as we did for the case of the number state interferometer. In this case, as was also true for the number state interferometer, the point of maximal signal occurs for $\phi = \pi/2$, so the practical noise-to-signal-ratio yields:

$$\delta\phi_p = \left.\frac{\sqrt{n(1/2+1/2\cos(\phi))}}{n/2\sin(\phi)}\right|_{\phi=\pi/2} = \sqrt{\frac{2}{n}}. \tag{A.3}$$

This interferometer has no practical drawbacks, optimally suppresses additional noise and leads to an increase of the noise-to-signal over the optimal value by $\sqrt{2}$. This implies that the advantage of a number-state interferometer may increase by $\sqrt{2}$ over the ideal limit in a realistic setting, where excess noise (such as current noise or dark counts of a detector) is almost inevitable. This also is arguably a more direct comparison to the $|0\rangle + |n\rangle$ interferometer experiment, where we choose the same relative phase between the two pulses of $\phi = \pi/2$ to maximize the signal. Despite the case to be made for using the more practical limit in our comparisons, we strictly use the more stringent ideal classical interferometer in all our sensitivity comparisons of the number-state interferometers in the main text.